Forward-Backward Asymmetry at High Mass in $t\bar{t}$ Production in $p\bar{p}$ Collisions at $\sqrt{s}$ =1.96 TeV

by

Andrew Peter Eppig

A dissertation submitted in partial fulfillment
of the requirements for the degree of
Doctor of Philosophy
(Physics)
in the University of Michigan
2011

Doctoral Committee:

Professor Dante Eric Amidei, Chair
Professor David W. Gerdes
Professor James Wayne Jones
Professor Gordon L. Kane
Professor Bing Zhou

CONTENTS

LIST OF FIGURES

Figure

LIST OF TABLES

Table

CHAPTER 1

Introduction

1.1 Standard Model

Current understanding of particle physics postulates that there are 17 fundamental particles that interact via four fundamental forces – gravity, the strong force, the weak force, and the electromagnetic force. These fundamental particles can be classified by their spins into bosons, which are the force-carrying particles with integer spins, and fermions, which have half-integer spins. Fermions can be further divided into quarks and leptons. The particles and three of the four forces – all but gravity – are described by the Standard Model, a local $SU(3) \times SU(2) \times U(1)$ gauge theory. Electromagnetic and weak interactions as described by Electroweak Theory or Quantum Electrodynamics, $SU(2) \times U(1)$. Strong interactions are described by Quantum Chromodynamics or QCD, $SU(3)$.

Fermions are grouped into three generations as shown in Table 1.1. Each generation consists of a leptonic doublet containing a charged and a neutral lepton and a weak isospin doublet containing two quarks. The first generation, containing the electron, the electron neutrino, the up quark, and the down quark, is the lightest generation and is thus the most frequently found in nature. The second generation contains the muon, the muon neutrino, the strange quark, and the charm quark. The third generation contains the tau, the tau neutrino, the bottom quark, and the top quark.

Generation	I	II	III
Lepton	electron	muon	tau
Neutrino	electron neutrino	muon neutrino	tau neutrino
Quark	up	strange	top
Quark	down	charm	bottom

Table 1.1. Standard Model Fermions.

1.2 Top Quark

Predicted to be the weak isospin doublet partner of the bottom quark – with $Q = \frac{2}{3}$ and $T_3 = \frac{1}{2}$ – the top quark was the last quark of the Standard Model to be discovered. It was first observed by the CDF and DØ experiments at the Fermilab Tevatron in 1995 [1][2]. With a mass of 173.3 ± 1.1 GeV/c^2, it is the most massive quark – over 40 times heavier than the next heaviest quark, the bottom quark [3] – and is the only quark heavier than the Z and $W^{\pm}$ bosons. At $\sqrt{s} = 1.96TeV$, the top quark has a cross section of 7.5 ± 0.48 pb [22]. Due to its large mass, the top quark decays very rapidly – with a width of less than 7.6 GeV corresponding to a lifetime of less than 10^{-24} s – before it has a chance to hadronize or form bound states. The top quark is unique in this property and allowed the first observation of a bare quark.

Top quarks are produced at the Tevatron in $p\bar{p}$ collisions at $\sqrt{s} = 1.96TeV$ through two primary mechanisms: quark-antiquark annihilation, $q\bar{q} \rightarrow t\bar{t}$ (85%), and gluon fusion, $gg \rightarrow t\bar{t}$ (15%). The theoretical cross section for these $t\bar{t}$ production mechanisms is $\sigma_{t\bar{t}} = 7.50 \pm 0.48$ pb. Top quarks are also produced singly at the Tevatron through weak interactions: $q\bar{q} \rightarrow tb$ and $qg \rightarrow qtb$. The cross section for single top production at the Tevatron is $\sigma_{t\bar{t}} = 2.3 \pm 0.5$ pb. Once produced, a top quark decays into a bottom quark and a W boson – the large mass of the top quark and the CKM angles make this decay process exclusive.

At the Tevatron, after top pair production – $p\bar{p} \rightarrow t\bar{t} \rightarrow WbWb$ – there are three dominant decay modes of the resultant W bosons and bottom quarks, as shown in Table 1.2. The final state quarks from the processes listed in Table 1.2 all hadronize

and appear as jets in the CDF detector.

Name	Process	Fraction
Dilepton	$t\bar{t} \to (W^+b)(W^-\bar{b}) \to (\bar{l}\mu_l b)(l\mu_{\bar{l}}\bar{b})$	0.12
Lepton + jets	$t\bar{t} \to (W^+b)(W^-\bar{b}) \to (q\bar{q}b)(l\mu_{\bar{l}}\bar{b}) + c.c.$	0.44
All-hadronic	$t\bar{t} \to (W^+b)(W^-\bar{b}) \to (q\bar{q}b)(q\bar{q}\bar{b})$	0.44

Table 1.2. The primary decay channels for $t\bar{t}$ production at the Tevatron.

Due to the recency of the top quark discovery, only the mass and cross section have been measured with much precision, so top quark properties remain an untapped are for probing both the Standard Model and new physics. With its high mass, the top quark is sensitive to the Higgs boson (or Higgs bosons depending on the model) or new gauge bosons – new bosons could be detected by direct decay from the top quark or appear in loop corrections to which the top quark is sensitive. New physics often revolves around symmetries – either the conservation of a previously unobserved symmetry or the breaking of an established symmetry – and symmetries provide an important tool for discovering new phenomena where the underlying dynamics are unknown.

1.3 CP Symmetry

A symmetry is an invariance of a system under a given transformation. Noether's Theorem states that any continuous symmetry has a corresponding conservation law. For example, the invariance of a system with respect to temporal translation corresponds to the conservation of energy. Symmetries do not have to be continuous; discrete symmetries are also common in physics. Charge symmetry (C) is the invariance of a system under the exchange of particles to their anti-particles and vice-versa which leaves the the charge conserved.[1] This property leads to the convention of

[1]In the context of Noether's Theorem, QED is a gauge theory with U(1) symmetry, the conservation law associated with this symmetry is charge conservation.

calling a particle's anti-particle its charge-conjugate – a convention that extends to a system of particles. Parity symmetry (P) is the invariance of a system under the exchange of all spatial coordinates with their additive inverses (e.g., $\vec{x} \rightarrow -\vec{x}$). Time reversal symmetry (T) is the invariance of a system under the exchange of all temporal coordinates with their additive inverses (e.g., $t \rightarrow -t$). Julian Schwinger showed that a simultaneous conservation of charge, parity, and time reversal (CPT) as a necessary condition for a Lorentz invariant, local quantum field theory with a Hermitian Hamiltonian. This concept was formalized by Wolfgang Pauli and Gerhart Lüders as the CPT Theorem. In addition to being conserved together as CPT, it was thought that each symmetry was always conserved individually. Individual conservation was disproved by C. S. Wu with her discovery of parity violation in the weak decay of radioactive nuclei. Simultaneous charge and parity conservation were disproved by James Cronin and Val Fitch in their observation of weak decay in kaons. For the CPT Theorem to hold true, if CP-symmetry is broken, then T-symmetry is also broken in the weak decay of kaons. Other weak interactions have since been shown to violate these symmetries, but strong interactions are expected to conserve charge-, parity-, and time-symmetries, though limited work has been able to be done to test this supposition, especially at high energy. Top quark pair production at the Tevatron is a natural place to test symmetries of strong interactions at high energies, as it allows for an event-by-event comparison of top and anti-top.

1.4 Forward-Backward Asymmetry

As explained in more detail in Section 2.1, interactions at the Tevatron involve protons traveling in circular direction colliding with anti-protons traveling in the opposite direction. In such a geometry, it is natural to define a coordinate system with one axis in along the beam line (the direction of the protons is chosen to be the positive direction). Top-anti-top pairs are produced with the top and anti-top having equal

and opposite momenta. One can define an angle, θ, determined by the angle between the direction of the top quark and the positive beam axis. The differential cross-section of the top-anti-top production can be expressed as a function of θ.

$$\frac{d\sigma}{d\cos\theta} = \frac{\alpha_s}{q^2} f(\cos\theta) f(\vec{s}) \tag{1.1}$$

In terms of symmetries, it is natural to ask if $f(\cos\theta)$ in Equation 1.1 is symmetric. To explore charge-symmetry in top pairs, it is useful to define a representation of charge asymmetry in terms of top and anti-top quarks as given in Equation 1.2.

$$A_C = \frac{N_t(p) - N_{\bar{t}}(p)}{N_t(p) + N_{\bar{t}}(p)} \tag{1.2}$$

$N_i(j)$ is defined as the number of particle i traveling in the direction of particle j. If the charge asymmetry, A_C, is non-zero it implies a net top current flowing in the direction of the protons. With the design of the Tevatron in mind, it is also useful to define a representation of a forward-backward asymmetry in terms of protons and anti-protons as given in Equation 1.3.

$$A_{FB} = \frac{N_t(p) - N_t(\bar{p})}{N_t(p) + N_t(\bar{p})} \tag{1.3}$$

If the forward-backward asymmetry, A_{FB}, is non-zero it implies a net top current flowing in the direction of the protons or anti-protons depending on the sign of the asymmetry. If C-symmetry is conserved, then $N_{\bar{t}}(p) = N_t(\bar{p})$, implying that the charge and forward-backward asymmetries, Equations 1.2 and 1.3, are equal. Thus a charge-symmetry is equivalent to a forward-backward symmetry.

1.5 QCD Asymmetry

Though strong interactions are expected to conserve charge, QCD predicts that strong interactions in top pair production at the Tevatron will produce net charge asymmetry. At leading order (LO), no charge asymmetry is expected, as quarks and anti-quarks are interchangeable. But at next-to-leading order (NLO), interference in the correction terms leads to differences in quark and anti-quark production, leading to net charge asymmetries. This process is analogous to the charge asymmetry found in $e^+e^- \to \mu^+\mu^-$ production where the radiative photon corrections of the QED process are replaced by radiative gluon corrections in the QCD process. As shown in Ref. [4], the QCD charge asymmetry is proportional to the QED charge asymmetry with appropriate color terms added.

$$f(\cos\theta) = (1 + \cos^2\theta) + (1 - \beta^2)\sin^2\theta \tag{1.4}$$

Two different processes lead to differently signed asymmetries that then combine to form a net asymmetry. The first process is radiative corrections in the form of gluon brehmsstrahlung in both the incoming and outgoing states, Figures 1.1a and 1.1b. These two sub-processes add together to form a negative overall charge asymmetry. The second process is the interference of box diagram processes with the Born process, Figures 1.1c and 1.1d; these two sub-processes add together to form a positive overall charge asymmetry. While one process gives a negative asymmetry and the other gives a positive asymmetry, the two are not of equal magnitude, creating a net positive asymmetry when all terms are added together. The predicted QCD NLO asymmetry is 4-5% [4], and the next-leading-order Monte Carlo generator MC@NLO estimates 5% [5].

The NLO asymmetry is both mass- and rapidity-dependent, as shown in Figure 1.2 which shows the estimated parton-level NLO asymmetry as generated by the Monte

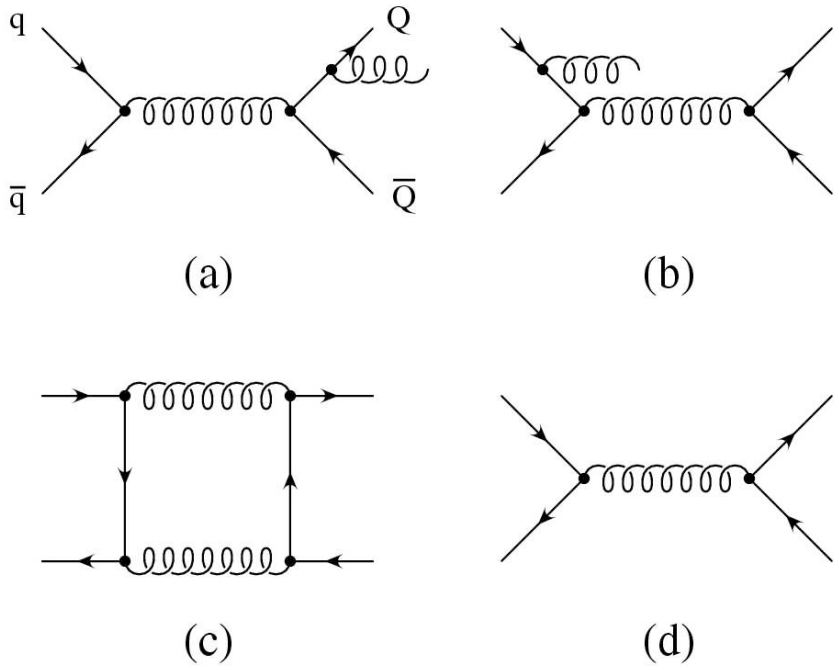

Figure 1.1. NLO and LO diagrams. a) final-state-radiation; b) initial-state-radiation; c) box diagram; and d) Born process

Carlo generator MCFM [6].

1.6 Previous Tevatron Asymmetry Results

With 3.2 fb^{-1} of $p\bar{p}$ collisions, CDF measured a forward-backward asymmetry in the lab frame of $A_{FB} = 0.193 \pm 0.069$ – the mass-dependence of the asymmetry was examined and found consistent with the NLO expectation [7][8][9][10][11]. With 4.3 fb^{-1} of $p\bar{p}$ collisions, DØ measured a forward-backward asymmetry in the lab frame of $A_{FB} = 0.08 \pm 0.04$ [12]. While these results have remained consistent with expected QCD asymmetries, other mechanisms beyond the Standard Model have been proposed to produce the measured asymmetries. These mechanisms include axigluons, diquarks, new weak bosons, and extra-dimensions which produce forward-backward asymmetries in $t\bar{t}$ production while remaining consistent with the observed $t\bar{t}$ cross-section and invariant mass distribution [13].

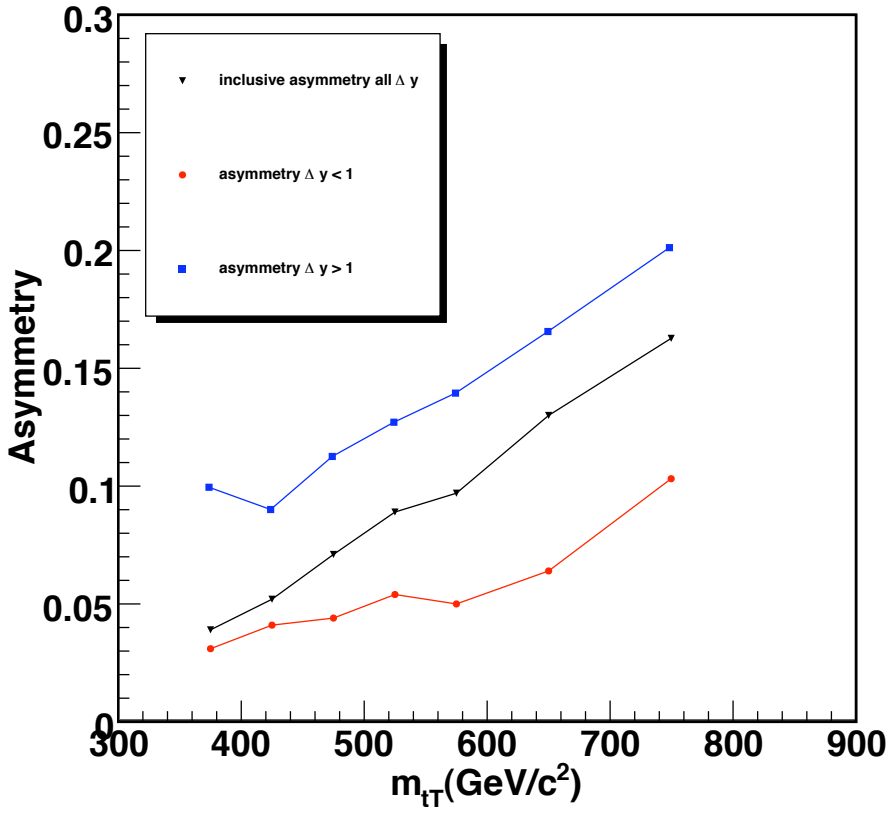

Figure 1.2. Forward-backward asymmetry in top pair production versus top pair mass as estimated by Monte Carlo generator MCFM. The asymmetry versus mass is also shown for two different rapidity regions.

1.7 Analysis Plan

Following the introduction and motivation of the previous sections, the analysis will proceed as follows:

- Chapter 2 gives an overview of the collider and detector used to generate and collect the data sample used in the analysis.
- Chapter 3 summarizes the selection cuts applied to the collected data sample.
- Chapter 4 discusses the simulated event samples that model the signal and backgrounds for the data sample.
- Chapter 5 describes the reconstruction algorithms applied to the selected data to produce the data sample along with the validation of the reconstruction.
- Chapter 6 analyzes the inclusive forward-backward asymmetry of the data sample.
- Chapter 7 expands upon the inclusive analysis of Chapter 6 to analyze the mass-dependent forward-backward asymmetry of the sample.
- Chapter 8 details checks of non-signal sources of the measured asymmetry.
- Chapter 9 validates the correction technique applied to the data sample in Chapter 7.
- Chapter 10 reviews the sources of systematic uncertainties in the analysis and calculates a systematic error for each source
- Chapter 11 wraps up the analysis with a summary of the findings.

.

CHAPTER 2

Experimental Apparatus

This analysis uses data collected by the Collider Detector at Fermilab (CDF) experiment at Fermilab's Tevatron accelerator. Located in Batavia, Illinois outside of Chicago, Fermilab was founded in 1967 and is currently the largest laboratory for particle physics in the United States. The Tevatron collides protons and antiprotons at a center of mass energy of $\sqrt{s} = 1.96$ TeV.

2.1 The Tevatron

Built in 1983, the Tevatron accelerator was the first superconducting synchrotron in the world. It is located at the end of a chain of seven Fermilab accelerators which are used together to accelerate protons and antiprotons to a center of mass energy of 1.96 TeV [14]. The accelerator complex is shown schematically in Figure 2.1.

The acceleration process begins inside a Cockcroft-Walton accelerator, where H^- ions are created by ionizing hydrogen gas. A static electric field between the grounded wall and an electrically charged dome accelerates the ions to an energy of 750 keV, at which point they are grouped into bunches and enter a 500 foot long linear accelerator or Linac. A combination of drift tube Linacs and Klystron amplifiers use 201 MHz radio frequency (RF) pulses to accelerate the ion beam from 750 KeV to 400 MeV.

The beam then enters a circular synchrotron accelerator called the Booster where the electrons are stripped off leaving only a proton beam. A synchrotron with a 75m diameter, the Booster converts the proton beam into discrete proton bunches

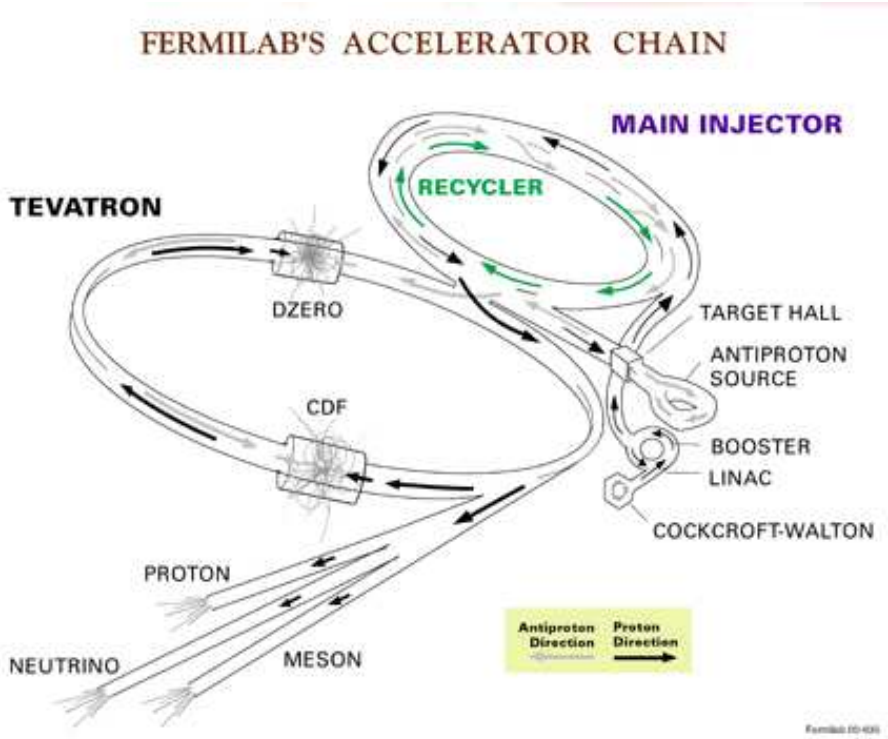

Figure 2.1. The Fermilab Accelerator Complex

and then accelerates them using RF cavities. The proton beam is directed along its circular path using dipole magnets. The beam circles the Booster approximately 20,000 times before reaching an energy of 8 GeV, at which point it is ready to be passed on to the next accelerator in the chain, the Main Injector. Only a portion of the protons that reach this stage are actually passed on to the Main Injector, while the rest are used for other experimental programs at Fermilab.

The Main Injector, a synchrotron with a radius seven times that of the Booster, serves several purposes. At this point in the accelerator chain, it accelerates the proton beam from 8GeV to 120GeV. Some of these 120 GeV protons are used for Fermilab's other experiments, while the rest are sent to the antiproton source to create antiprotons. These protons strike the antiproton target, a nickel disk, every 1.5 seconds and create a shower of new particles. The particles created are focused using a lithium lens, and then the negatively charged antiprotons, which have an average energy of 8 GeV, are separated from the other particles by passing the shower

of particles through a magnetic field.[1] For every 100,000 protons which strike the target, only 1 antiproton is created, so a very large number of protons is needed to accumulate a usable antiproton beam.

Once the antiprotons have been filtered from the other particles, they enter an accelerator called the Debuncher that cools the antiprotons to a uniform energy. At this point, the antiprotons are accelerated to a uniform energy of 8 GeV. Because the antiprotons enter the Debuncher with a spread of energies, the result of this process is that, although the energy of the beam becomes uniform, the antiprotons are now spread out in space and no longer in bunches. The beam is then passed to the Accumulator, which is located in the same tunnel as the Debuncher. By making the transfers from the Debuncher to the Accumulator at discrete moments in time, a process called "stacking", the bunch structure is returned to the antiproton beam. The antiprotons are collected in the Accumulator over several hours, at which point they are transferred to the Recycler, a fixed energy storage ring located in the same tunnel as the Main Injector. It can take 12-24 hours for a sufficient number of antiprotons to become available for loading into the Tevatron.

When enough antiprotons have been created, the Main Injector is used to accelerate proton and antiproton bunches from 8 GeV to 150 GeV and then inject these bunches into the Tevatron. With a radius of 1 kilometer and a 53.1 MHz RF used for acceleration, there are 1,113 RF wavelengths along the circumference of the Tevatron. The spacing between the proton and antiproton bunches is determined by the radio waves, resulting in 1,113 slots, called "buckets", in which the proton and antiproton bunches are able to travel. At the beginning of a run, 36 bunches of protons with an energy of 150 GeV are injected into the Tevatron from the Main Injector, and 36 antiproton bunches are injected in the opposite direction. The proton bunches generally

[1]The separation procedure takes advantage of the electrodynamic force relationship, $\vec{F} = q\vec{E} \times \vec{B}$. Charged particles in a fixed electromagnetic field will curve differently depending on their charge and energy, allowing one to separate out particles with selected properties.

contain several times the number of particles that are in the antiproton bunches, since protons are much easier to obtain. The 36 bunches are injected in three groups of 12, called "trains". Within a train, there are 20 empty buckets between each bunch, and there are larger spaces between each train. If the beam becomes unstable for any reason, the large gap between trains allows time for abort switch magnets to turn on and abort the beam, directing it into a concrete block before it can do any damage to the accelerator or the detectors.

After all proton and antiproton bunches have been loaded into the Tevatron, the beams are accelerated once more from 150 GeV to 980 GeV. Large steel blocks called "collimators" are inserted close to the beam to remove any stray particles, and the transverse beam size is reduced to approximately 2 microns using quadrupole magnets on each side of both the CDF and DØ detectors. At 980 GeV, each bunch circles the 6 km circumference ring approximately 50,000 times each second. Collisions are initiated at the CDF and DØ experiments by electrostatic separators that rotate the helical proton and antiproton beams, creating direct collisions at only two points along the ring. The detectors are built around these two collision points.

Even though trillions of particles are contained in the proton and antiproton beams, only a few collisions - generally fewer than 10 - occur each time proton and antiproton bunches cross. The probability of a collision taking place at a given time can be quantified by the instantaneous luminosity, which is given by Equation 2.1 [24].

$$L = n\ f \frac{N_p\ N_{\bar{p}}}{\sigma_x\ \sigma_y}\ cm^{-2}s^{-1} \tag{2.1}$$

In this equation, n is the number of bunches, f is the revolution frequency, N_p and $N_{\bar{p}}$ are the number of protons and antiprotons in each bunch, and σ_x and σ_y are the average width of a bunch in the transverse directions. The luminosity measures the number of protons that interact with antiprotons per cm^2 per second. For a process

that has a given cross-section σ, the luminosity can be used as in Equation 2.2 to determine the number of times that process will occur. Once collisions have begun, the Tevatron can run 30 hours or even longer before it needs to be reloaded, although generally it is refilled approximately every 20 hours in order to keep the instantaneous luminosity as large as possible and maximize the number of collisions observed.

$$N = \int L \, \sigma dt \tag{2.2}$$

Because the cross sections for various processes will be constant at a given energy, we can define the integrated luminosity, a measure of the total amount of data collected, as $\mathcal{L} = \int L \, dt$. Then the total number of events that will take place for a given process can be written as $N = \mathcal{L} \, \sigma$. Since cross sections are often measured in units of femtobarns (fb) and the number of events is a unitless number, the integrated luminosity is measured in units of fb^{-1}. The dataset used in the analysis described here has an integrated luminosity of 4.3 fb^{-1}, which means that for a process that has a cross section of 1 fb, we would expect to produce 4.3 events.

2.2 The CDF Detector

When a collision takes place at the Tevatron, it can be observed and recorded by the CDF detector, a general purpose, longitudinally and cylindrically symmetric particle detector located within and around a solenoidal magnetic field [15]. CDF can measure the charge, momentum, and energy of various types of particles using several different detector systems, each of which is optimized for a particular type of particle or measurement. Figure 2.2 shows the various detector systems, each of which is discussed below [15].

Different types of particles interact differently with the CDF detector. CDF has several basic layers of detector systems: tracking chambers, an electromagnetic calorimeter, a hadronic calorimeter, and muon chambers. The detector needs to

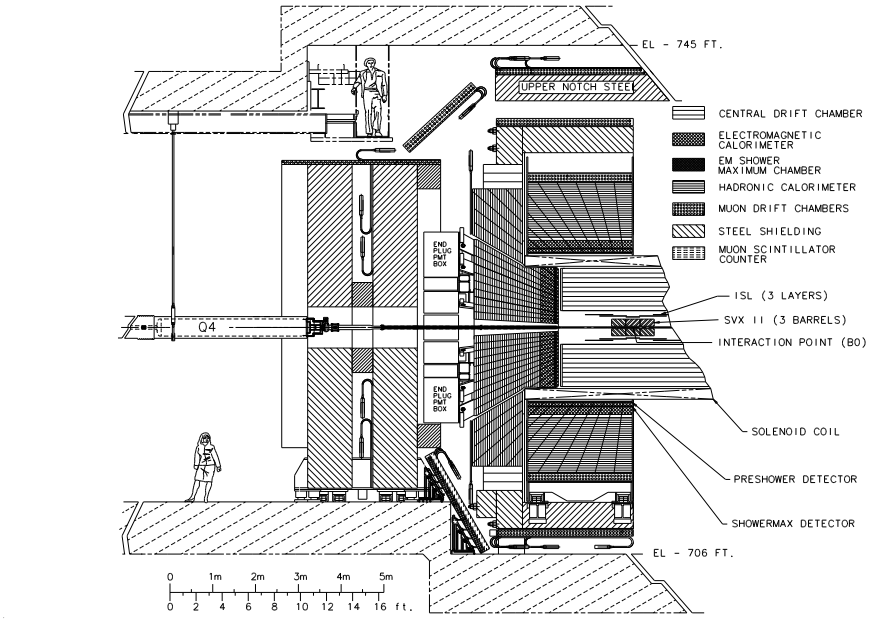

Figure 2.2. Diagram of the CDF Detector

identify many different types of objects: photons, electrons, muons, jets created by the hadronization of quarks, and neutrinos. The way that these particles interact with the detector is summarized in Figure 2.3 [16]. In the CDF detector, the tracking chambers are located inside the solenoidal magnetic field, while the remaining components are outside of the magnet.

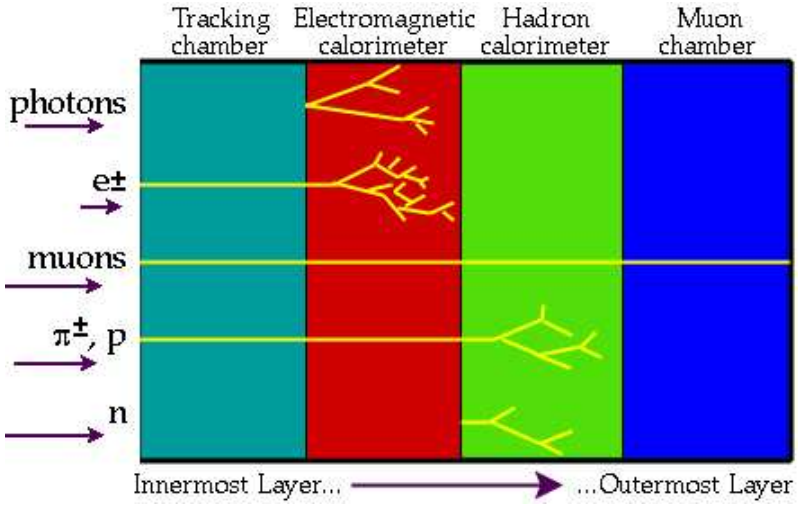

Figure 2.3. How Different Particles Interact with the Detector

Because photons are neutral, they will not leave a track in the tracking chambers,

but will deposit energy in the electromagnetic calorimeter. Electrons, being charged, will leave tracks in the tracking chambers as well as energy in the electromagnetic calorimeter. Muons are charged, and thus leave tracks in the tracking chambers, but they do not interact with most material, so they will not deposit much energy in either calorimeter system, and will travel all the way through the detector to leave hits in the muon chambers. Charged hadrons from quark jets will leave tracks in the tracking chambers and leave some energy in the electromagnetic calorimeter, but most of their energy will be deposited in the hadronic calorimeter. Neutral hadrons in quark jets will not leave tracks, and will deposit little energy in the electromagnetic calorimeter, but will deposit most of their energy in the hadronic calorimeter. Finally, neutrinos do not interact with any part of the detector, and are detectable only by their absence - because they carry energy away but do not interact with the detector, they are detected as an imbalance of momentum left in the detector.

2.2.1 Coordinates and Definitions

The CDF detector can be described by a right-handed spherical coordinate system with the origin at the center of CDF and the z-axis pointing along the direction of the proton beam. The x-axis, from which the azimuthal angle ϕ is measured, points out radially from the center of the Tevatron in the plane of the Tevatron ring. The polar angle θ is measured from the z-axis, although it is often transformed to a new variable called pseudorapidity, η, defined in Equation 2.3.

$$\eta = -\ln(\tan(\frac{\theta}{2})) \tag{2.3}$$

The new variable η is convenient at a hadron collider because Lorentz boosts along the z-direction appear as linear translations, $\eta \rightarrow \eta' = \eta + f(\beta)$. This is useful because the momentum along the z-direction of the two initial colliding partons will be different in each event, depending on what fraction of the proton (or antiproton)

momentum each parton carries. For the same reason, it is also useful to define the transverse energy $E_T = E \sin\theta$ and the transverse momentum $P_T = P \sin\theta$. P_T and η form a complete set of coordinates.

2.2.2 The Silicon Tracking Detectors

The innermost detector system at CDF consists of the silicon tracking detectors. This detector system is critical to many analyses at CDF because it is able to measure track impact parameters with a resolution of approximately 30 microns. As will be discussed in Chapter 3, this allows for the tagging of jets originating from bottom quarks, providing a very useful way to differentiate signal events from background events in this analysis and many others.

The silicon detectors are made up of many silicon semiconductor p-n junctions. When a charged particle passes through the detector, it will cause ionization in the depletion regions of the semiconductors, allowing the particle to be detected and tracked. There are three separate detectors that make up the silicon tracking system: Layer 00 (L00), the Silicon Vertex Detector (SVX), and the Intermediate Silicon Layer (ISL). Together, these three systems cover a cylindrical area around the beam pipe with a radial range from 1.5 cm to 32 cm, and they can detect tracks from charged particles with $|\eta| \leq 2$.

L00 consists of a single-sided silicon microstrip detector and is attached directly to the beam pipe. It is surrounded by the SVX, which is made up of five layers of silicon microstrip ladders which are double-sided (each strip contains p-n junctions on both sides). Outside of the SVX is the ISL, which again consists of double-sided silicon ladders. There is one ISL layer that covers the central region of the detector and two additional ISL layers that provide tracking out to $|\eta| = 2$.

2.2.3 The Central Outer Tracker

The entire silicon tracking system is located inside CDF's other tracking detector, the central outer tracker (COT). The COT is an open cell drift chamber made up of eight concentric superlayers of tracking cells which use an argon-ethane mixture for the ionizing gas. Each cell spans the entire length of the COT and contains alternating potential wires, held at a voltage of 2 kV, and sense wires, held at a voltage of 3 kV.

When a charged particle enters the COT, it causes the argon-ethane mixture to become ionized. The electrons released during this ionization drift towards the sense wires, causing secondary ionization and releasing additional electrons. This charge is deposited on a sense wire, and the charge and its arrival time are recorded by a charge integrating amplifier/ADC and a fast time-to-digital converter. By knowing the electron drift velocity in the gas mixture, the distance to the original ionization can be determined, and a track can be reconstructed. In this way, the COT is able to measure tracks for charged particles with $|\eta| \leq 1$.

Both the silicon detectors and the COT are enclosed inside a large superconducting solenoid magnet which creates a field of 1.4 T. This field causes the paths of charged particles to curve in the azimuthal plane. The amount of curvature depends on the transverse momentum of a particle, so the curvature can be used to measure this momentum. The silicon and COT combined can measure P_T with a resolution of approximately $\frac{\delta P_T}{P_T} = 0.0012\ P_T$ [15].

2.2.4 The Electromagnetic and Hadronic Calorimeters

The electromagnetic (EM) calorimeters are located directly outside of the magnet and are used to measure energy deposition by particles that interact mainly via the electromagnetic interaction (photons and electrons). The central electromagnetic calorimeter (CEM) covers the range $|\eta| \leq 1.1$, while the plug electromagnetic calorimeter (PEM), covers $1.3 \leq |\eta| \leq 3.6$. Both electromagnetic calorimeter sys-

tems are made up of alternating layers of lead and plastic scintillator. When an electron enters the calorimeter, it will radiate photons due to deceleration caused by the electromagnetic fields of atomic nuclei (bremsstrahlung radiation). Each radiated photon can then convert into an electron-positron pair, which in turn causes more bremsstrahlung, and the shower continues to grow until the resulting particles do not have enough energy to emit any radiation.

The total energy in the shower (equivalent to the energy of the initial particle entering the calorimeter) is proportional to the amount of light produced by the shower in the scintillator layers.[2] The light is collected by the scintillators and transmitted to a photomultiplier tube, where the total amount of light produced is measured. In this way, the electromagnetic calorimeters are able to determine the energy of an incident photon or electron with a resolution of approximately $\frac{\delta E_T}{E_T} = 0.14/\sqrt{E_T}$ [15].

Several layers into the CEM, at the depth where the electromagnetic shower is expected to be at a maximum, there is a layer of wire chambers called the central electron strip (CES) detector. Similarly, there is a PES detector located inside the PEM. These detectors are used to localize the position of an electromagnetic shower inside the calorimeter, allowing better matching of showers to tracks observed by the COT.

Charged hadrons that pass through the electromagnetic calorimeter lose a small portion of their energy, but they do not cause a shower because they do not radiate photons. In order to measure the energy of hadrons, the hadronic calorimeters (HAD) are located just outside of the electromagnetic calorimeters. The HAD calorimeters cover the same range as the EM calorimeters, and are analagous in design - the HAD calorimeters are made up of alternating layers of iron and scintillator. Hadrons

[2]Each particle in the shower stimulates the scintillating material to produce photons. The photons are channeled through the scintillating layer to the photomultiplier tubes, recording the number of photons produced by the passing of the particle, which is proportional to the energy of the particle at the time it pass through the scintillating layer.

entering the HAD calorimeters participate in nuclear interactions within the iron, creating a shower of new particles which can then undergo nuclear interactions themselves. The showering hadrons then enter the scintillator layers and produce light, which is used to measure the energy in the shower. Because the shower in the HAD calorimeters depends on nuclear interactions, which occur less frequently than the bremsstrahlung radiation in the EM calorimeter, there are generally fewer particles in a shower in the HAD calorimeters, and the energy resolution is poorer - approximately $\frac{\delta E_T}{E_T} = 0.50/\sqrt{E_T}$ in the central HAD calorimeter [15].

2.2.5 The Muon Chambers

The final layer of the CDF detector, located beyond the HAD calorimeters, consists of the muon chambers. Muons interact via the electromagnetic force, but because they are 200 times more massive than the electron, they do not readily produce bremsstrahlung radiation. They therefore pass through the calorimeters without losing energy or creating a shower. Large steel slabs surround the hadronic calorimeters, designed to stop all particles except muons from passing through. Wire chamber drift cells are placed just outside of these slabs to detect muons that travel beyond the steel slabs. Similar to the COT, when a muon passes through a chamber, it ionizes the gas (which is argon-ethane, as is used in the COT). The ionization electrons then drift to high voltage wires in each chamber, and the detector records the passage of a muon.

The CDF detector contains several sets of muon chambers, each of which consists of four layers of drift cells with a slight azimuthal offset. Hits in these muon chambers define a track segment or "stub" which can then be matched to a reconstructed track in the COT. The central muon detector (CMU) and the central muon upgrade (CMP) cover the range $|\eta| \leq 0.6$. The central muon extension (CMX), located at the corners of the detector, covers the range $0.6 \leq |\eta| \leq 1.0$. Finally, the barrel muon upgrade

(BMU) covers the region with $1.0 \leq |\eta| \leq 1.5$.

2.3 Data Acquisition at CDF

Collisions occur at the Tevatron every 396 nanoseconds. With 750,000 channels in the detector to be read out, it is impossible to record every collision on this timescale, so a "trigger" system must be used to decide which events to record. CDF uses a three stage trigger system that was designed to look at the 2 million collisions that occur each second and select only the approximately 75 most interesting ones to be recorded. This trigger system is shown schematically in Figure 2.4. It was designed so that the data acquisition (DAQ) system could check at least 95% of the collisions to determine whether or not to keep the event.

The first trigger stage, the Level 1 selection, stores information for 42 consecutive bunch crossings in a hardware buffer. Each event is kept for 5500 ns, allowing the buffers to collect signals from all detector systems but the silicon detectors – including the COT and muon chambers, which have long drift times. The Level 1 hardware fits helical tracks to hits in the COT, matches extrapolated COT tracks to hits in the muon chambers, and finds the energy deposited in the calorimeter. The results of these operations are compared with the Level 1 selection criteria, as listed in a "trigger table", and a decision is made as to whether to pass the event on to the next level or reject it. The Level 1 system is designed to process the low level information from each event in less than 4000 ns so that no event is lost from the buffer before a decision is made.

An event that passes the Level 1 selection is passed on to one of four Level 2 buffers. At this point, the silicon tracking system is read out and tracks are reconstructed to determine if there are any jets which could potentially be tagged as bottom quark jets. Information from the electromagnetic and hadronic calorimeters is used to identify possible electrons, photons, and jets. Processors then combine the information from

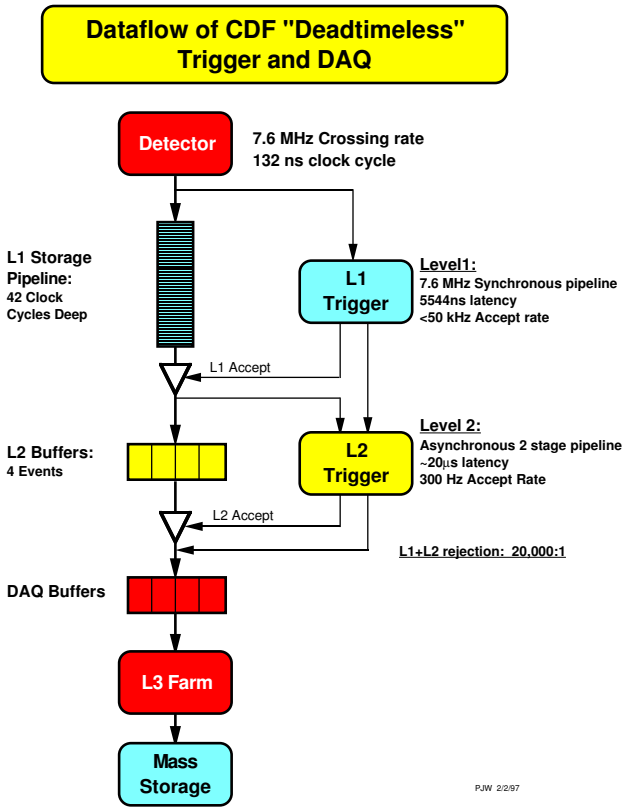

Figure 2.4. Schematic of the Data Acquisition System

various sources and make a more sophisticated decision than the Level 1 system by comparing each event to a set of criteria determined by the trigger table.

After an event is selected by the Level 2 system, the entire detector is read out and this information is sent to one of several hundred processors that make up the Level 3 system. This is the first time that the event is fully reconstructed using all the detector channels. The Level 3 processors can take up to a second to reconstruct an event and then make a final decision on whether or not to record that event, based on the types of particles present in the event and certain other properties of the event as a whole.

Once an event has been accepted by the Level 3 trigger system, it is written to a magnetic tape at Fermilab's computing center. From there, offline processing is performed to apply calibrations for variables that can change over time, such as beam alignment, and a detailed validation of the data is performed. The data can then be used for analysis.

CHAPTER 3

Event Selection

Collisions at the Tevatron can result in many different interactions, producing many possible final states, but this analysis is concerned with only those events that have a final state that could have been the result of the decay of a pair of top quarks. The event selection must be designed to separate these signal events from the background – the many other processes that occur at the Tevatron. In particular, we consider events where the final state has a signature consistent with a $t\bar{t}$ system decaying via the lepton plus jets decay channel, where one of the top quarks in the $t\bar{t}$ system decays leptonically via $t \rightarrow Wb \rightarrow \ell\nu b$ and the other top quark decays hadronically via $t \rightarrow Wb \rightarrow udb$. One reason for using this channel is that the detector is very good at identifying electrons and muons, which are rarely produced at hadron colliders, greatly in reducing the number of background events.

We use the standard selection that has been developed at CDF for $t\bar{t}$ events in the lepton plus jets decay channel. This selection requires one central ($|\eta| < 1$), high energy ($P_T > 20\ GeV$) charged lepton (from the leptonically decaying W boson), four high energy ($E_T > 20\ GeV$) jets (clusters of particles resulting from the hadronization of the two bottom quarks and the two quarks from the hadronically decaying W boson), and a large ($\not\!\!E_T \geq 20\ GeV$) amount of missing energy (from the neutrino, which passes through the detector without depositing any energy). Due to the difficulty of correctly identifying tau leptons in the detector, the charged lepton is required to be an electron or a muon. Electrons are identified by looking for isolated

tracks pointing to isolated energy deposits in a single electromagnetic calorimeter tower in the CEM; muons are identified as tracks in the COT that align with track stubs in the muon chambers. The two jets associated with the bottom quarks are used to track the bottom quark prior to hadronization. While W bosons decay near-instantaneously, bottom quarks have a longer lifetime and thus decay away from the interaction point (the distance is $\gamma\beta c\tau = 500\ \mu m$), so the bottom quarks in an event must have a secondary vertex displaced from the primary interaction vertex.

There are several steps in the event selection, the first of which is performed by the online trigger system as events are selected to be read out and written to tape. This online selection is primarily driven by the detection of a high momentum electron in the CEM calorimeter or a high momentum muon in the CMUP or CMX muon chambers. This method allows us to take advantage of the rarity of leptons at a hadron collider and immediately reduce the background. Once an event has been selected by the online trigger system, it is written to disk and the data is then processed offline. At this point, a number of calibration corrections are made, allowing tracks and energy showers to be reconstructed using the information taken directly from the detector. This reconstruction allows us to identify objects like electrons, muons, or jets. By looking at these objects, we can make a final determination as to whether an event should be selected as a $t\bar{t}$ candidate. The details of this selection are described in [17]. In the dataset used for this analysis, which has an integrated luminosity of 5.3 fb^{-1}, we select 1,260 candidate $t\bar{t}$ events.

CHAPTER 4

Modeling the Expected Signal and Background

It is necessary to have a model for the signal and the background for a given event sample to check that the events are properly reconstructed. The models are created using simulated data sets, which are mathematical models based on theoretical and experimental understanding of the underlying physical interactions. The millions of events generated in simulated data sets allow for measurements of expected phenomena and detector responses with high statistical precision.

4.1 Event Generation and Simulation

Most of our signal and background samples are modeled by simulating events produced by each particular signal and background process. This simulation takes place over several steps. First, the initial conditions of the $p\bar{p}$ collision must be modeled, and the momenta of the colliding particles are fed into an event generator. This event generator performs the matrix element calculation for the various processes and produces output "events" which fully specify the momenta of the various outgoing particles. The hadronization of any outgoing partons into jets must then be simulated in a process called parton showering. Finally, the results of this simulation are passed through a simulation of the detector response, called CDFSim. The output of this final step is a set of data banks identical to those which would be read out from the detector, as if a given simulated event actually occurred inside the detector. The various event generators used for modeling both our signal and background

processes are listed below.

- PYTHIA [18]: PYTHIA is a multi-purpose, leading order event generator which also includes parton showering. It is used for $t\bar{t}$ modeling and also for some of our background samples. PYTHIA models quarks, gluons, PDFs, final state decays, and parton showers of the underlying events.
- HERWIG [19]: HERWIG is a leading order matrix element event generator which also includes parton showering. It is particularly suited for modeling the emission of low-energy gluons. Because HERWIG includes $t\bar{t}$ spin correlation effects in the event generation, while PYTHIA does not, it is useful in generating the signal samples used to test our measurement method.
- ALPGEN [20]: ALPGEN is a leading order matrix element generator that does not include parton showering. It is especially useful for modeling the production of electroweak vector bosons in association with energetic partons, and is used for many of our simulated samples for processes which include vector bosons. Because ALPGEN does not include parton showering, PYTHIA is used to simulate the parton showers.
- MADEVENT [21]: MADEVENT is a leading order matrix element generator that includes color flow and spin polarization effects, but does not include parton showering. It is used here to model the background processes involving the production of single top quarks. Again, PYTHIA is used to simulate the parton shower in events generated by MADEVENT.

4.2 $t\bar{t}$ Signal Modeling

In this analysis, $t\bar{t}$ events are our signal, so it is important that we have an accurate model of the $t\bar{t}$ production process. We create this model using simulated events. Having models of both the signal and background will allow us to compare simulated signal+background distributions to the data which passes our selection so that we can

ensure that our understanding of the data is accurate. We model $t\bar{t}$ production using both PYTHIA and HERWIG, allowing us to perform cross checks in multiple simulated samples.

$$N_{p\bar{p}\to X} = \epsilon \; \sigma_{p\bar{p}\to X} \int dt \; L \tag{4.1}$$

For $t\bar{t}$ production and several of our background processes, we estimate the number of events that pass our event selection using the cross section for the process, the integrated luminosity of the data sample, and the overall selection efficiency for the chosen process, which is derived from our simulated samples. The expected number of events for a given process can be determined using Equation 4.1, where ϵ is the selection efficiency, σ is the cross section (measured to be $\sigma_{t\bar{t}} = 7.50 \pm 0.48$ pb [22]), and $\int dt \; L$ is the integrated luminosity. For an integrated luminosity of 5.3 fb^{-1}, the number of predicted $t\bar{t}$ events is

$$N^{t\bar{t}} = 996.3 \pm 129.8$$

4.3 $t\bar{t}$ Background Modeling

Our event selection criteria are optimized for selecting $t\bar{t}$ events in the lepton plus jets decay channel. However, there are several other physical processes with final states that are similar to the $t\bar{t}$ lepton plus jets final state. Of the 1,260 events in our dataset which pass the event selection cuts, we expect some of them to be the result of these other background processes. These processes include: electroweak diboson production, Drell-Yan production (Z+jets), electroweak production of single top quarks, QCD production of fake $t\bar{t}$ events, W-boson plus heavy flavor jets production (W+HF), and W-boson plus light flavor jets production (W+LF). Each of these processes will be discussed in more detail below. Some of these processes are very well understood and can be modeled fully using simulated events, while others

Process	σ
WW	13.25 ± 0.25 pb
WZ	3.96 ± 0.06 pb
ZZ	1.58 ± 0.02 pb

Table 4.1. Cross Sections for Diboson Production

are not as well understood theoretically and are modeled using real data collected by the CDF detector [17, 23].

4.3.1 Electroweak Diboson Production

The electroweak interaction can produce events with pairs of vector bosons: WW, WZ, and ZZ events. Some of these events are able to pass our selection criteria because they contain a real lepton and neutrino (from the decay of a W boson) as well as multiple jets (from the decay of the second boson). These diboson backgrounds are simulated using the PYTHIA event generator. The number of events expected in our sample is again calculated using Equation 4.1. The cross sections for the various diboson processes are shown in Figure 4.1 [24].

Using this information, we find the total predicted number of diboson events that will pass our selection to be

$$N^{Diboson} = 19.5 \pm 1.3$$

4.3.2 Drell-Yan Production

The electroweak Drell-Yan production of a Z boson can be accompanied by several jets. In this case, particularly when the boson decays via $Z \rightarrow \tau\tau$, the final state of such an event could pass our event selection, thanks to the presence of a real lepton and neutrino (from a τ lepton decay) as well as multiple jets. We model this Z+jets production using the ALPGEN event generator, with the parton showering performed by PYTHIA. The overall normalization is determined in the same way as for the electroweak diboson production. The contribution from this particular background

Process	σ
Single Top T-Channel	1.98 ± 0.08 pb
Single Top S-Channel	0.88 ± 0.05 pb

Table 4.2. Cross Sections for Single Top Quark Production

process is fairly small (the cross section for $Z \rightarrow \tau\tau$ is $\sigma = 13.0 \pm 1.5$ pb [24]), but it is non-negligible. The total predicted number of Drell-Yan events in our sample of candidate $t\bar{t}$ events is

$$N^{Z+Jets} = 8.8 \pm 0.9$$

4.3.3 Electroweak Single Top Production

This analysis studies top quarks produced in pairs by the QCD interaction, but the electroweak force can also produce top quarks paired with a bottom quark. When this occurs, these single top quarks form a background for our analysis. There are two electroweak processes that can produce single top quarks at the Tevatron. The first, called s-channel production, occurs when a virtual W boson decays via $W^* \rightarrow tb$. The second process, t-channel single top production, occurs when a W boson interacts with a bottom quark in the "sea" of quarks inside the proton, producing a top quark. Figures 4.1 and 4.2 depict s-channel and t-channel single top production respectively.

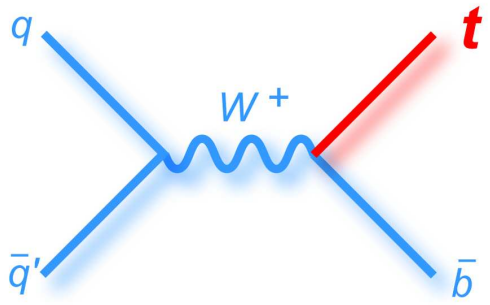

Figure 4.1. S-channel Single Top Production

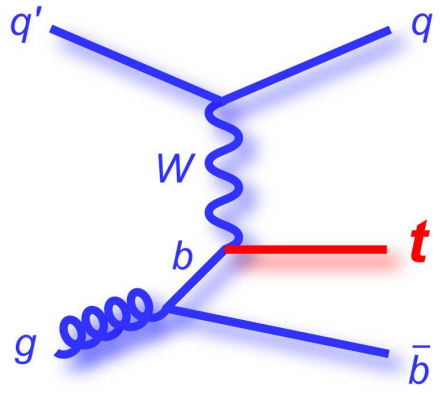

Figure 4.2. T-channel Single Top Production

Because these events contain one real top quark, as well as extra jets, they are often able to pass our event selection. We model single top production using the MadEvent event generator, with the parton showering performed by pythia. The normalization for the single top quark contribution to the total background is found using Equation 4.1, with the cross sections given in Table 4.2 [24]. The cross sections are small, but because these events look very much like $t\bar{t}$ events, they still make a sizable contribution to our overall background, with the predicted number of single top quark events passing our selection given by

$$N^{SingleTop} = 15.6 \pm 0.9$$

4.3.4 QCD

The vast majority of collisions at the Tevatron involve only the QCD interaction. Without any electroweak process taking place, such events will not involve any W bosons. Because of this, they will not include any real leptons or neutrinos with large energy, so our event selection removes an overwhelming majority of these events. However, these events can occasionally pass our event selection by containing both a jet that happens meets all of our lepton selection cuts and a significant amount of missing transverse energy – usually due to the mis-measurement of jet energies. The probability that any individual QCD event will meet both these requirements and pass our event selection is very small, but because there are so many QCD events produced at the Tevatron, they form one of the largest backgrounds for the $t\bar{t}$ events we are studying.

Only QCD events with very specific characteristics will be able to produce both a fake lepton and fake missing transverse energy. Because these things require both mis-identification of a lepton and mis-measurement of energy in the detector, it is difficult to verify that our detector simulation properly models these effects. There-

fore, rather than using simulated samples to model this background, we use the data itself. To do so, we work with the "jet electron" dataset, which is created using selection criteria similar to what is used for this analysis, except that there is no $\not\!\!E_T$ cut and, instead of tight leptons, we select jet electrons. These jet electrons are defined as jets containing at least four tracks in the COT, but which deposit most of their energy in the electromagnetic calorimeter. The jet electrons meet the requirements for electron identification, except for the fact that they contain multiple tracks and are thus unlikely to be real electrons. The presumption is that QCD events in the jet electron dataset are similar kinematically to QCD events where there is a jet that actually does get identified as a tight electron.

In order to determine the normalization of the QCD background, a fit is performed to the $\not\!\!E_T$ distribution in the data using the jet electron sample as one template and a W+jets simulated sample as a second template. This determines the expected QCD fraction in the data, and by then applying our $\not\!\!E_T$ cut, we can determine the number of expected QCD events that will pass our selection. This prediction is

$$N^{QCD} = 67.5 \pm 29.6$$

4.3.5 W + Heavy Flavor

The W + heavy flavor background processes are those which produce a real W boson as well as heavy quarks ($W + b\bar{b}$, $W + c\bar{c}$, and $W + c$). These events contain a real W boson which can decay leptonically to produce a real lepton and missing transverse energy. They also contain multiple jets, and due to the presence of real bottom quarks, our b-tagging requirement does not significantly reduce this background. As a result, these events form the largest portion of our overall background model.

The W + heavy flavor background component is modeled using ALPGEN, with the parton showering performed by PYTHIA – the combination of these generators gives

the overall shape of this background distribution. Because it is difficult to determine the theoretical cross section for the production of W bosons in association with various numbers of jets, we do not estimate the normalization for this background process using Equation 4.1. Instead, we start with the pretag data sample, which is the sample we find when we impose all of our selection cuts except for requiring at least one jet to be tagged as a b jet. Starting from this sample, the expected number of W + heavy flavor events in our signal sample can be calculated using Equation 4.2.

$$N^{W+HF} = (N_{pretag} - N_{QCD} - N_{Diboson} - N_{Z+Jets} - N_{SingleTop} - N_{t\bar{t}})\ f_{HF}\ \epsilon_{tag} \quad (4.2)$$

Starting with the pretag sample, the number of predicted QCD, diboson, Drell-Yan, single top, and $t\bar{t}$ events is subtracted, giving us an estimate of the number of events containing a W boson and jets. Simulated ALPGEN samples are used to calculate the fraction f_{HF} of these events with heavy flavor quarks. The result is then multiplied by the b-tagging efficiency ϵ_{tag}. In this way, while simulated samples are used to find the heavy flavor fraction f_{HF}, the absolute normalization is determined directly from the pretag data. The total number of W + heavy flavor events predicted using this method is

$$N^{W+HF} = 135.5 \pm 35.2$$

4.3.6 W + Light Flavor

The final background component in our sample is made up of processes which produce a real W boson in association with light quarks. As with the W + heavy flavor background, the W + light flavor processes produce events with a real W boson, which can decay into a lepton and neutrino, as well as multiple jets. However, in this case, there are no real bottom jets in the event. Two poorly reconstructed jets can

have tracks that cross near the primary vertex giving the appearance of a secondary vertex. This can be identified as a bottom jet – called a "mistagged" jet. Some jets have a negative secondary vertex, which cannot come from a physical bottom quark. Assuming that all tagged events with a negative secondary vertex are mistagged events, one can determine the ratio of mistags to tags and use the ratio to model mistags in a given sample based on jet properties.

We again use ALPGEN, with the parton showering performed by PYTHIA, to model the W + light flavor background. In order to determine the appropriate normalization of this background, we first consider the secondary vertex that is the basis of our b-tagging algorithm. If we let the distance from the primary vertex to the secondary vertex be T, the path of the decaying particle be $\vec{d}$, and the direction of the jet be $\hat{j}$, then for a real secondary vertex, we should have $T = \vec{d} \cdot \hat{j} > 0$ because the decaying particle must be traveling in the same direction as the jet. If we consider a sample of jets with no measurable lifetime (like those in the W + light flavor sample), the distribution of T will be symmetric around 0, but not exactly 0 because of the finite detector resolution. Thus a mistagged jet is equally likely to have $T > 0$ or $T < 0$. Since no real process can produce a secondary vertex with $T < 0$, the number of such vertices in our data can be used to estimate the number of mistagged jets with $T > 0$ in our candidate events.

The rate of secondary vertex tags with $T < 0$ is measured in the data and parameterized by six jet variables: jet E_T, the number of good SVX tracks in the jet, the total E_T for all jets in the event, the jet η, the number of reconstructed primary vertices in the event, and the z-coordinate of the jet's primary vertex [23]. Using these variables, we can determine N^{mis}, the number of mistagged events predicted in the pretag sample. We can then multiply this number by the estimate for the fraction of W + light flavor events in the pretag sample, as in Equation 4.3, to determine the expected number of W + light flavor events to pass the selection.

$$N^{W+LF} = N^{mis} \frac{N_{pretag} - N_{t\bar{t}} - N_{QCD} - N_{W+HF} - N_{Diboson} - N_{Z+Jets} - N_{SingleTop}}{N_{pretag}} \tag{4.3}$$

The final result of this estimate is that we expect W + light flavor to be our third largest background component, with a predicted number of events given by

$$N^{W+LF} = 45.2 \pm 9.8$$

4.4 Overall Event Simulation Model

Our overall background model is determined by summing the predictions for all of the various background processes. The various backgrounds and their respective normalizations are shown in Table 4.3, giving a total background prediction of 283.3± 91.2 events.[1] If we add in the expected $t\bar{t}$ events, our prediction for the total number of observed events becomes 1279.6 ± 158.6, which is in good agreement with the 1260 events that pass the selection cuts. The signal to background ratio is approximately 3.5:1.

Process	Events
Signal Prediction	996.3 ± 129.8
WW/WZ/ZZ	19.5 ± 1.3
Z+Jets	8.8 ± 0.9
Single Top	15.6 ± 0.9
W + HF Jets	135.5 ± 35.2
Non-W (QCD)	67.5 ± 29.6
Mistags (W+LF)	45.2 ± 9.8
Total Background Prediction	283.3 ± 91.2
Signal+Background Prediction	1279.6 ± 158.6

Table 4.3. Summary of Simulation Model Predictions

[1]Errors for each background sample are derived from systematic uncertainties in their method of calculation, so they are not independent and cannot be summed in quadrature to form a total error. Instead, the error from each source (e.g., jet-energy scale – discussed in more detail in Section 10) must be propagated through each sample to arrive at a final calculation.

CHAPTER 5

Reconstructing $t\bar{t}$ Events

We have identified $t\bar{t}$ candidate events with a lepton, four jets, and large missing energy, as described in Chapter 3. In this lepton plus jets decay channel, one top, called the leptonic top, decays via $t \to Wb \to \ell\nu b$, and the other, the hadronic top, decays via $t \to Wb \to udb$. Our measurement will require us to use these identified decay products to measure rapidity values, as measured in the top quark and $t\bar{t}$ rest frames. In order to do this, we must be able to fully reconstruct the $t\bar{t}$ kinematics for each event, matching each final state jet with the appropriate top decay product and using simple constraints to determine the t and $\bar{t}$ momentum vectors [17].

5.1 Kinematic Reconstruction

The final state of a $t\bar{t}$ event in our selected decay channel contains a lepton, a neutrino, two bottom quarks, one up-type quark, and one down-type quark. There are several difficulties in trying to match the objects observed in the detector to these final state partons. The lepton and the quark jets can be directly observed in the detector, but for the neutrino, we can measure only the transverse component of its momentum, P_T, which is the source of the $\not\!\!E_T$ – the P_z must be inferred. The detector can tag jets from bottom quarks, but otherwise it cannot determine which jet is created by a given type of quark, so another problem in reconstructing the event from the available information is determining the correct assignment of jets to partons from all of the possible combinations. These combinations are subject to the constraints

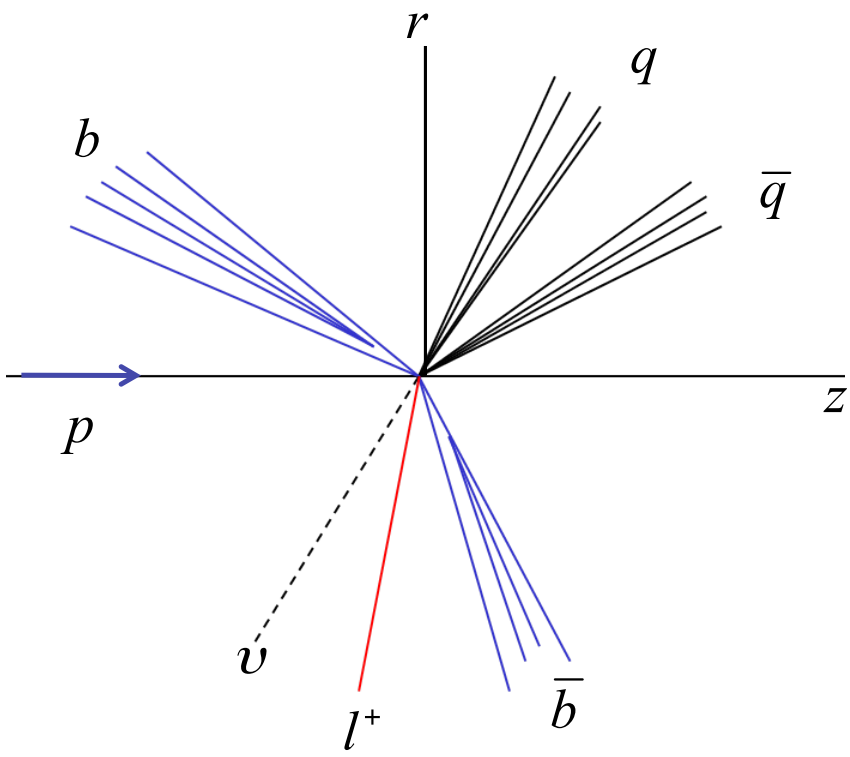

Figure 5.1. A $t\bar{t}$ event in the r-z plane.

of the assumption that the event is a $t\bar{t}$ event: the mass of the two jets are consistent with the W boson mass, $M_W = 80$ GeV/c^2, the mass of the lepton and neutrino, $M_{\ell\nu}$ is consistent with M_W, and the underlying top quarks each have a mass of 172.5 GeV/c^2.

Our reconstruction assumes that the four highest energy jets in the event come from the four final state quarks. Ignoring any b-tagging information for now, there are 24 possible combinations for matching the four quarks to the four observed jets. However, interchanging the up and down quarks from the hadronically decaying W boson has no effect on the overall kinematics for the t and $\bar{t}$, so the number of unique combinations is reduced from 24 to 12.

The $\not\!\!E_T$ can be used to determine the components p_x and p_y of the neutrino momentum. Unfortunately, we cannot know the portion of the proton and antiproton momenta carried by the initial colliding partons, so we do not know the total mo-

mentum of the event along the beam direction, p_z. This means we cannot directly measure the z-component of the neutrino momentum. It is possible, however, to calculate the neutrino p_z from other information available in the event. Because the lepton and neutrino are the only two decay products of the leptonically decaying W, when their momenta are added, they should form a particle whose mass is consistent with that of the W boson. This equality involves a quadratic term, and thus solving it produces two possible solutions for the neutrino p_z. The kinematic reconstruction considers both possible solutions, and therefore the number of possible combinations for the event kinematics is increased again from 12 to 24.

To determine the correct combination, we evaluate how closely each possible combination matches the expectation that it is the final state of a $t\bar{t}$ decay. We expect such a final state to have four basic characteristics:

- The lepton and neutrino should be the decay products of a W boson, $W \to \ell\nu$
- Two of the jets should be the decay products of another W boson, $W \to jj$
- The lepton, neutrino, and a third jet should be the decay products of a top quark, $t \to \ell\nu j$
- The two jets from the W boson and the fourth jet should also be the decay products of a top quark, $t \to jjj$

The degree to which each of the 24 combinations is compatible with these requirements is evaluated using a χ^2 test, with the χ^2 function given in Equation 5.1.

$$\begin{aligned}\chi^2 \;=\; & \sum_{i=\ell,jets} \frac{(p_T^{i,meas} - p_T^{i,fit})^2}{\sigma_i^2} + \sum_{j=x,y} \frac{(p_j^{UE,meas} - p_j^{UE,fit})^2}{\sigma_j^2} \\ & + \frac{(M_{jj} - M_W)^2}{\Gamma_W^2} + \frac{(M_{\ell\nu} - M_W)^2}{\Gamma_W^2} + \frac{(M_{bjj} - M_{fit})^2}{\Gamma_t^2} + \frac{(M_{b\ell\nu} - M_{fit})^2}{\Gamma_t^2}\end{aligned} \tag{5.1}$$

The first term in Equation 5.1 is a sum over the lepton and jet transverse energies, while the second term is a sum over the "unclustered" energy, which consists of all the

measured energy in the event that is not part of the actual $t\bar{t}$ decay. When evaluating the χ^2 function, small corrections to the energies of each object are made by varying them within the experimental resolution. This improves the energy resolution and increases the probability of finding the correctly matched combination.

The final four terms in Equation 5.1 are the constraints imposed by the assumption that the event is a $t\bar{t}$ event. M_{jj} is the mass of the two jets. The mass of the lepton and neutrino is given by $M_{\ell\nu}$. $M_{b\ell\nu}$ and M_{bjj} are the invariant masses of the decay particles from the leptonically and hadronically decaying top quarks. The kinematic reconstruction can be used to measure a top quark mass M_{fit}, but instead we include the constraint $M_{fit} = M_t = 172.5$ GeV/c^2 to help improve the reconstruction. The denominators in these constraints are the W boson and top quark decay widths, but do not include a factor for the experimental resolution of the lepton and jets because this resolution has already been accounted for in the first term of Equation 5.1 [25].

The package MINUIT [26] is used to find the solution that minimizes the χ^2 function for each of the 24 possible combinations. At this point we use the b-tagging information in each event to require that any b-tagged jets also be matched to one of the original bottom quarks. The combination that meets this requirement and has the smallest χ^2 value is then chosen as the best candidate for describing the true $t\bar{t}$ final state.

5.2 Reconstruction Validation

It is important to verify that the event reconstruction is performed adequately and that the results are modeled well. In this section, we examine the agreement of the data with the prediction in the distributions of important kinematic variables as well as the reconstructed variables; there is reasonable agreement in all cases. For each plot, a Kolmogorov-Smirnov (KS) test is performed to check the similarity between

the data the predicted samples across all bins [27].[1] The result of each KS test shows that the data and the model are in agreement at a two-σ confidence level. We can now proceed with our analysis comfortable with the agreement between the data and the predicted model.

5.2.1 Detector Variables and Observables

Before passing any detector objects to the kinematic fitter and doing the reconstruction, the detector variables and observables need to be checked. These include the four jets, the lepton, and the missing transverse energy. We use the transverse energy to check the transverse component of the variables and the rapidity to check the longitudinal component of the variables. For the missing transverse energy, which has no longitudinal component, the ϕ distribution is used as a secondary check.

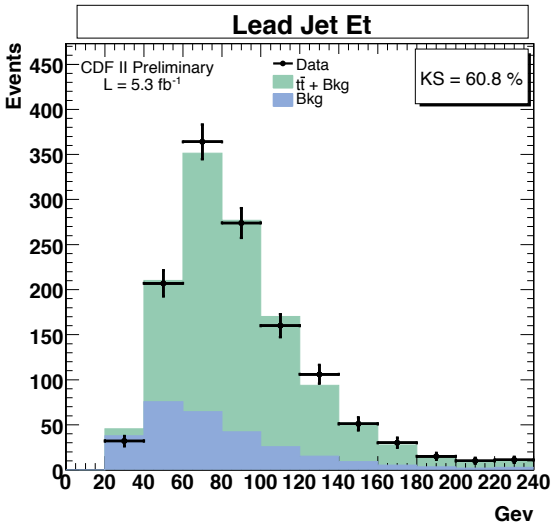

Figure 5.2. Lead jet transverse energy

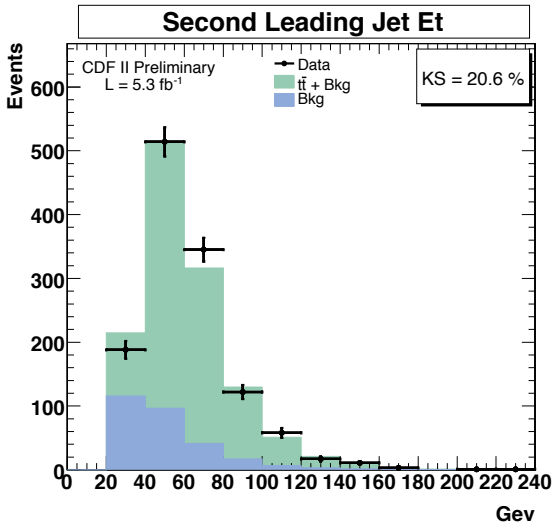

Figure 5.3. Second leading jet transverse energy

[1]The KS test checks the cumulative distribution in the histograms of the two samples. For a given bin, the cumulative fraction of each sample is calculated and the values are checked between the two samples. The KS test represents the largest deviation between these two fractions across the entire range of the distributions making it a more robust check than the mean or the RMS.

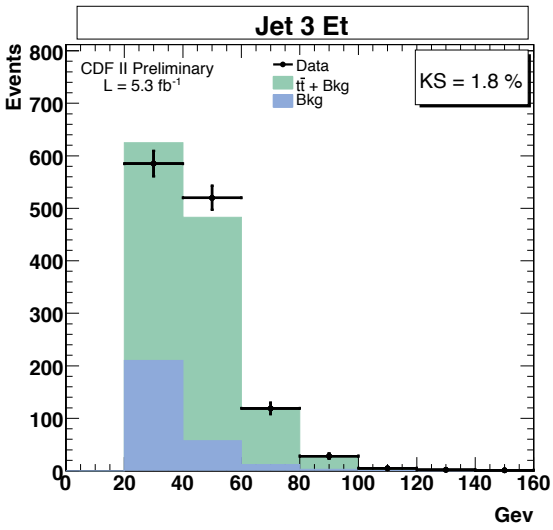

Figure 5.4. Third leading jet transverse energy

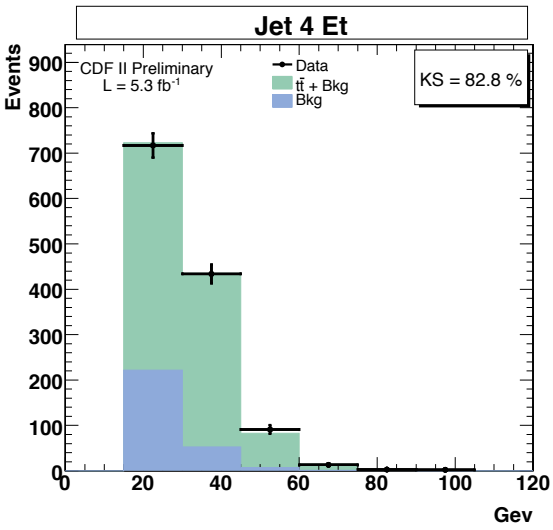

Figure 5.5. Fourth leading jet transverse energy

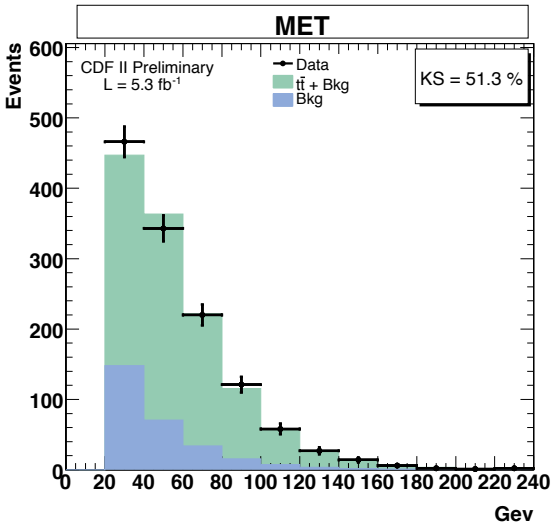

Figure 5.6. Missing transverse energy

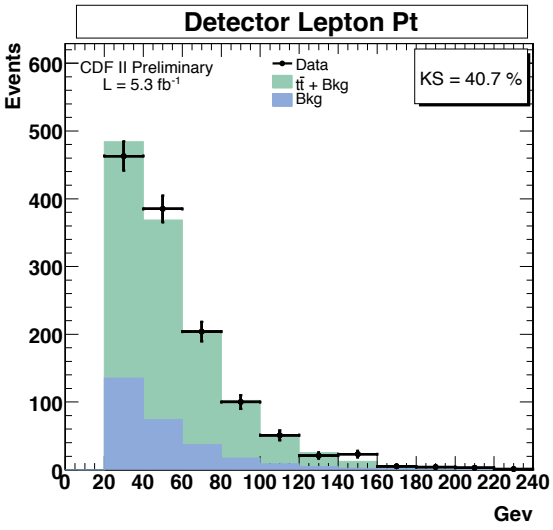

Figure 5.7. Lepton p_T

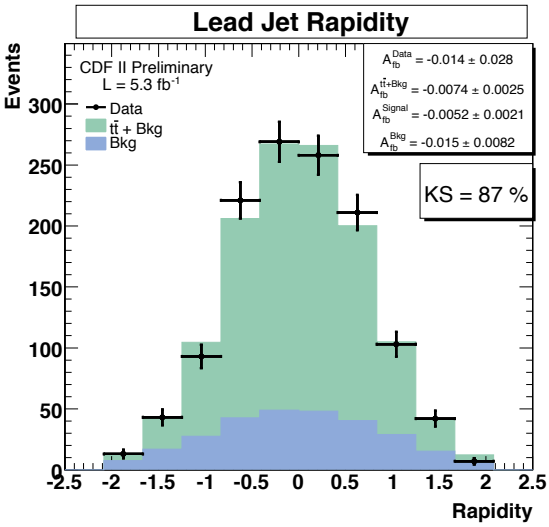

Figure 5.8. Leading jet rapidity

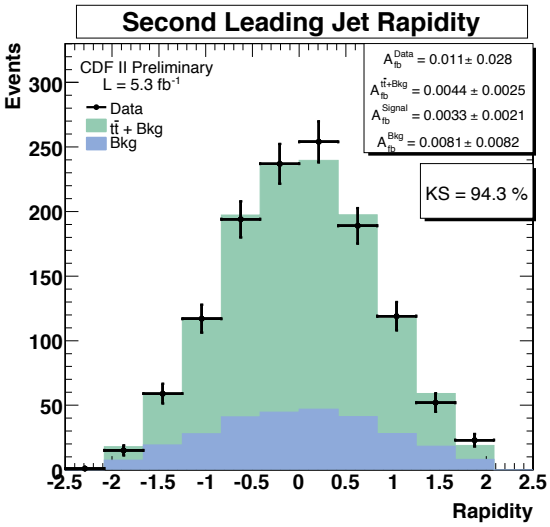

Figure 5.9. Second leading jet rapidity

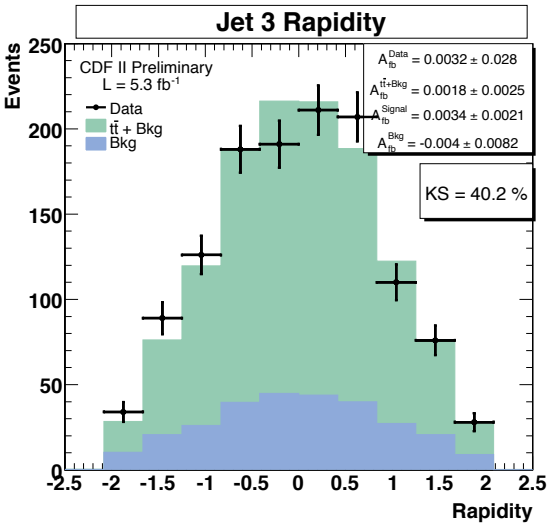

Figure 5.10. Third leading jet transverse energy

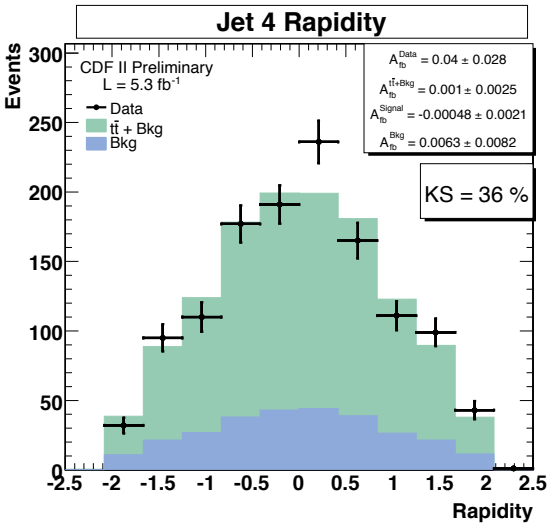

Figure 5.11. Fourth leading jet rapidity

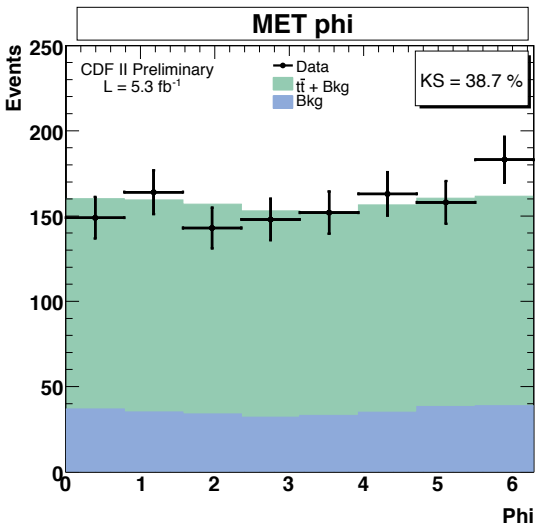

Figure 5.12. Missing transverse energy ϕ

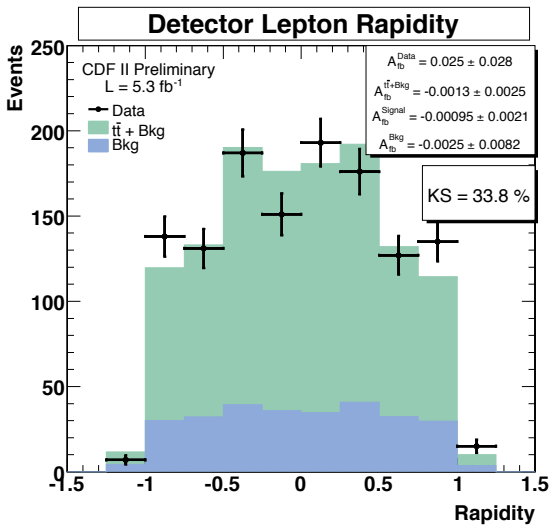

Figure 5.13. Lepton rapidity

5.2.2 Kinematic Fitter and Reconstructed Variables

Once the detector variables and observables are checked, the kinematic fitter and reconstructed variables can be checked. These include the hadronic and leptonic W bosons, the hadronic and leptonic bottom quarks, the neutrino, and the $t\bar{t}$ pair. We use the transverse energy to check the transverse component of the variables and the rapidity to check the longitudinal component of the variables (except where it is convenient to check the longitudinal momentum, as with the neutrino and the $t\bar{t}$ system).

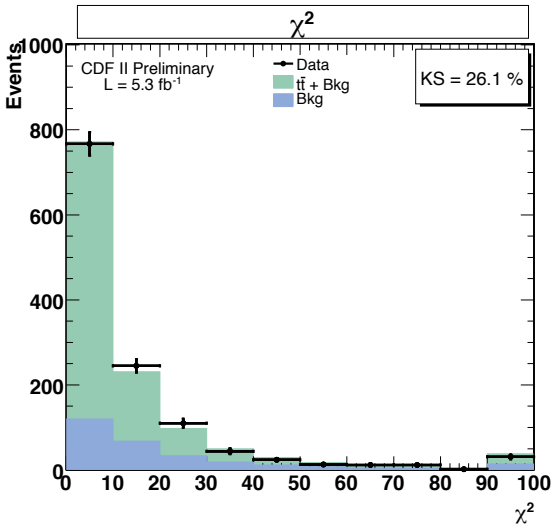

Figure 5.14. Event χ^2.

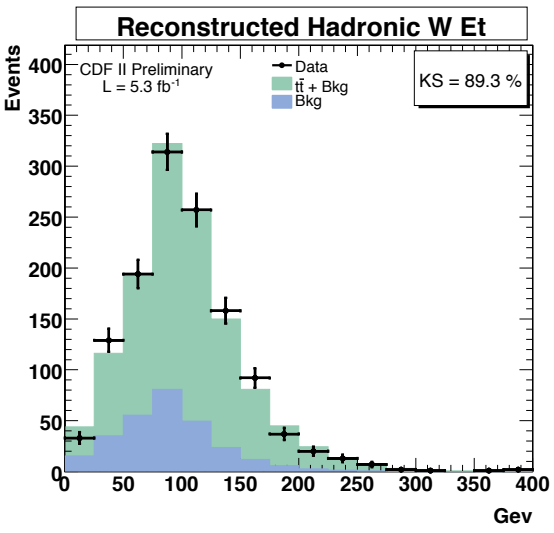

Figure 5.15. Hadronic W transverse energy

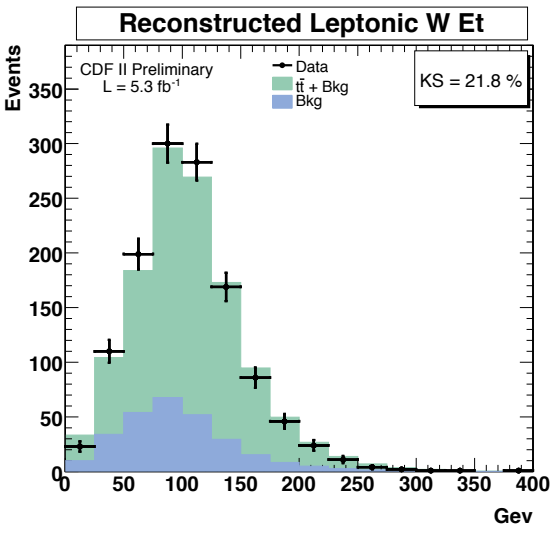

Figure 5.16. Leptonic W transverse energy

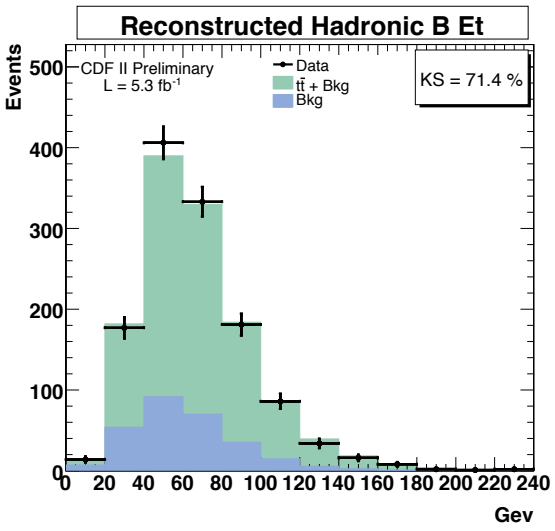

Figure 5.17. Hadronic B transverse energy

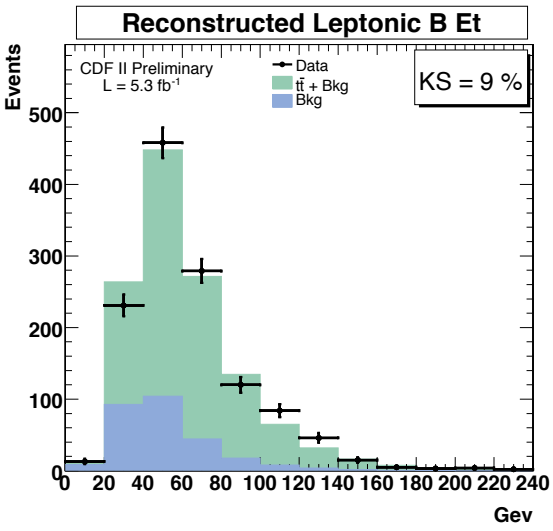

Figure 5.18. Leptonic B transverse energy

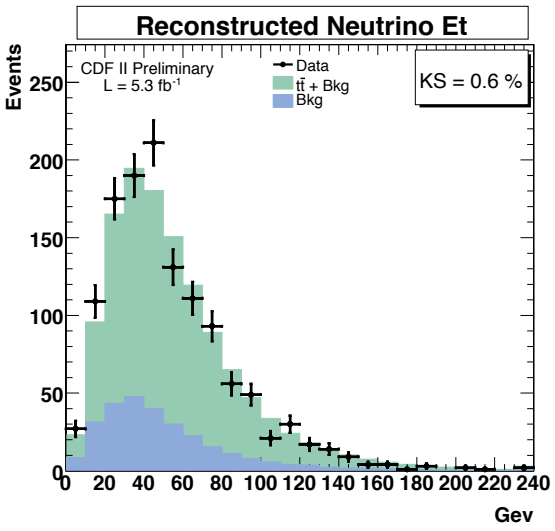

Figure 5.19. Neutrino transverse energy

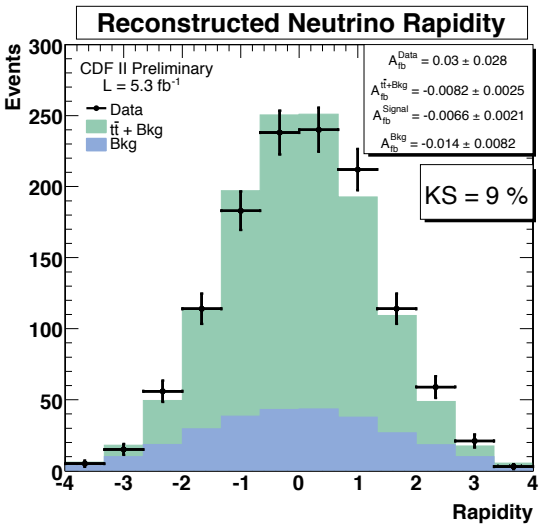

Figure 5.20. Neutrino rapidity

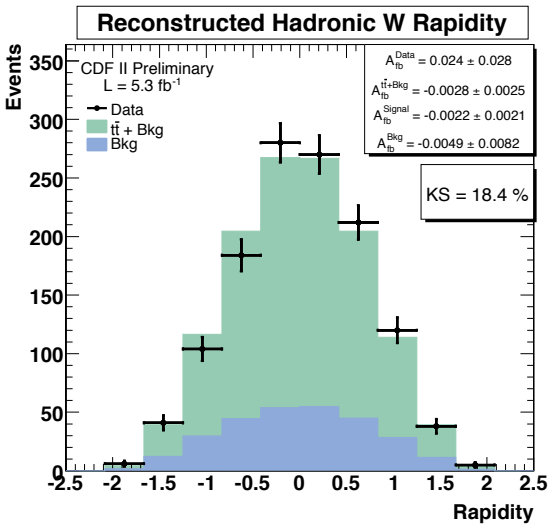

Figure 5.21. Hadronic W rapidity

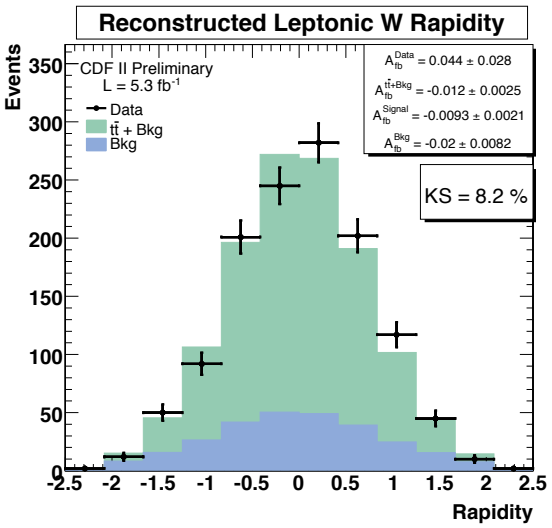

Figure 5.22. Leptonic W rapidity

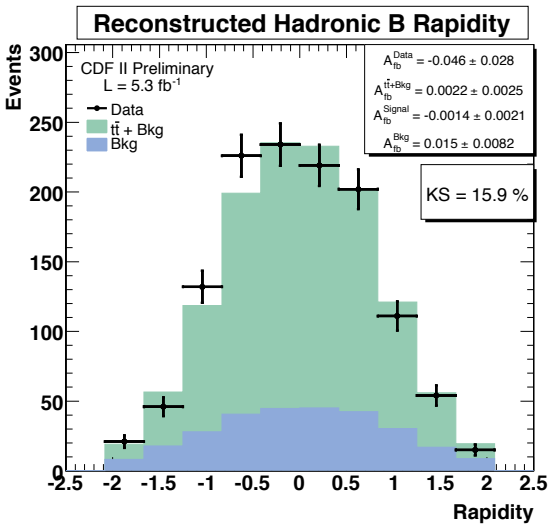

Figure 5.23. Hadronic B rapidity

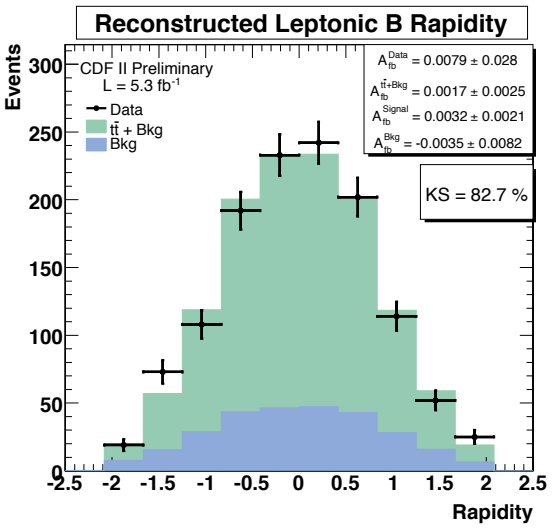

Figure 5.24. Leptonic B rapidity

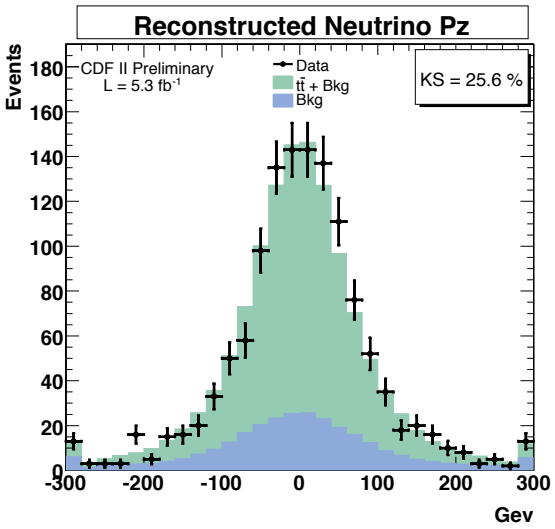

Figure 5.25. Neutrino longitudinal momentum

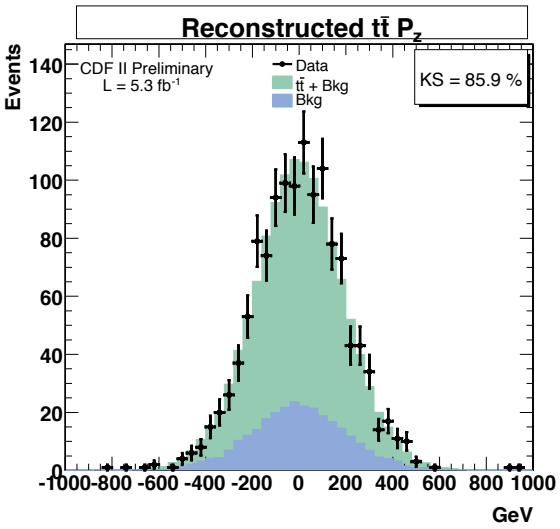

Figure 5.26. $t\bar{t}$ longitudinal momentum

CHAPTER 6

The Inclusive Forward-Backward Asymmetry

Before describing the forward-backward asymmetry as a function of mass, we will describe the main features of the inclusive effect and variables for the study. We will also review the correction procedure for the inclusive analysis which will then be extended for the mass-dependent analysis.

6.1 Rapidity Variables

The charge asymmetry appears as a difference between the distributions of t and $\bar{t}$ production angles or rapidities. In lepton plus jet events, the t and $\bar{t}$ have distict signatures: one is a "leptonic" decay and a one is a "hadronic" decay. The t or $\bar{t}$ assignments are different according to the lepton charge q_l:

$\mathbf{q_l}$	$\mathbf{t_{lep}}$	$\mathbf{t_{had}}$
$+$	t	$\bar{t}$
$-$	$\bar{t}$	t

Table 6.1. The leptonic and hadronic systems in events with positive and negative leptons

The leptonic and hadronic systems have different experimental complications. The leptonic system has that well measured lepton with limited rapidity range $\mid \eta \mid \leq 1.0$, a $\not\!\!E_T$ which is correlated to the hadronic system, and the unconstrained longitudinal neutrino momentum that must be derived in the fit. The hadronic decay has 3 jets with acceptance out to $\mid \eta \mid \leq 2.0$, modest energy resolution, excellent direction

resolution, and no correlation with the leptonic system. Either or both systems could contain a b-tagged jet confined to central region $\mid \eta \mid \leq 1.0$.

The centrality of the b-tag and lepton ID create the possibility of acceptance biases. For example, in an event with a b-tagged leptonic decay, all of the leptonic measurables are centrally confined. This limits the rapidity range of the leptonic top, while meanwhile for the hadronic top system all its jets can extend to $\mid \eta \mid \leq 2.0$. In order to control effects of this kind, our treatment of top rapidity variables keeps the leptonic vs. hadronic distinction primary, with the conversion to t and $\bar{t}$ following according to Table 6.1.

The most direct measurement of the "top direction" is the lab rapidity of the hadronic top system, y_h. In events with a negative lepton, y_h is the lab rapidity of the t quark, $y_t^{p\bar{p}}$. In events with a positive lepton, y_h is the rapidity of the $\bar{t}$ quark, $y_{\bar{t}}^{p\bar{p}}$. If CP is good, $y_{\bar{t}}^{p\bar{p}} = -y_t^{p\bar{p}}$, and we can combine both samples by weighting with the lepton charge. Keeping in mind that half the sample is hadronic $y_{\bar{t}}^{p\bar{p}}$ going the other way, we therefore consider $-qy_h$ equivalent to $y_t^{p\bar{p}}$, the rapidity of the top quark in the lab frame. $y_t^{p\bar{p}}$ has good directional precision and η acceptance, at the cost of including an unknown boost from the $q\bar{q}$ frame to the $t\bar{t}$ frame. The resulting bin-to-bin smearing in $y_t^{p\bar{p}}$ can be corrected for on average, and this is a major component in the unfold to the parton-level asymmetry.

An alternative, frame independent, variable is the rapidity difference of the leptonic and hadronic systems $\Delta y_{lh} = y_l - y_h$. After multiplication by the lepton charge q, this variable measures the frame independent difference between the top and anti-top rapidities:

$$
\begin{aligned}
q\Delta y_{lh} &= q y_l - q y_h && (6.1)\\
&= y_t^{p\bar{p}} - y_{\bar{t}}^{p\bar{p}} && (6.2)\\
&= y_t - y_{\bar{t}} && (6.3)\\
&= \Delta y && (6.4)
\end{aligned}
$$

$q\Delta y_{lh} = \Delta y$ uses all of the information in the event, at the cost of adding uncertainty from the $\not\!\!E_T$ and unknown longitudinal motion of the leptonic side. It has the the advantage of compensating for the $t\bar{t}$ system motion, and is thus more directly interpretable without the need of unfolding. Most importantly, however, Δy is proportional to $y_t^{t\bar{t}}$, the top rapidity in the $t\bar{t}$ rest frame. To see this, transform the top rapidity in the lab frame back to the $t\bar{t}$ rest frame by subtracting the motion of the $t\bar{t}$ system, $y_{t\bar{t}}$:

$$
\begin{aligned}
y_t^{t\bar{t}} &= y_t^{p\bar{p}} - y_{t\bar{t}} && (6.5)\\
&= y_t^{p\bar{p}} - \frac{1}{2}(y_t^{p\bar{p}} + y_{\bar{t}}^{p\bar{p}}) && (6.6)\\
&= \frac{1}{2}(y_t^{p\bar{p}} - y_{\bar{t}}^{p\bar{p}}) && (6.7)\\
&= \frac{1}{2}(y_t - y_{\bar{t}}) && (6.8)\\
&= \frac{1}{2}\Delta y && (6.9)
\end{aligned}
$$

The top quark rapidity in the $t\bar{t}$ rest frame is a function of the top quark production angle $\cos(\theta^*)$ in that frame. Since the transformation from angles to rapidities preserves sign, an asymmetry in $q\Delta y_{lh}$ is identical to an asymmetry in the top quark production angle in the $t\bar{t}$ rest frame. Thus, while $-qy_h = y_t^{p\bar{p}}$ is most experimentally straightforward, $q\Delta y_{lh} = \Delta y$ contains the physics that will be strongly correlated to the mechanism of the asymmetry. For this reason we will use Δy and Δy_{lh} as

our primary rapidity variable, although we will continue to monitor y_h and $-qy_h$ as important cross-checks.

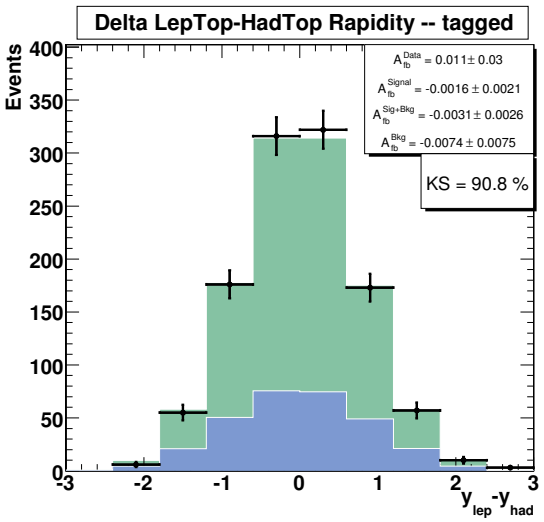

Figure 6.1. Rapidity distributions in data compared to the Pythia+M24U prediction. Left: $\Delta y_{lh} = Y_{lep} - Y_{had}$ Right: Y_{had}

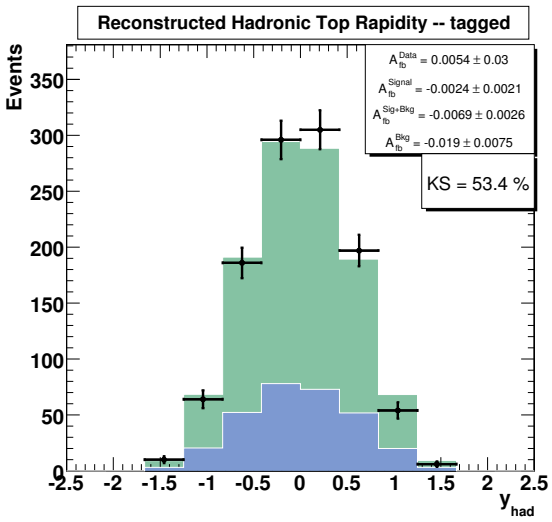

Figure 6.2. Angle between bottom-down and bottom-up quarks in W rest frame

6.2 Asymmetry Measurement

We show the inclusive y_h and Δy_{lh} distributions in Fig. 6.1. The asymmetries in the data, the signal model, the background model, and the combined signal+background prediction are shown in the legend on the top right. In this paper all asymmetries and their uncertainties use the standard forms:

$$A = \frac{F-B}{F+B} = \frac{F-B}{N} \tag{6.10}$$

$$\sigma_A = \sqrt{\frac{4FB}{N^3}} \tag{6.11}$$

$$= \sqrt{\frac{1-A^2}{N}} \tag{6.12}$$

The error of the asymmetry in Equation 6.2 follows from the binomial nature of the asymmetry.

The distributions in Fig. 6.1 contain the full sample of both lepton signs and should be symmetric. For both variables the data agrees very well with prediction, and, in particular, the asymmetries in are consistent with zero.

The asymmetry becomes apparent when the sample is partitioned by charge.

We define the charge asummetry in Δy_{lh}:

$$A_{lh}^{\pm} = \frac{N^{\pm}(\Delta y_{lh} > 0) - N^{\pm}(\Delta y_{lh} < 0)}{N^{\pm}(\Delta y_{lh} > 0) + N^{\pm}(\Delta y_{lh} < 0)} \tag{6.13}$$

Note that this is before the sign weighting, $\Delta y_{lh} = y_l - y_h$. Note also that we streamline our notation: $A = A_{\text{rest}}$. Fig. 6.3 shows the Δy_{lh} distributions for events with negative leptons and Fig. 6.4 with positive leptons. We find $A_{lh}^{+} = 0.084 \pm 0.043$ and $A_{lh}^{-} = -0.057 \pm 0.041$, equal and opposite with modest significance. The difference of these values is 0.141 ± 0.059. Comparison of the positive and negative shapes to each other with the standard CDF KS test gives KS = 2%.

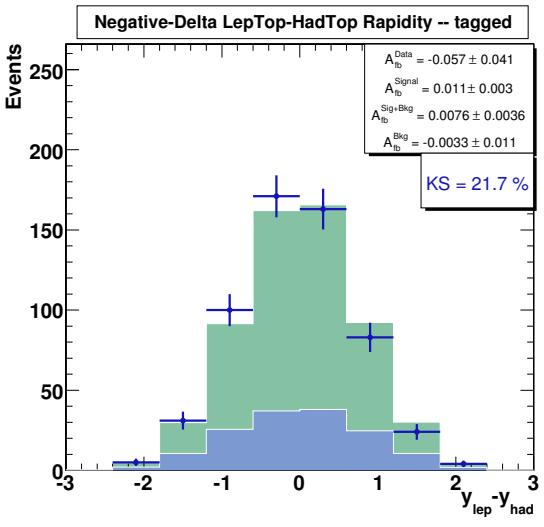

Figure 6.3. Δy_{lh} distribution for events with negative leptons

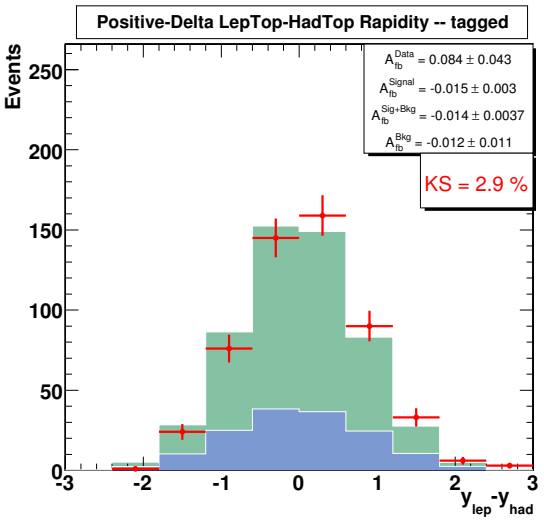

Figure 6.4. Δy_{lh} distribution for events with positive leptons

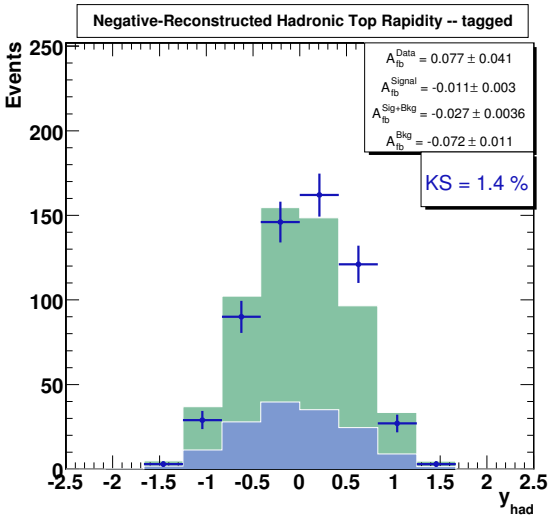

Figure 6.5. Y_{had} distribution for events with negative leptons

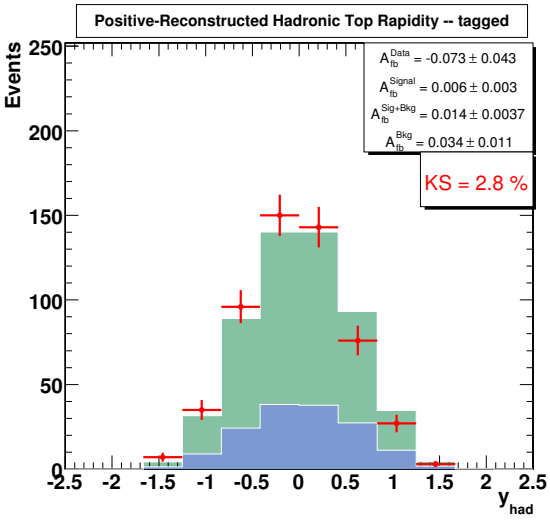

Figure 6.6. Y_{had} distribution for events with positive leptons

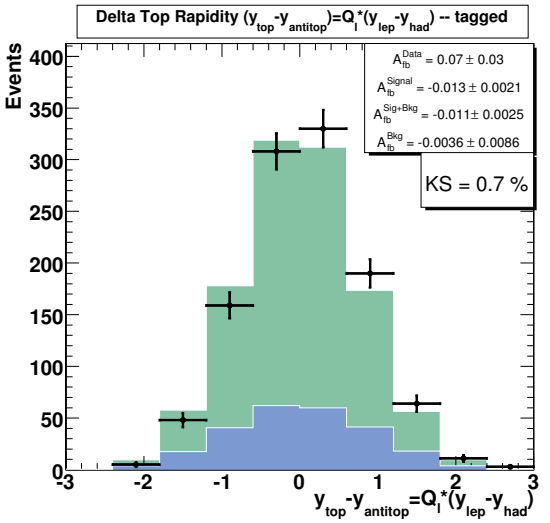

Figure 6.7. $q\Delta y_{lh}$ distribution in data vs prediction.

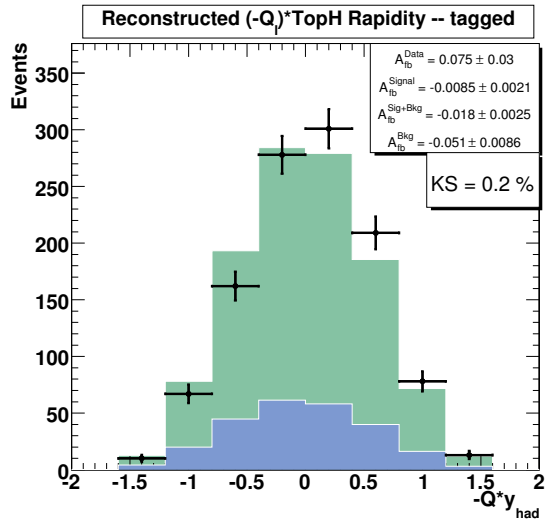

Figure 6.8. qY_{had} distribution in data vs prediction.

We also define the charge asymmetry in hadronic top system:

$$A_h^{\pm} = \frac{N^{\pm}(y_h > 0) - N^{\pm}(y_h < 0)}{N^{\pm}(y_h > 0) + N^{\pm}(y_h < 0)} \tag{6.14}$$

Fig. 6.5 shows the y_h distributions for events with negative leptons and Fig. 6.6 negative leptons (right). Using Table 6.1, this figure suggests a preference for the t quarks to move in the proton (forward) direction and the $\bar{t}$ quarks to move in the $\bar{p}$ direction. The measured asymmetries are $A_h^+ = -0.073 \pm 0.043$ and $A_h^- = -0.078 \pm 0.041$, equal and opposite with moderate statistical significance. The difference of the values is 0.151 ± 0.059. Comparison of the positive and negative shapes to each other with the standard CDF KS test gives KS = 0%.

We measure the total CP conserving asymmetry by combining the separate charge samples after weighting the distributions by lepton charge q, so that in the sense of Table 6.1, and assuming the CP consistent inversion $y_t = -y_{\bar{t}}$, $-qy_h = y_t$ and $q\Delta y_{lh} = y_t - y_{\bar{t}}$

We define the frame independent asymmetry

$$A^{t\bar{t}} = \frac{N(q\Delta y_{lh} > 0) - N(q\Delta y_{lh} < 0)}{N(q\Delta y_{lh} > 0) + N(q\Delta y_{lh} < 0)} \tag{6.15}$$

$$= \frac{N((y_t - y_{\bar{t}}) > 0) - N((y_t - y_{\bar{t}}) < 0)}{N((y_t - y_{\bar{t}}) > 0) + N((y_t - y_{\bar{t}}) < 0)} \tag{6.16}$$

$$\tag{6.17}$$

and the lab frame asymmetry

$$A^{p\bar{p}} = = \frac{N(qy_h > 0) - N(y_h < 0)}{N(qy_h > 0) + N(qy_h < 0)} \tag{6.18}$$

$$= \frac{N(y_t > 0) - N(y_t < 0)}{N(y_t > 0) + N(y_t < 0)} \tag{6.19}$$

$$\tag{6.20}$$

The distributions of these variables are shown in Fig. 6.7. The frame dependent asymmetry is $A^{t\bar{t}} = 0.070 \pm 0.030$, and the inclusive asymmetry in the lab frame is $A^{p\bar{p}} = 0.075 \pm 0.030$.

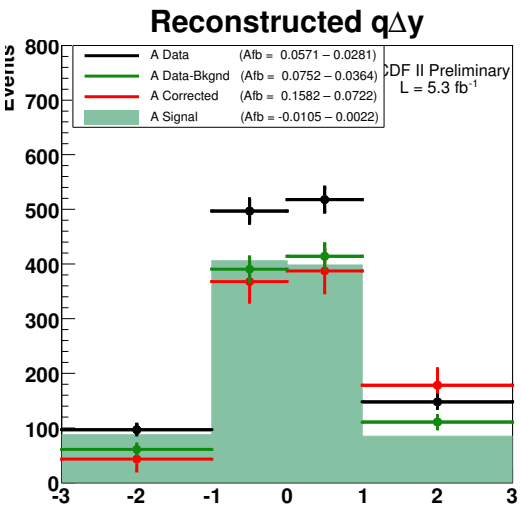

Figure 6.9. Four-bin reresentation of $q\Delta y_{lh} = y_t^{t\bar{t}}$ with background subtraction and unfold.

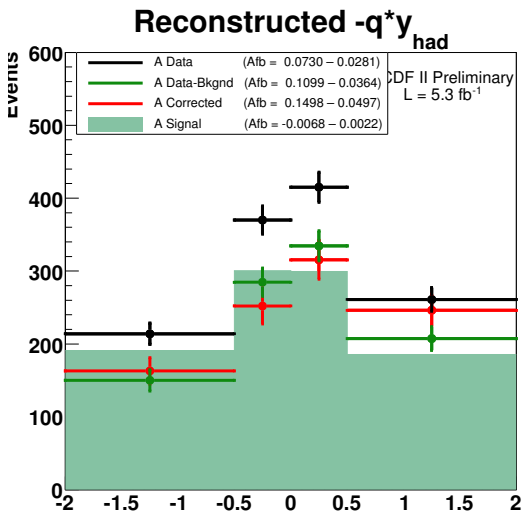

Figure 6.10. Four-bin reresentation of $-qy_h = ytlab$ with background subtraction and unfold.

	$q\Delta y_{lh}$	qY_{had}
data	0.057 ± 0.028	0.073 ± 0.028
data-bkgd	0.075 ± 0.036	0.110 ± 0.036
corrected	0.158 ± 0.072	0.150 ± 0.050
mcfm	0.058 ± 0.009	0.038 ± 0.038

Table 6.2. Summary of inclusive asymmetries.

6.3 Correction to the Parton-Level

6.3.1 Overview

To compare the measurements in Section 6.2 to the theoretical predictions, we need to correct the data to account for backgrounds, incomplete detector acceptance, and finite rapidity resolution of the reconstruction. The correction of these effects is two-fold. First, to extract the $t\bar{t}$ signal, we subtract off the expected background contribution from the reconstructed data. We then correct for acceptance and resolution effects using a linear matrix inversion.

The nature of the problem is shown nicely in generator level Z' study in CDF9813 [28]. Fig. 6.11 shows the generated vs. reconstructed distributions for the top quark lab rapidity $y_t^{p\bar{p}}$ and the total $M_{t\bar{t}}$ for low and high mass, narrow, sequential Z' decays to $t\bar{t}$. For all but the bottom-right plot, solid=generator and dashed=reconstructed; the bottom right plot has this convention reversed (bug). In the top row, we see how the reconstructed rapidity is smeared back towards greater symmetry. In the bottom row we see how the mass distributions are smeared to lower values. If the data contained such a Z', the asymmetry at high mass would be propagated down into the low mass region in the reconstructed data. The correction would re-concentrate the asymmetry back to high mass.

We represent the bins of the parton-level Δy distribution by a vector, $\vec{n}_{\text{parton}}$. The distribution is first modified by the acceptance and then by the smearing. These transformations can be expressed as matrices acting on the distribution vector.

$$\vec{n}_{\text{signal}} = \mathbf{S}\mathbf{A}\vec{n}_{\text{parton}} \tag{6.21}$$

To measure the parton-level data, Equation 6.21 is inverted:

$$\vec{n}_{\text{parton}} = \mathbf{A}^{-1}\mathbf{S}^{-1}\vec{n}_{\text{signal}} \tag{6.22}$$

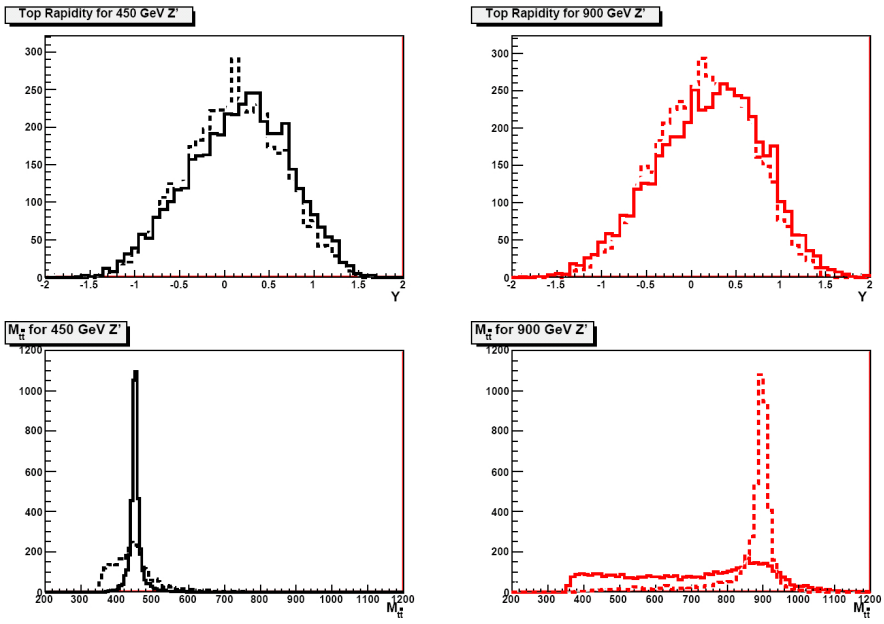

Figure 6.11. Generated vs. reconstructed $y_t^{p\bar{p}}$ and $M_{t\bar{t}}$ for low mass and high mass sequential $Z\prime$. For all but the bottom right, solid = generated, dashed = reconstructed. Bottom right is reversed.

The matrices **A** and **S** are derived from Monte Carlo samples by comparing truth distributions to the same distributions after reconstruction.

In the final application, we must account for the presence of backgrounds, so the signal is extracted from the data by subtracting the background events from the reconstructed sample.

$$\vec{n}_{\text{signal}} = \vec{n}_{\text{reconstruction}} - \vec{n}_{\text{background}} \tag{6.23}$$

By substituting Equation 6.23 into Equation 6.22, we can express the parton-level distribution, $\vec{n}_{\text{parton}}$, in terms of known values:

$$\vec{n}_{\text{parton}} = \mathbf{A}^{-1}\mathbf{S}^{-1}(\vec{n}_{\text{reconstruction}} - \vec{n}_{\text{background}}) \tag{6.24}$$

Previous studies of this method found that using four components to the vectors minimized the errors [17]. In the inclusive analysis, the vectors in Equation 6.24 have

four components comprising two forward bins and two backward bins in rapidity:

$$\vec{n} = \begin{pmatrix} N_F(\Delta y_{lh} > 1) \\ N_F(\Delta y_{lh} \leq 1) \\ N_B(\Delta y_{lh} \geq -1) \\ N_B(\Delta y_{lh} < -1) \end{pmatrix} \tag{6.25}$$

The acceptance and smearing corrections are 4x4 matrices relating parton-level and signal-level values. To allow for easier interpretation, the acceptance matrix is renormalized to the number of signal events in the data sample, which means that the entries in the matrix are close to unity.

We employ a simplified binning of the rapidity [9]. Fig. 6.10 shows the Δy and y_t distributions in the 4-bin representation used in Refs. [10, 8]. The black marker shows the data and the green marker is the data after background subtraction. The green histogram is the Pythia $t\bar{t}$ model. The background subtracted data is near the background-free prediction, but continues to show the asymmetries.

The red marker shows the rapidity distributions after correcting for acceptance and bin migration that arise in the selection and reconstruction. The correction procedure is a linear unfold in the four rapidity bins based on acceptance and smearing effects as measured with the Pythia ttop25 simulation. The binning is optimized to minimize the uncertainty in the correction, with the intermediate bin-edge put at $|\Delta y| = 1.0$ or $|y_t^{p\bar{p}}| = 0.5$. The corrected inclusive asymmetries, whch represent the physics at the parton level after gluon radiation, are $A^{t\bar{t}} = 0.16 \pm 0.076$ and $A^{p\bar{p}} = 0.15 \pm 0.055$. The asymmetries in the raw data, in the backgrounds (a la M24U), in the background subtracted data, and fully corrected to the parton level are summarized in Table 6.2, along with the expected NLO QCD asymmetry predicted by MCFM.

CHAPTER 7

Asymmetry and Kinematics

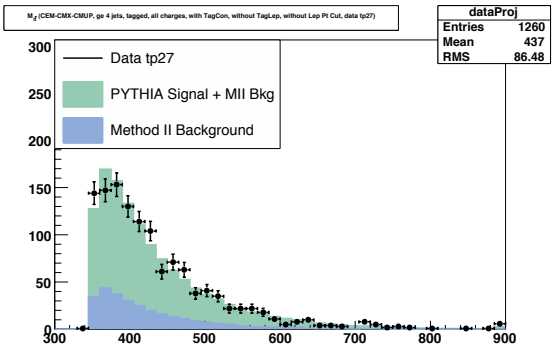

Figure 7.1. The total invariant mass of $M_{t\bar{t}}$.

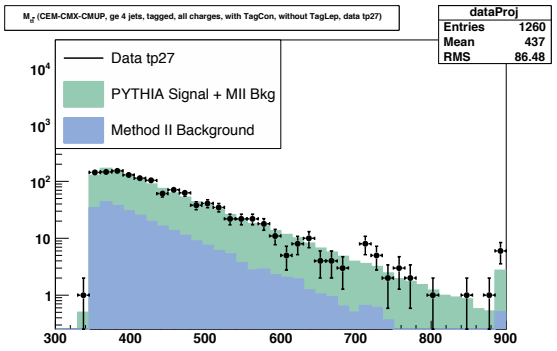

Figure 7.2. The total invariant mass of $M_{t\bar{t}}$ (log scale).

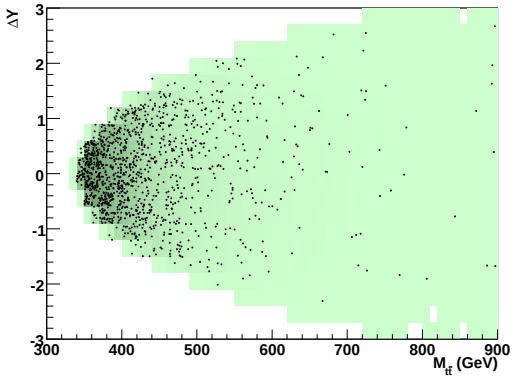

Figure 7.3. The $q\Delta y_{lh}$—$M_{t\bar{t}}$ plane.

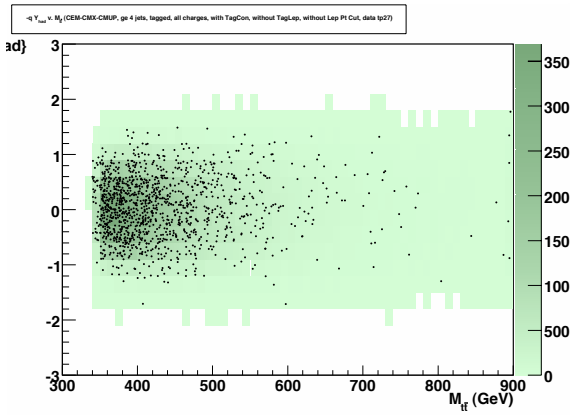

Figure 7.4. The $-qY_{had}$—$M_{t\bar{t}}$ plane.

The NLO QCD asymmetry has a strong $M_{t\bar{t}}$ dependence, as shown in Fig. 1.2. The $M_{t\bar{t}}$ dependence allows us to probe the fundamental mechanism of the asymmetry.

The value of $M_{t\bar{t}}$ is derived using the same reconstruction process described in Sec. 5 to measure the rapidities of the top quarks. The distribution of $M_{t\bar{t}}$ is shown

in linear and log scales in Fig. 7.1. A recent search for structure in this spectrum using 1.9fb^{-1} found no bumps or wiggles, although there is a hint of an excess on the tail in Ref. [29]. A measurement of the differential cross section in 2.7fb^{-1} finds consistency with Ref. [30].[1] DØ claims to see an modest excess on the tail [31].

Our studies are performed in the space of rapidity or rapidity difference vs $M_{t\bar{t}}$. The top plot in Fig. 7.3 shows the 2-dimensional distribution of Δy vs $M_{t\bar{t}}$; the bottom plot shows y_t vs $M_{t\bar{t}}$. Each dot is one event. The green shading is the relative probability of events from the combined ttop25+M24U background+signal model. We expect $M_{t\bar{t}}$ and Δy to be related by a simple kinematic relationship mediated by the transverse mass of the system: $M_{t\bar{t}} = 2m_T \cosh \Delta y$. As seen in the top plot of Fig. 7.3, both the data and the prediction confirm this expectation. The extremum of the rapidity difference grows from less than 0.5 at low masses to greater than 2.0 at high mass. The bottom plot shows that rapidity of the hadronic top quark is limited to less than 1.5 and mostly confined to less than 1.0 in a rather flat way across the whole mass domain.

The comparison of these plots suggests that interesting information on the rapidity vs. mass correlation exists in the $t\bar{t}$ frame, but is diluted in the uncontrolled boost to the $p\bar{p}$ frame. We have already noted that the MCFM prediction for the asymmetry (and thus the significance) is larger in the Δy variable, that Δy is less diluted in the raw data, and that the asymmetry in Δy is equal to the top production angle asymmetry in the $t\bar{t}$ frame. For all of these reasons, we will focus on the Δy_{lh} variables in much of what follows. y_t is still an important cross-check.

We now examine the mass dependence of the asymmetries in the data, and follow that a detailed cross-check of the results against variations in selection and reconstruction.

[1]The cited analysis uses a matrix inversion procedure similar to the one used in Sec. 6.

7.1 A vs. $M_{t\bar{t}}$

A raw differential asymmetry $dA^{t\bar{t}}/dM_{t\bar{t}}$ is found by binning $M_{t\bar{t}}$ in the top plot of Fig. 7.3 and calculating the asymmetry in each bin. The mass-dependent asymmetry $A^{t\bar{t}}(M^i_{t\bar{t}})$ is determined by dividing the $M_{t\bar{t}}$ axis into i bins and calculating the asymmetry in each bin:

$$A^{t}\bar{t}(M^i_{t\bar{t}}) = \frac{N(\Delta y_{lh} > 0, M^i_{t\bar{t}}) - N(\Delta y_{lh} < 0, M^i_{t\bar{t}})}{N(\Delta y_{lh} > 0, M^i_{t\bar{t}}) + N(\Delta y_{lh} < 0, M^i_{t\bar{t}})} \tag{7.1}$$

We use 50 GeV/c^2 slices of $M_{t\bar{t}}$ below 600 GeV/c^2, and 100 GeV/c^2 slices above. Fig. 7.5 shows the asymmetry in Δy for the separate charge species as a function of $M_{t\bar{t}}$. The asymmetries for the two charges behave in approximately equal and opposite fashion. Fig. 7.5b. shows the combined asymmetry $A^{t\bar{t}}$ in the same mass bins. The asymmetry is consistent with the expected monotonic positive correlation with $M_{t\bar{t}}$, though the large statistical errors at high mass allow for many possible models. The differential asymmetries are summarized in Table 7.1.

bin-center	N	A^{tt}	MCFM	A^{+}_{lh}	A^{-}_{lh}
350	499	-0.026 ± 0.045	0.030 ± 0	+0.004 ± 0.066	+0.052 ± 0.061
400	322	-0.012 ± 0.056	0.050 ± 0	-0.026 ± 0.081	+0.000 ± 0.077
450	190	0.157 ± 0.072	0.070 ± 0	+0.203 ± 0.096	-0.103 ± 0.106
500	95	0.304 ± 0.097	0.090 ± 0	+0.274 ± 0.140	-0.330 ± 0.136
550	58	0.137 ± 0.130	0.090 ± 0	+0.131 ± 0.180	-0.140 ± 0.185
600	34	0.098 ± 0.220	0.110 ± 0	+0.462 ± 0.201	-0.452 ± 0.227
700	20	0.105 ± 0.323	0.140 ± 0	-0.320 ± 0.268	-0.706 ± 0.243

Table 7.1. The differential asymmetry in Δy, in MCFM, and in Δy_{lh} for both lepton charges, as a function of $M_{t\bar{t}}$.

7.1.1 A vs. $M_{t\bar{t}}$ Sensitivity

A proper treatment of this information would make a mass and rapidity dependent correction to derive the functional dependence of $A(M_{t\bar{t}})$ that can compared to theory. A simple technique for doing this has been developed by M. Tecchio and T. Schwarz, and used to measure $A^{p\bar{p}}$ as a function of $M_{t\bar{t}}$ in 1.9fb^{-1}, see CDF9813 [28]. In

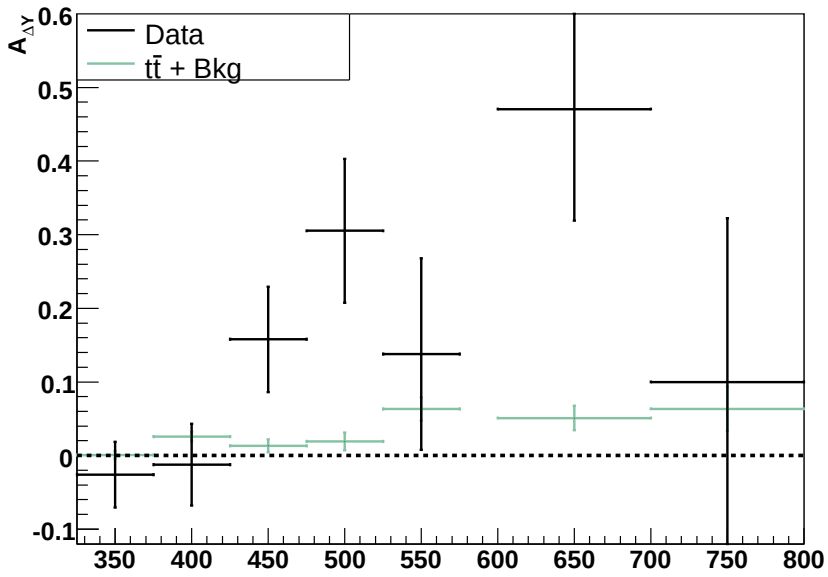

Figure 7.5. The charge weighted $A(q\Delta y_{lh})$ for all events vs $M_{t\bar{t}}$ in bins of 50 GeV/c^2.

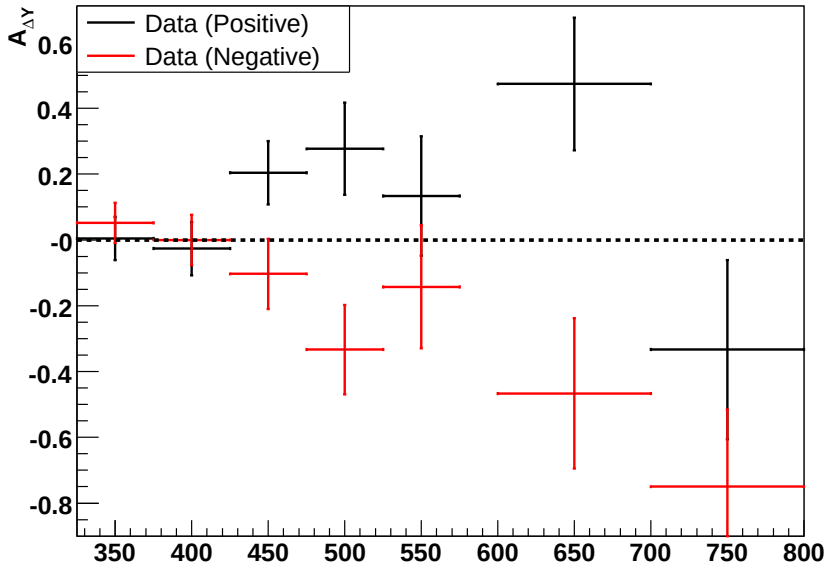

Figure 7.6. A vs. $M_{t\bar{t}}$ in bins of 50 GeV/$c^2$for the two charges, positive (red) and negative (black).

order to maximize statistics and mitigate the complication of the unfold corrections, they use two bins in rapidity and mass, and reuse the 4-bin unfold machinery that is understood and approved in the inclusive analysis. The effect of the bin choice is studied by looking at the results as the bin edge is scanned across the mass range. We will ultimately apply this full procedure to find the parton-level mass dependent $A^{t\bar{t}}$ in the 5.3fb^{-1} sample. In preparation for this, we first study the dependence of the asymmetry on $M_{t\bar{t}}$ in the raw data, employing the still useful technique of dividing the data into low and high mass regions above and below a threshold.

The sensitivity of the asymmetry is not only dependent on the rapidity variable of the asymmetry but also on the magnitude of the asymmetry and the number of events, both of which depend on the invariant mass. MCFM predicts that asymmetry increases with$M_{t\bar{t}}$, potentially increasing the sensitivity, but at the same time the number of events decreases, lowering the sensitivity. To see if there is a critical point, we can express the sensitivity in terms of the asymmetry and its error as given in Equation 7.2.

$$S = \frac{A}{\sigma_A} = \frac{A}{\sqrt{1-A^2}}\sqrt{N} \tag{7.2}$$

To maximize sensitivity, we set the derivative with respect to $M_{t\bar{t}}$ equal to zero.

$$\frac{dS}{dM_{t\bar{t}}} = \frac{1}{\sigma_A(1-A^2)}\frac{dA}{dM_{t\bar{t}}} + \frac{A}{2\sigma_A N}\frac{dN}{dM_{t\bar{t}}} \tag{7.3}$$

After setting Equation 7.3 equal to zero, the resulting equation can be re-arranged to give Equation 7.4.

$$\frac{dN}{dM_{t\bar{t}}} = -\frac{2}{A(1-A^2)}\frac{dA}{dM_{t\bar{t}}}N \tag{7.4}$$

We note that in Equation 7.4 N, A, and $\frac{dA}{dM_{t\bar{t}}}$ are all positive, meaning that sensitivity is maximal at a value of $M_{t\bar{t}}$ where $\frac{dN}{dM_{t\bar{t}}} < 0$, implying that the number of events

is decreasing. The number of events, $N(M_{t\bar{t}})$, is given by a relativistic Breit-Wigner distribution which decreases after a peak. In the case of the data, the peak is near $M_{t\bar{t}}$=400 GeV/c^2. After inserting a relativistic Breit-Wigner distribution with width Γ and peak at M_0 into Equation 7.4 and rearranging, we get Equation 7.5.

$$\frac{M_{t\bar{t}}(M_{t\bar{t}}^2 - M_0^2)}{(M_{t\bar{t}}^2 - M_0^2)^2 + \Gamma^2} = \frac{1}{2A(1-A^2)}\frac{dA}{dM_{t\bar{t}}} \tag{7.5}$$

The right side of Equation 7.5 is very small. Our invariant mass range is restricted to the range [345 GeV/c^2,∞), so the only way Equation 7.5 can be small is by having $M_{t\bar{t}}$ close to the peak, M_0. So the optimal sensitivity is for $M_{t\bar{t}}$ close to 400 GeV/c^2. While the exact location of the optimal invariant mass depends on the parametrization of the distributions and the asymmetry, the fact that the location is above the peak of the mass distribution only depends on the asymmetry being positive and having a positive mass-dependence. This argument is confirmed by examining the sensitivity of the asymmetry in the MC@NLO sample which finds the optimal threshold for sensitivity at 450 GeV/c^2.

Fig. 7.7 and Fig. 7.8 show the rapidity difference Δy at high and low mass when we divide the data into 2-bins below and above $M_{t\bar{t}} = 450$ GeV/c^2. Notice that the distribution is much broader at high mass, as expected from Fig. 7.3. At high mass there is a large and significant asymmetry $A = 0.210 \pm 0.049$, while at low mass the asymmetry is consistent with zero. The lab frame asymmetry at low mass is comparable to the inclusive result, increasing to $A^{p\bar{p}} = 0.100 \pm 0.052$ at high mass.

To understand the effect of the cut choice and capture all of the information, we look at the low-bin/high-bin behavior for both asymmetries as we move the mass threshold. The left plot in Fig. 8.6 shows the behavior of $A_{lh}^{\pm}$ in the high mass bin as a function of the bin edge; the separate charges are seen to behave in equal and opposite fashion. The combined $A^{t\bar{t}}$ is shown on the right. At the lowest threshold $M_{t\bar{t}} = 345$ GeV/c^2, all of the sample is in the upper bin and the asymmetry is the

inclusive result 0.070 ± 0.028. The $A^{t\bar{t}}$ grows with $M_{t\bar{t}}$ to $\sim 30\%$ at $M_{t\bar{t}} \geq 600$ GeV/c^2, followed by a drop off at very high mass that may not be statistitically meaningful. The right plot in Fig. 8.6 shows the behavior of $A_{lh}^{\pm}$ and $A^{t\bar{t}}$ in the low mass bin as a function of the bin edge. The asymmetry at low mass is small, growing slowly as the low bin absorbs more and more events at high mass, and asymptotes to the value of the inclusive measurement. The asymmetries for the separate charges are again equal and opposite.

The asymmetry values for the semi-integral samples at high and low $M_{t\bar{t}}$ are shown as a function of the bin edge in Table 7.2. In the high mass bin we find a steady increase of the asymmetry with mass. For all values of the bin edge cut, $A^{t\bar{t}}$ is larger than $A^{p\bar{p}}$, but with very similar uncertainties. At high mass, the asymmetries in $A^{t\bar{t}}$ are $3-4\sigma$ above zero. In the low mass bin, we find that $A^{p\bar{p}}$ is approximately constant at the inclusive value of $\sim 7\%$, independent of the bin-edge, whereas the behavior of $A^{t\bar{t}}$ is to grow zero up to the inclusive value.

	low mass		high mass	
bin-edge	$A^{p\bar{p}}$	A^{tt}	$A^{p\bar{p}}$	A^{tt}
400	0.079 ± 0.043	-0.019 ± 0.043	0.069 ± 0.037	0.113 ± 0.037
450	0.059 ± 0.034	-0.016 ± 0.034	0.103 ± 0.049	0.212 ± 0.048
500	0.056 ± 0.031	0.015 ± 0.031	0.157 ± 0.067	0.259 ± 0.066
550	0.064 ± 0.030	0.039 ± 0.030	0.156 ± 0.090	0.222 ± 0.088
600	0.066 ± 0.029	0.044 ± 0.029	0.205 ± 0.123	0.299 ± 0.120

Table 7.2. The two asymmetry variables compared at low and high $M_{t\bar{t}}$ as the low-high threshold is scanned.

7.2 Raw Data Summary

We measure an inclusive asymmetry in the tagged $t\bar{t}$ sample as shown in Table 7.3. As predicted by MC@NLO, we observe both a mass-dependence and a rapidity-dependence in the asymmetry, however, the observed asymmetries are larger than the asymmetries predicted by MC@NLO.

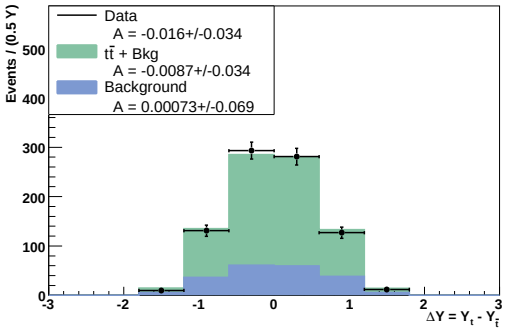

Figure 7.7. The distribution of $q\Delta y_{lh}$ at low mass.

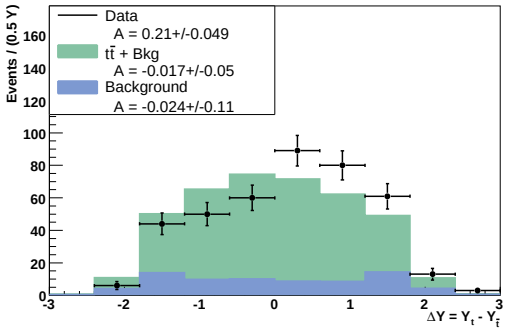

Figure 7.8. The distribution of $q\Delta y_{lh}$ at high mass.

		A in $t\bar{t}$ rest frame		
	N	inclusive	$M_{t\bar{t}} < 450$ GeV/c^2	$M_{t\bar{t}} \geq 450$ GeV/c^2
inclusive tagged	1260	0.057±0.028	-0.016±0.034	0.21±0.049
bkg.-subtracted	977	0.075±0.032	-0.022±0.039	0.265±0.053
pos. leptons	613	0.067±0.040	-0.013±0.050	0.210±0.066
neg. leptons	647	-0.048±0.039	0.020±0.047	-0.210±0.071
MCFM		0.058 ± 0.009	0.055 ± 0.009	0.088 ± 0.013

Table 7.3. The rest frame asymmetry $A^{t\bar{t}}$ in all data, $M_{t\bar{t}} < 450$ GeV/c^2, and $M_{t\bar{t}} \geq 450$ GeV/$c^2$for various selections.

The asymmetries found are robust under various cross-checks including different triggers, charge-separation, tighter selection cuts, and b-tagging – though the results of the single/double tags and different periods neither support nor deny an asymmetry. To explore the asymmetries and their mass-dependence, we will continue this analysis using the unfold technique used in previous studies.

7.3 Mass- and Rapidity-Dependent Corrections

We wish to find the asymmetry as a function of $M_{t\bar{t}}$. As we anticipated in Section 7.1, we maximize statistical precision, mitigate unfold complications, and re-use the well-vetted four-bin unfold machinery by organizing the data into two bins in rapidity, forward and backward, and two bins in mass, high and low. As in Section 7.1, the high-low boundary of $M_{t\bar{t}}$ is adjustable, and we will examine our results as the

boundary is varied. Our four-element data vector is:

$$\vec{n} = \begin{pmatrix} N_F(M_{t\bar{t}} \text{ low}) \\ N_B(M_{t\bar{t}} \text{ low}) \\ N_F(M_{t\bar{t}} \text{ high}) \\ N_B(M_{t\bar{t}} \text{ high}) \end{pmatrix} = \begin{pmatrix} FL \\ BL \\ FH \\ BH \end{pmatrix} \tag{7.6}$$

The acceptance matrix takes the form of a diagonal matrix:

$$\mathbf{A} = \begin{pmatrix} FL_{\text{true}}\, v\, FL_{\text{rec}} & 0 & 0 & 0 \\ 0 & BL_{\text{true}}\, v\, BL_{\text{rec}} & 0 & 0 \\ 0 & 0 & FH_{\text{true}}\, v\, FH_{\text{rec}} & 0 \\ 0 & 0 & 0 & BH_{\text{true}}\, v\, BH_{\text{rec}} \end{pmatrix} \tag{7.7}$$

where the diagonal values of $\mathbf{A}$ should be perturbations around unity. And the smearing matrix takes the form:

$$\mathbf{S} = \begin{pmatrix} FL_{\text{true}}\, v\, FL_{\text{rec}} & BL_{\text{true}}\, v\, FL_{\text{rec}} & FH_{\text{true}}\, v\, FL_{\text{rec}} & BH_{\text{true}}\, v\, FL_{\text{rec}} \\ FL_{\text{true}}\, v\, BL_{\text{rec}} & BL_{\text{true}}\, v\, BL_{\text{rec}} & FH_{\text{true}}\, v\, BL_{\text{rec}} & BH_{\text{true}}\, v\, BL_{\text{rec}} \\ FL_{\text{true}}\, v\, FH_{\text{rec}} & BL_{\text{true}}\, v\, FH_{\text{rec}} & FH_{\text{true}}\, v\, FH_{\text{rec}} & BH_{\text{true}}\, v\, FH_{\text{rec}} \\ FL_{\text{true}}\, v\, BH_{\text{rec}} & BL_{\text{true}}\, v\, BH_{\text{rec}} & FH_{\text{true}}\, v\, BH_{\text{rec}} & BH_{\text{true}}\, v\, BH_{\text{rec}} \end{pmatrix} \tag{7.8}$$

The columns of $\mathbf{S}$ sum to unity, as the rows represent all the possible locations of a given event after smearing. The sums rows of $\mathbf{S}$ show the relative proportions of the final locations of the events after smearing.

At the $M_{t\bar{t}} = 450$ GeV/c^2 threshold using ttop25 as the Monte Carlo generator, the values for $\mathbf{A}$ and $\mathbf{S}$ are:

$$\mathbf{A} = \begin{pmatrix} 0.932 \pm 0.004 & 0 \pm 0 & 0 \pm 0 & 0 \pm 0 \\ 0 \pm 0 & 1.00 \pm 0.004 & 0 \pm 0 & 0 \pm 0 \\ 0 \pm 0 & 0 \pm 0 & 1.00 \pm 0.005 & 0 \pm 0 \\ 0 \pm 0 & 0 \pm 0 & 0 \pm 0 & 1.100 \pm 0.005 \end{pmatrix} \tag{7.9}$$

$$\mathbf{S} = \begin{pmatrix} 0.631 \pm 0.003 & 0.258 \pm 0.002 & 0.216 \pm 0.002 & 0.139 \pm 0.002 \\ 0.254 \pm 0.002 & 0.620 \pm 0.003 & 0.132 \pm 0.002 & 0.237 \pm 0.002 \\ 0.088 \pm 0.001 & 0.032 \pm 0.001 & 0.578 \pm 0.004 & 0.072 \pm 0.001 \\ 0.028 \pm 0.001 & 0.091 \pm 0.001 & 0.074 \pm 0.001 & 0.552 \pm 0.003 \end{pmatrix} \tag{7.10}$$

As expected, the entries of **A** are all close to unity representing the relative fraction of each sample. Overall there is a slight efficiency bias for high mass events over low mass events due to the presence of more energetic jets and leptons. There is an additional bias for backward events over forward events due to angular ordering of the QCD radiation as discussed in Section 8.6.

The entries of **S** can be understood by looking at the third column as an example. Of all the forward events with $M_{t\bar{t}} \geq 450$ GeV/c^2 at the parton level, 21.6% were reconstructed as forward events below the mass threshold, 13.2% were reconstructed as backward events below the mass threshold, 57.8% were reconstructed as forward events above the mass threshold, and 7.4% were reconstructed as backward events above the mass threshold. The sums of the rows of **S** show the relative proportions of the final locations for events after smearing. The matrix in Equation 7.10 reveals that both the forward low and the backward low bins end up with 1.24 times their original bin contents, while the forward high bin ends up with 0.77 its original contents and the backward high bin ends up with 0.75 its original contents. Overall, we see events in the high mass bins shift to the low mass bins but little in the opposite direction.

	$\vec{n}_{\text{parton}}$	$\mathbf{A}\vec{n}_{\text{parton}}$	$\mathbf{SA}\vec{n}_{\text{parton}}$
FL	1000	932	1215
BL	1000	1000	1249
FH	1000	1000	771
BH	1000	1100	798
$A^{t\bar{t}}$ below	0.000	-0.035	-0.014
$A^{t\bar{t}}$ above	0.000	-0.048	-0.017

Table 7.4. The effect of the ttop25 acceptance and smearing matrices on a toy sample of events with no parton-level asymmetry.

As seen in Table 7.4, both acceptance and smearing effects shift asymmetries down from the parton-level values. The exact ratios of final bin counts to initial bin counts depend on the relative proportions of the initial bin counts, but the toy sample shown allows us to explicitly see how the acceptance and smearing effects work. In Figure 7.9, the unfold correction is seen explicitly acting on the axigluon validation sample. At low mass, the raw bin counts (black) are higher than the corrected bin counts (red), while at high mass in the forward bin raw counts are much lower than corrected counts. It is easily seen that the corrected asymmetries are higher than the raw asymmetries — especially at high mass.

7.4 Data Unfold Results

We now turn the unfold technique to the data sample on hand. In Figure 7.10, the asymmetry values below the mass thresholds show an increase for thresholds above 500 GeV/c^2 while for other mass thresholds the errors are too large — due to smaller statistics — for unambiguous interpretation. At the 450 GeV/c^2 threshold, the asymmetry below shifts from a raw value of $A^{t\bar{t}} = 0.001 \pm 0.036$ to a corrected value of $A^{t\bar{t}} = -0.037 \pm 0.139$ which is consistent with the expected MCFM value of $A^{t\bar{t}} = 0.040 \pm 0.006$. In Figure 7.11, the asymmetry values above the mass thresholds show an increase for thresholds below 700 GeV/c^2 while for other mass thresholds the errors are too large — due to smaller statistics — for unambiguous interpretation. At the 450 GeV/c^2 threshold, the asymmetry above shifts from a raw value of $A^{t\bar{t}} =$

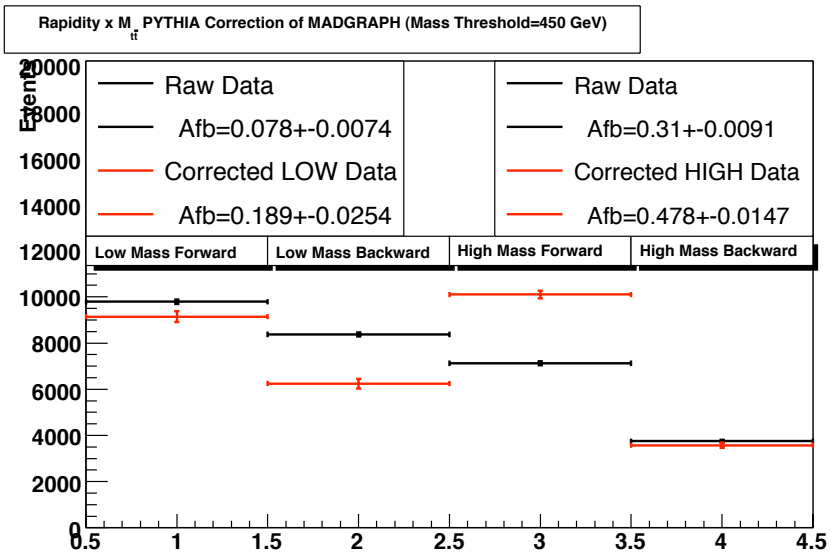

Figure 7.9. The unfold for $A^{t\bar{t}}$ in the axigluon sample using ttop25 at the $M_{t\bar{t}} = 450$ GeV/c^2mass threshold in each of the four bins: low mass forward, low mass backward, high mass forward, high mass backward. True values of the asymmetry are $A_{lh}^{\text{low}} = 0.150$ and $A_{lh}^{\text{high}} = 0.466$.

0.216 ± 0.052 to a corrected value of $A^{t\bar{t}} = 0.449 \pm 0.105$ deviates from the expected MCFM value of $A^{t\bar{t}} = 0.088 \pm 0.011$ by 3.4σ before systematic errors are computed. The corrected $A^{t\bar{t}}$ can be compared across all thresholds in Figure 9.12. The range of the MCFM values show the MC values with errors of 12%.

	A^{tt} $M_{t\bar{t}} < 450$ GeV/c^2	A^{tt} $M_{t\bar{t}} \geq 450$ GeV/c^2
raw tagged	0.001 ± 0.036	0.216 ± 0.052
background subtracted	0.001 ± 0.040	0.254 ± 0.055
corrected tagged	-0.037 ± 0.139	0.449 ± 0.105
inclusive MCFM	0.040 ± 0.006	0.088 ± 0.013

Table 7.5. The asymmetry $A^{t\bar{t}}$, both raw and corrected, in all data, $M_{t\bar{t}} < 450$ GeV/c^2, and $M_{t\bar{t}} \geq 450$ GeV/$c^2$for various selections.

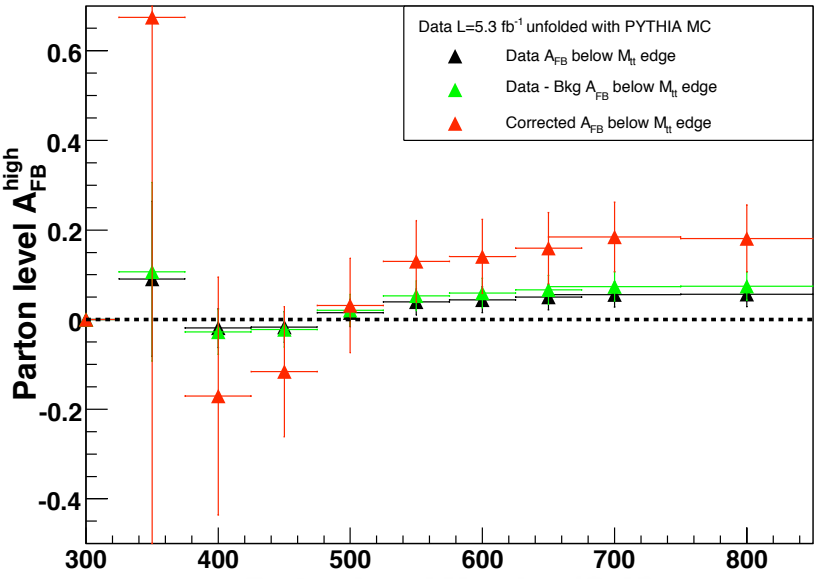

Figure 7.10. The corrected forward-backward asymmetry in $A^{t\bar{t}}$ below the 450 GeV/c^2in the $L = 5.3\text{fb}^{-1}$ data sample using ttop25 to generate the correction matrices.

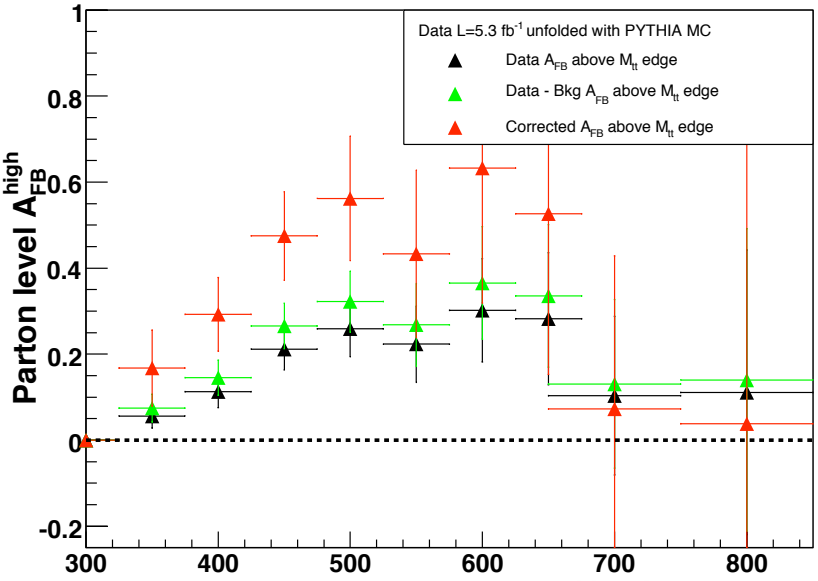

Figure 7.11. The corrected forward-backward asymmetry in $A^{t\bar{t}}$ above the 450 GeV/c^2in the $L = 5.3\text{fb}^{-1}$ data sample using ttop25 to generate the correction matrices.

	low mass		high mass	
edge	Raw A^{tt}	Corrected A^{tt}	Raw A^{tt}	Corrected A^{tt}
400	-0.006 ± 0.046	-0.089 ± 0.248	0.126 ± 0.039	0.299 ± 0.086
450	0.001 ± 0.036	-0.037 ± 0.139	0.216 ± 0.052	0.449 ± 0.105
500	0.053 ± 0.033	0.085 ± 0.104	0.247 ± 0.070	0.491 ± 0.143
550	0.054 ± 0.031	0.163 ± 0.090	0.215 ± 0.094	0.384 ± 0.199
600	0.057 ± 0.031	0.162 ± 0.082	0.321 ± 0.127	0.631 ± 0.315
650	0.062 ± 0.030	0.177 ± 0.078	0.314 ± 0.160	0.558 ± 0.376
700	0.069 ± 0.030	0.202 ± 0.076	0.120 ± 0.199	0.081 ± 0.386
800	0.070 ± 0.030	0.204 ± 0.074	0.000 ± 0.354	-0.242 ± 0.774

Table 7.6. The raw and corrected asymmetry values of $A^{t\bar{t}}$ in $t\bar{t}$ events in $L = 5.3\text{fb}^{-1}$ compared at low and high $M_{t\bar{t}}$ as the invariant mass threshold is scanned.

CHAPTER 8

Cross-Checks of the A vs. $M_{t\bar{t}}$ Dependence

Using the boundary of $M_{t\bar{t}} = 450$ GeV/c^2, we now survey the behavior of the two-bin mass dependence against variations in selection and reconstruction. This cut at divides the 1260 events of the sample into 854 events at low mass and 406 events at high mass. We reiterate here that a proper study of a real $t\bar{t}$ effect across these selections would employ a background subtraction to measure a pure $t\bar{t}$ signal. Because we wish to avoid any assumptions at this stage, we perform these cross-checks using the inclusive tagged lepton+jets data.

8.1 Frame

The comparison of $A^{p\bar{p}}$ and $A^{t\bar{t}}$ at high and low mass for all bin edges was presented in Table 7.2. The Δy and y_t distributions below and above our reference cut at $M_{t\bar{t}} = 450$ GeV/c^2 were shown in Figs. 7.7 and 7.8. Table 8.1 summarizes the asymmetries in Figs. 7.7 and 7.8, along with the expectation from MCFM and Madgraph, and the asymmetries when the cut is moved to 500 GeV/c^2. The MCFM results are at parton level, and we would expect the values here to be degraded by roughly a factor ~ 2 in the measurement. ay is consistent with MCFM in any interpretation. $A^{t\bar{t}}$ at high mass is 4σ above zero and 2σ above the parton-level MCFM prediction. Although MCFM predicts that $A^{t\bar{t}} \sim 2A^{p\bar{p}}$ in the inclusive sample, at high mass it predicts a ratio much closer to 1. The data disagrees with this, showing a ratio ~ 2 at high mass, although the uncertainty is large. The Madgraph result is for fully simulated

	$M_{t\bar{t}} < 450$ GeV/c^2		$M_{t\bar{t}} \geq 450$ GeV/c^2	
sample	$A^{p\bar{p}}$	A^{tt}	$A^{p\bar{p}}$	A^{tt}
data	0.059 ± 0.034	-0.016 ± 0.034	0.103 ± 0.049	0.212 ± 0.048
MCFM	0.020 ± 0.003	0.040 ±0.006	0.071 ± 0.001	0.087 ± 0.013
Madgraph	0.037 ± 0.007	0.060 ±0.006	0.220 ± 0.008	0.250 ± 0.008

Table 8.1. Asymmetries in two frames at hi and low mass for data, MCFM (parton level) and Madgraph coloron.

$t\bar{t}$ events combined with the standard M24U backgrounds, and can thus be compared directly to the data. At high mass the ratio $A^{t\bar{t}}/A^{p\bar{p}}$ in Madgraph is also close to 1, like MCFM, and in distinction to the data.

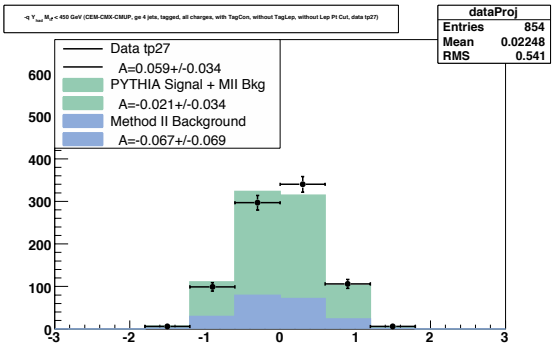

Figure 8.1. The distribution of qy_h at low mass.

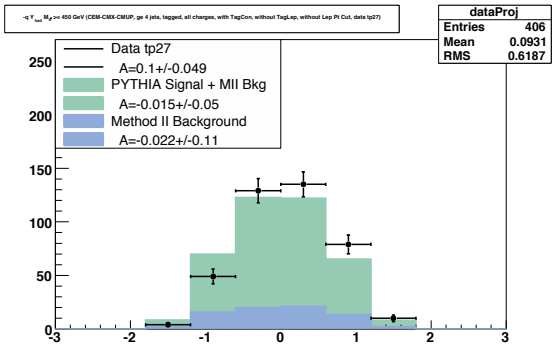

Figure 8.2. The distribution of qy_h at high mass.

8.2 Charge

The Δy_{lh} distributions in the high mass region for the two charge species is shown in Figs. 8.3 and 8.4.

	N events	inclusive	$M_{t\bar{t}} < 450$ GeV/c^2	$M_{t\bar{t}} \geq 450$ GeV/c^2
inclusive tagged	1260	0.057±0.028	-0.016±0.034	0.210±0.049
pos. leptons	613	0.067±0.040	-0.013±0.050	0.210±0.066
neg. leptons	647	-0.048±0.039	0.020±0.047	-0.210±0.071

Table 8.2. The asymmetry $A^{t\bar{t}}$ below and above $M_{t\bar{t}} = 450$ GeV/c^2.

Table 8.2 shows the Δy asymmetries at low and high mass when the sample is partitioned by the sign of the lepton. At low mass the asymmetries are both small.

At high mass the asymmetries are equal and opposite at roughly 20%. As seen in Figs. 8.3 and 8.4, the distributions are qualitatively mirror-symmetric. This is an amplified version of the "CP-conserving" effect discussed in Sec. 1.3.

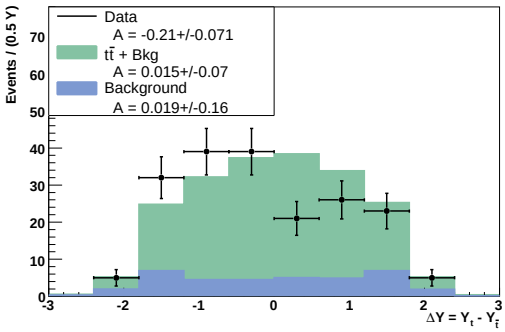

Figure 8.3. The distribution of Δy_{lh} at high mass for negative lepton charges.

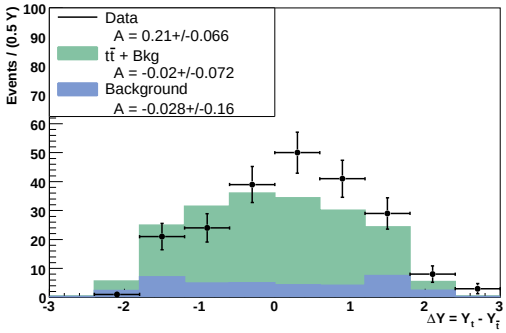

Figure 8.4. The distribution of Δy_{lh} at high mass for positive lepton charges.

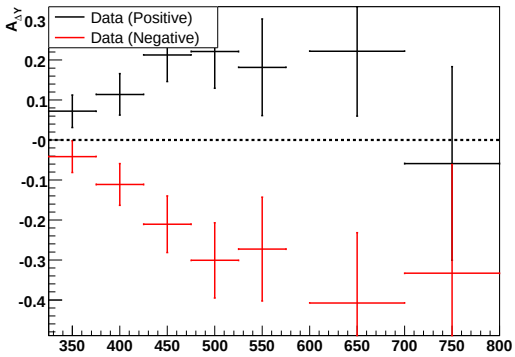

Figure 8.5. The integrated asymmetry above the $M_{t\bar{t}}$ threshold for separate charge species, positive/negative = red/black.

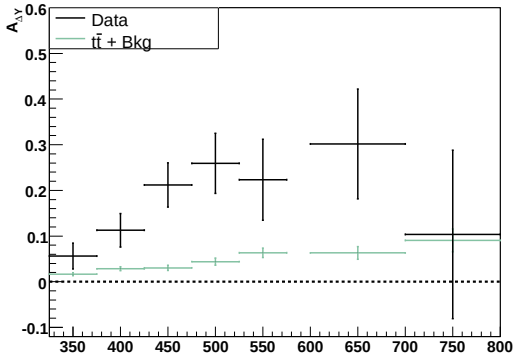

Figure 8.6. The integrated asymmetry above the $M_{t\bar{t}}$ threshold.

8.3 Reconstruction

The continued presence of the asymmetry in the charge-separated samples makes it unlikely that a reconstruction bias is the source of the asymmetry. However, it is still possible that a sub-sample of the events is reconstructed poorly and the asymmetry is unique to those events. To exclude events with low quality resolution, we cut on the χ^2 variable. Figs. 8.9 and 8.10 show the Δy distributions at low and high mass when

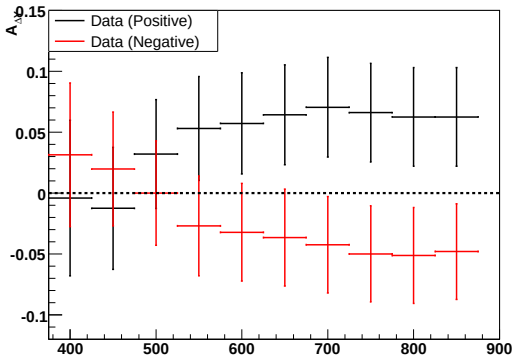

Figure 8.7. The integrated asymmetry below the $M_{t\bar{t}}$ threshold for separate charge species, positive/negative = red/black.

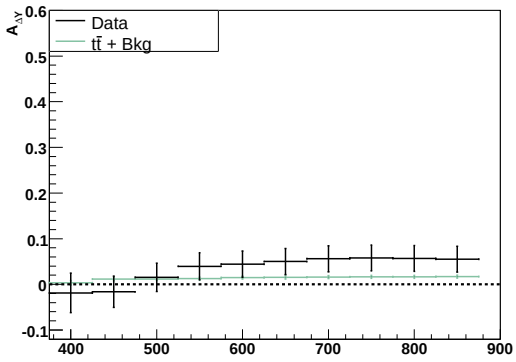

Figure 8.8. The integrated asymmetry below the $M_{t\bar{t}}$ threshold.

we make a reconstruction quality cut at $\chi^2 = 3.0$. In this sample of 388 events we find $A^{t\bar{t}} = -0.033 \pm 0.065$ at low mass and $A^{t\bar{t}} = 0.180 \pm 0.099$ at high mass. The Δy distributions at high and low mass are very similar to those in the full sample of 1260 events with no χ^2 cut seen Figs. 7.7 and 7.8, except that much of the background contribution has eliminated. Thus the high mass asymmetry appears in the best reconstructed events and seems less likely to be a background effect.

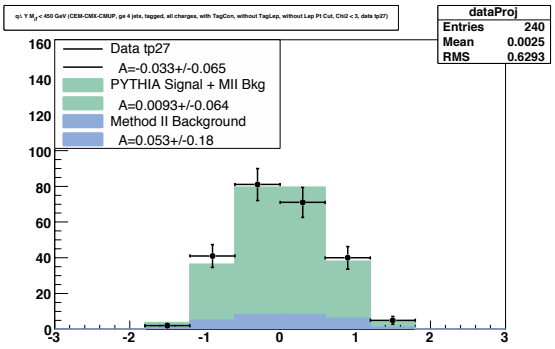

Figure 8.9. The distribution of Δy_{lh} at low mass in events with reconstruction $\chi^2 < 9.0$.

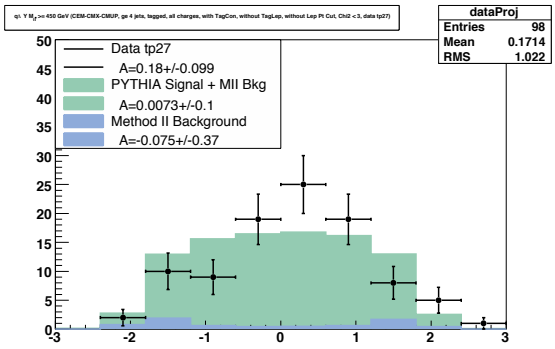

Figure 8.10. The distribution of Δy_{lh} at high mass in events with reconstruction $\chi^2 < 9.0$.

Another concern about the reconstruction is the handling of the b-tag information. Perhaps forcing the b-tagged jet to be a b-parton creates an asymmetry when that b-jet is assigned to the wrong top system? To test for b-tag effects, we re-run the reconstruction having removed the constraint that b-tagged jets should be assigned

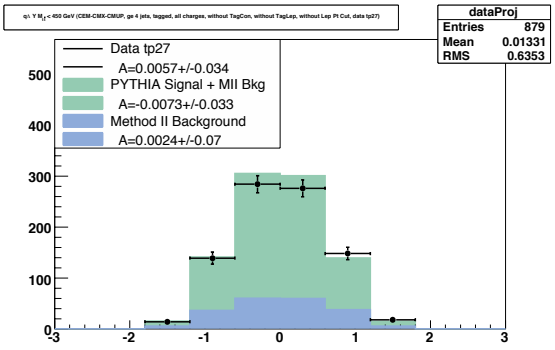

Figure 8.11. The distribution of Δy_{lh} at low mass with no requirement the reconstruction associate b-tags to b-jets.

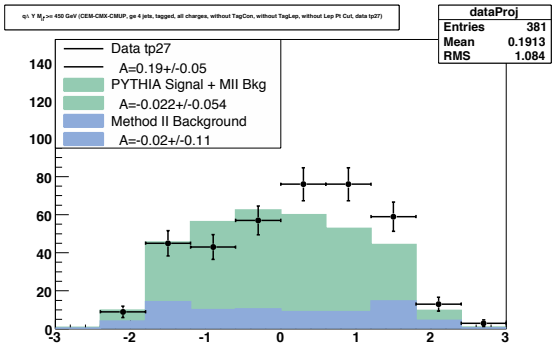

Figure 8.12. The distribution of Δy_{lh} at high mass with no requirement the reconstruction associate b-tags to b-jets.

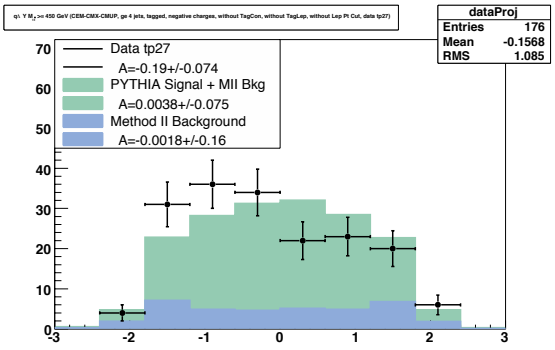

Figure 8.13. The distribution of Δy_{lh} at high mass with negative leptons when the reconstruction is not required to associate b-tags to b-jets.

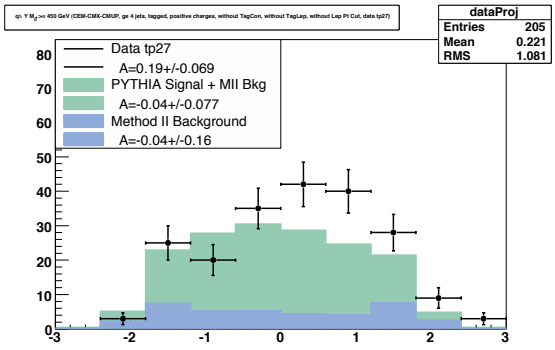

Figure 8.14. The distribution of Δy_{lh} at high mass with positive leptons when the reconstruction is not required to associate b-tags to b-jets.

to b-partons. The Δy distributions at low and high mass in this case are shown in Figs. 8.11 and 8.12. Note that we still use the b-tagging to purify the $t\bar{t}$ signal. We find $A^{t\bar{t}} = 0.0057 \pm 0.034$ at low mass and $A^{t\bar{t}} = 0.190 \pm 0.050$ at high mass, very close to the result when the b-tag constraint is used. When we further separate the events by lepton charge, the Δy distributions for the no fit with no b-tag constraint are shown in Figs. 8.13 and 8.14. The Δy_{lh} asymmetries are $A^{-}_{lh} = -0.190 \pm 0.074$ and $A^{+}_{lh} = 0.190 \pm 0.069$.

These results suggest that the mass dependent asymmetry, and its reflection under lepton charge reversal, is not obviously associated with reconstruction or b-tagging.

8.4 Run Range.

In the inclusive case we found that the asymmetry significance was somewhat lower than expected in the more recent part of the data. Since the asymmetry is predominantly at high mass, we expect the significance there will also be reduced in the later data. The cumulative significance of the $q\Delta y_{lh}$ asymmetry at high mass is shown in table and plot form in Fig. 8.15. The later data is indeed a bit flat. On the other hand maybe the early data was a bit steep. The curve is constrained to go through zero, is a very good fit to the $\sqrt{N}$ hypothesis and its normalization gives $A_{hiM} = 0.278 \pm 0.010$, consistent with the simple average. We will continue to monitor the integrity of that overall dataset, but for the purpose of our study we will also continue to consider the whole data set as a single robust sample.

	N events	all $M_{t\bar{t}}$	$M_{t\bar{t}} < 450$ GeV/c^2	$M_{t\bar{t}} \geq 450$ GeV/c^2
CEM	735	0.026±0.037	-0.020±0.045	0.120±0.063
CMUP	332	0.130±0.054	0.047±0.065	0.310±0.095
CMX	172	0.035±0.076	-0.143±0.091	0.430±0.120

Table 8.3. The inclusive and mass dependent asymmetries in qY for various trigger selections

Data Source	n Events	A Above 450	Significance
tp8	98	0.327 ± 0.096	3.42
tp9	110	0.291 ± 0.082	3.19
tp10	134	0.300 ± 0.082	3.62
tp11	151	0.311 ± 0.077	4.02
tp12	158	0.304 ± 0.076	4.01
tp13	180	0.333 ± 0.070	4.74
tp14	182	0.341 ± 0.070	4.89
tp15	191	0.309 ± 0.069	4.49
tp16	196	0.316 ± 0.068	4.67
tp17	205	0.307 ± 0.066	4.62
tp18	229	0.301 ± 0.063	4.78
tp19	248	0.282 ± 0.061	4.63
tp20	267	0.281 ± 0.059	4.78
tp21	294	0.252 ± 0.056	4.46
tp22	313	0.246 ± 0.055	4.49
tp23	325	0.225 ± 0.054	4.16
tp24	345	0.223 ± 0.052	4.25
tp25	357	0.216 ± 0.052	4.17

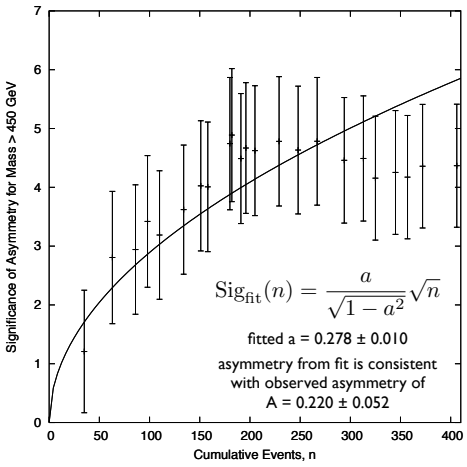

Figure 8.15. Significance of $A(q\Delta y_{lh})$ as a function of the total number of b-tagged events. Each point represents the increment of a new data period.

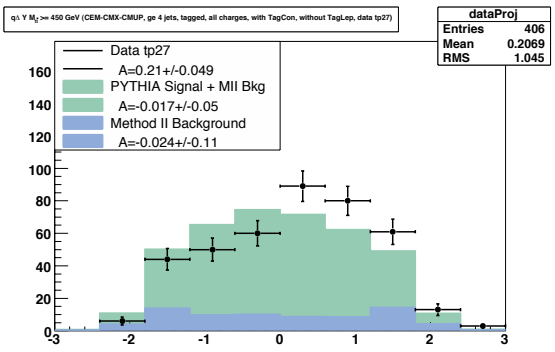

Figure 8.16. The distribution of Δy_{lh} at high mass, all triggers

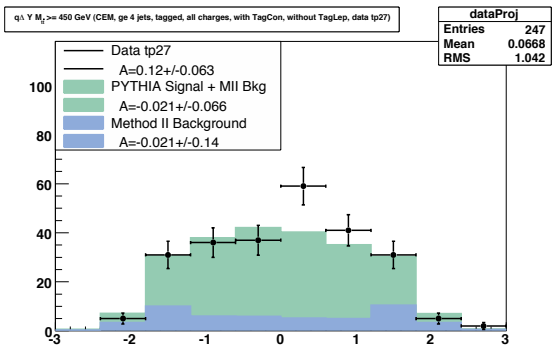

Figure 8.17. The distribution of Δy_{lh} at high mass for CEM-triggered events.

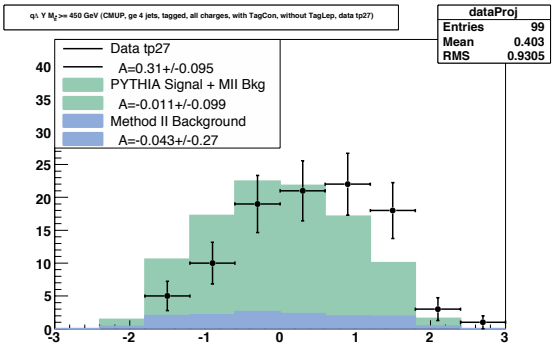

Figure 8.18. The distribution of Δy_{lh} at high mass for CMUP-triggered events.

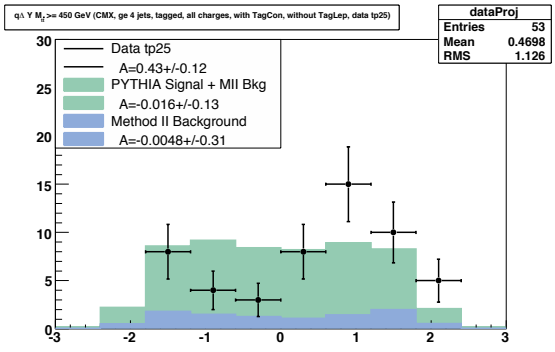

Figure 8.19. The distribution of Δy_{lh} at high mass for CMX-triggered events.

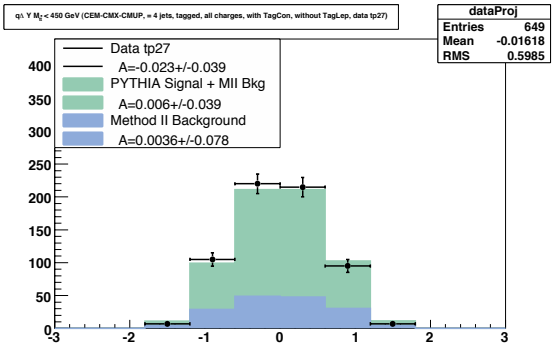

Figure 8.20. The distribution of Δy_{lh} at low mass for events with 4 tight jets.

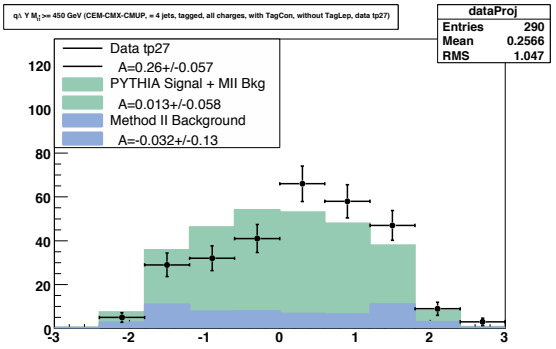

Figure 8.21. The distribution of Δy_{lh} at high mass for events with 4 tight jets.

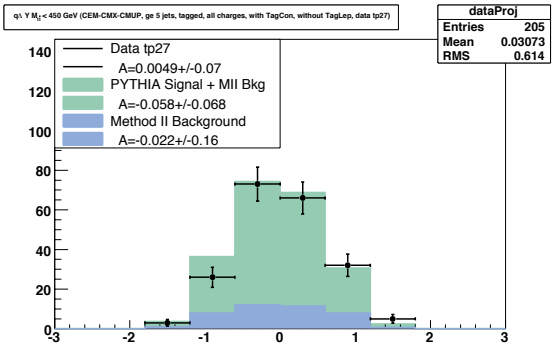

Figure 8.22. The distribution of Δy_{lh} at low mass for events with 5 (or more) tight jets.

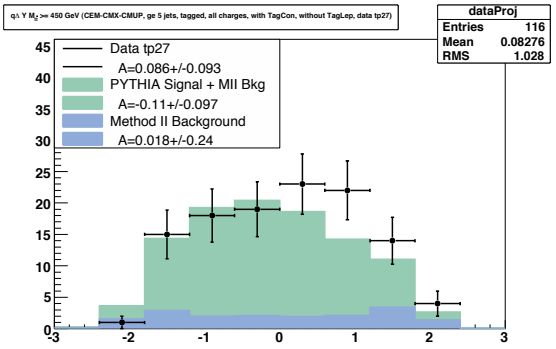

Figure 8.23. The distribution of Δy_{lh} at high mass for events with 5 (or more) tight jets.

8.5 Triggers

Figs. 8.17, 8.18, and 8.19 show the distribution of Δy at high-mass as measured separately for each one of our trigger lepton types. The asymmetries are listed in Table 8.3. As we saw in the inclusive case, the values are consistent within errors, although the fluctuations across the trigger types are large.

8.6 Jet Multiplicity

Figs. 8.20, 8.21, 8.22, and 8.23 show the asymmetries at low and high mass when the sample is partitioned by jet multiplicity. The asymmetry values are summarized in Table 8.4 along with some predictions from MCFM and Madgraph. In the data, at low mass there are no asymmetries, while at high mass the asymmetry is increased by 1σ in the 4jet sample and significantly decreased in the 5jet sample. In Fig. 8.23, the expected PYTHIA asymmetry at high mass in the 5jet sample is-0.110 ± 0.100. The negative asymmetry is due to color flow in the initial state radation, which produces a fifth jet. So while the observed asymmetry in the 5jet sample is lower than the 4jet asymmetry, it is higher than the PYTHIA prediction. The MCFM calculation for NLO QCD effect shows a very large asymmetry in 4-jets at high mass, almost comparable to the data, although we must remember that the parton-level MCFM result would likely be diluted by passage to the lab frame and detector. MCFM predicts the exclusive 4-jet asymmetry to be a factor of 2 larger than the inclusive asymmetry, whereas the ratio in the data is 1.28 ± 0.45. The Madgraph model shows a significant decrease of the small low-mass asymmetry in going from 4-jet to 5-jets, but a large asymmetry almost independent of jet multiplicity at high mass. The comparisons here are hampered by the gaps in the MCFM values, we are working to fill those in.

	N	all $M_{t\bar{t}}$	$M_{t\bar{t}} < 450$ GeV/c^2	$M_{t\bar{t}} \geq 450$ GeV/c^2
incl. data	1260	0.057±0.028	-0.016±0.034	0.21±0.049
4-jet	939	0.065±0.033	-0.023±0.039	0.26±0.057
5-jet	321	0.034±0.056	0.0049±0.07	0.086±0.093
incl. MCFM		0.058 ± 0.087	0.040 ± 0.006	0.088 ± 0.013
4-jet MCFM		0.115 ± 0.017		0.180 ± 0.027
5-jet MCFM				
incl. Madgraph		0.130 ± 0.004	0.060 ± 0.006	0.250 ± 0.008
4-jet Madgraph		0.140 ± 0.005	0.073 ± 0.007	0.270 ± 0.009
5-jet Madgraph		0.084 ± 0.010	0.016 ± 0.012	0.200 ± 0.016

Table 8.4. The asymmetry $A(q\Delta y_{lh})$ in all data, and above and below $M_{t\bar{t}} = 450$ GeV/c^2, for 4jet and 5(or more)jet events.

8.7 B-tagging

We have disucssed the absence of the asymmetry in the inclusive double tagged sample. Figs. 8.24 and 8.25 shows the Δy distributions in events with single and double tags (top and bottom) when the sample is divided into low and high mass (left and right). The asymmetries in each sample are given in the top rows of Table 8.3.

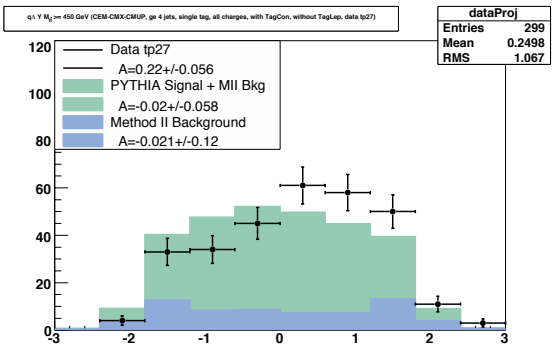

Figure 8.24. The distribution of Δy_{lh} at high mass for single-tagged events.

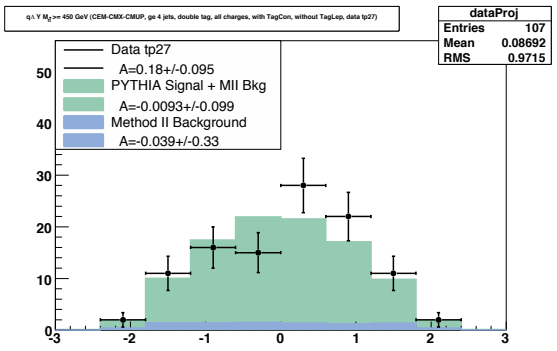

Figure 8.25. The distribution of Δy_{lh} at high mass for double-tagged events.

In the double tags at high mass, the asymmetry is statistically compatible with either the single tags or with zero. The double tagged Δy distribution does show a suggestion of the same asymmetric behavior as in the single tags. It suggests that the double tag problem is because the asymmetry is at high mass, and the number of double tags at high mass is still too small to provide any sensitivity.

It is also interesting that the Pythia prediction for Δy in the high mass double

tags is much narrower than in the single tags. This may be evidence of an acceptance bias related to requirment that both b-tagged jets have $\mid \eta \mid \leq 1.0$.

8.7.1 Anti-Tags

The complement of the single and double tags is the antitag sample. The Δy distribution in the anti-tags at high mass is shown in Figs. 8.26, where our model is seen to be in good agreement with the data. The anti-tags are background dominated, so this comparison checks the mass dependence of the M24U modeling, and, in particular, the background asymmetry modelling. Both antitag samples show slight positive asymmetries. In the high mass case $A^{t\bar{t}} = 0.054 \pm 0.035$ compared to expected background and total model predictions of zero. If we mix backgrounds and $t\bar{t}$ in the expected ratio for anti-tags ratio and assume the $t\bar{t}$ component has an asymmetry of 26.6%, we find a total expected anti-tag of asymmetry $A^{t\bar{t}} = 0.079 \pm 0.034$ in agreement with the data.

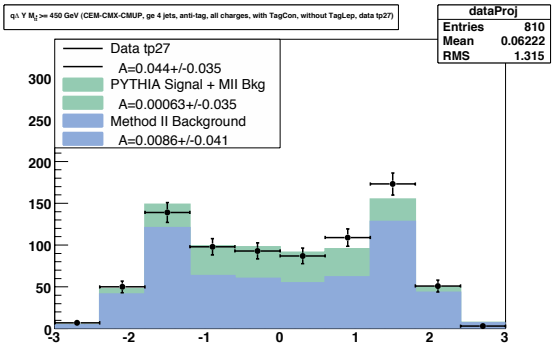

Figure 8.26. The distribution of Δy_{lh} at high mass for anti-tag events.

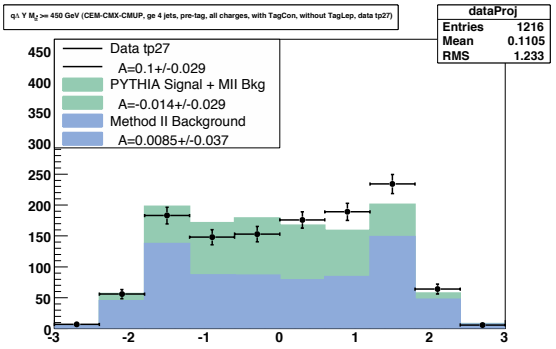

Figure 8.27. The distribution of Δy_{lh} at high mass for pre-tag events.

The good agreement between anti-tag model and data includes a spiky structure in the background prediction in a limited region of rapidity difference: $1 < \Delta y < 2$. The $\Delta y = q\Delta y_{lh}$ distributions at high mass for the nine different components of the background model are shown in Fig. 8.28. The spikes at high Δy are produced by the QCD backgrounds, perhaps an artifact of forcing the QCD events into the $t\bar{t}$ hypothesis. This is unexpected and under study, but the QCD backgrounds are

symmetric (and expected to be), don't contribute to the asymmetry, and do seem to be well modeled in the anti-tags.

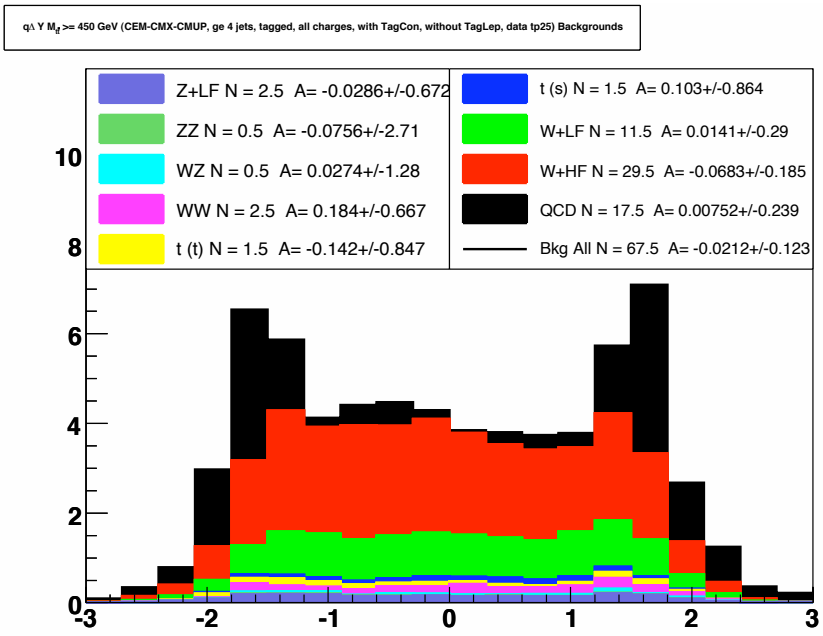

Figure 8.28. The M24U background prediction for Δy at high mass.

8.7.2 Pre-Tags

The remaining b-tag comparison sample is the union of the single tags, double tags, and anti-tags, *a.k.a* the pre-tag sample. Figure 8.27, shows the pre-tag Δy distribution at high mass. At high mass, the predicted asymmetry including the backgrounds at the M24U asymmetry (zero) and $t\bar{t}$ at 26.6% asymmetry, is $A^{t\bar{t}} = 0.111 \pm 0.028$, in agreement with the observed value in the data, $A^{t\bar{t}} = 0.100 \pm 0.029$.

A final b-tagging exercise tests the impact of b-tag information in the event reconstruction. The standard reconstruction requires that b-tagged jets are used as b-partons. Perhaps this constraint combines with an asymmetry in the b-tagging to create an artificial asymmetry in the top direction? To check this we re-run the reconstruction *without* the requirement that b-tags are associated with b-partons. The results for tags and pre-tags, shown at the bottom of Table 8.5 and in Fig. 8.30 are

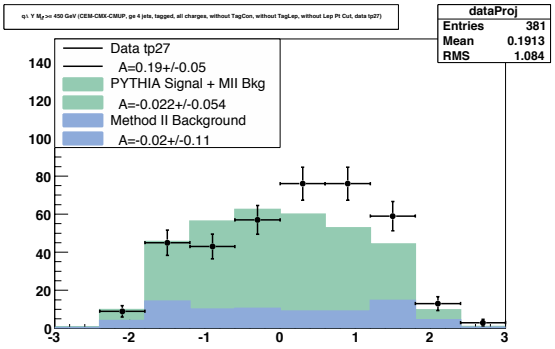

Figure 8.29. The distribution of Δy at high mass for tagged events when the reconstruction is not required to match b-tag jets with b-partons.

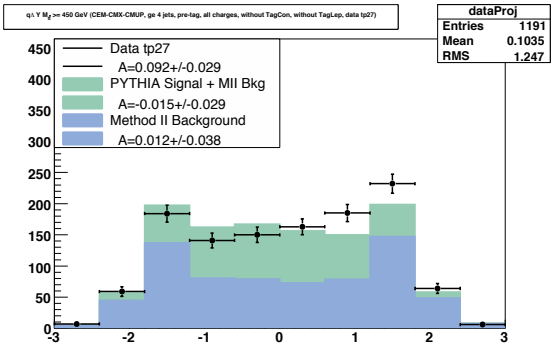

Figure 8.30. The distribution of Δy at high mass for pretag events when the reconstruction is not required to match b-tag jets with b-partons.

very close to asymmetries and distributions found when b-tag consistency is required. These results, particularly for the pretags at high mass, suggest that the asymmetry at high mass does not arise from any kind of bias associated with b-tagging.

		A^{tt}		
	N	Inclusive	$M_{t\bar{t}} < 450$ GeV/c^2	$M_{t\bar{t}} \geq 450$ GeV/c^2
b-tags	1260	0.057±0.028	-0.016±0.034	0.210±0.049
single	979	0.058±0.032	-0.015±0.038	0.220±0.056
double	281	0.053±0.060	-0.023±0.076	0.180±0.095
anti	3019	0.033±0.018	0.029±0.021	0.044±0.035
pretag	4279	0.040±0.015	0.017±0.018	0.100±0.029
notagcon	1260	0.062±0.028	0.006±0.034	0.190±0.050
notagcon, pretag	4279	0.042±0.015	0.023±0.018	0.092±0.029

Table 8.5. The asymmetry $A^{t\bar{t}}$ in all data, and above and below $M_{t\bar{t}} = 450$ GeV/c^2, for different b-tagging selections.

8.8 Summary on A vs. $M_{t\bar{t}}$

The various cross-checks performed to check the source of the observed asymmetry are summarized for $A^{t\bar{t}}$ in Table 8.6 and for $A^{p\bar{p}}$ in Table 8.7. The checks of the independent charge samples, the individual triggers, tighter χ^2 cuts, relaxed b-tag consistency, and pre-tag samples are all consistent with a real effect. The checks of the single/double tags and the different periods are ambiguous regarding the mea-

surement.

		$A^{t\bar{t}}$		
	N	Inclusive	$M_{t\bar{t}} < 450$ GeV/c^2	$M_{t\bar{t}} \geq 450$ GeV/c^2
inclusive tagged	1260	0.057±0.028	-0.016±0.034	0.210±0.049
pos. leptons	613	0.067±0.040	-0.013±0.050	0.210±0.066
neg. leptons	647	-0.048±0.039	0.020±0.047	-0.210±0.071
$\chi^2 \leq 3$	338	0.030±0.054	-0.033±0.065	0.180±0.099
relax b-tag con.	1260	0.062±0.028	0.006±0.034	0.190±0.05
P0-19 (3.4 fb^{-1})	777	0.071±0.036	-0.028±0.043	0.280±0.061
P20-27 (3.1 fb^{-1})	341	0.067±0.054	0.069±0.065	0.064±0.096
CEM	735	0.026±0.037	-0.02±0.045	0.12±0.063
CMUP	332	0.13±0.054	0.047±0.065	0.31±0.095
CMX	172	0.035±0.076	-0.140±0.091	0.430±0.120
pre-tag	4279	0.04±0.015	0.017±0.018	0.1±0.029
pre-tag no tag-con	4279	0.042±0.015	0.023±0.018	0.092±0.029
single tag	979	0.058±0.032	-0.015±0.038	0.220±0.056
double tag	281	0.053±0.060	-0.023±0.076	0.180±0.095
4 jets	939	0.065±0.033	-0.023±0.039	0.260±0.057
5 jets	321	0.034±0.056	0.005±0.070	0.086±0.093

Table 8.6. The asymmetry $A^{t\bar{t}}$ in all data, $M_{t\bar{t}} < 450$ GeV/c^2, and $M_{t\bar{t}} \geq 450$ GeV/$c^2$for various selections.

8.9 Backgrounds as Source of Observed Asymmetry

In Sec. 8.7, the calculation of the expected value of $A^{t\bar{t}}$ relied on the assumption that the background was well-modeled and thus the background asymmetry was accurate. If this assumption is false, it calls into question any conclusions we draw about the asymmetry. To examine how the backgrounds could affect the asymmetry, we will first examine the backgrounds in the data using anti-tags, then we will explore the possible ways the background modeling could alter the observed asymmetry: normalization, fluctuation, and incorrect estimation.

8.10 Cross-Check of Anti-Tags as Background

The anti-tag sample is dominated by background events, so it allows both a check of our background models and an estimate of the asymmetry of the background. As seen

		$A^{p\bar{p}}$		
	N	Inclusive	$M_{t\bar{t}} < 450$ GeV/c^2	$M_{t\bar{t}} \geq 450$ GeV/c^2
inclusive tagged	1260	0.073±0.028	0.059±0.034	0.100±0.049
pos. leptons	613	0.070±0.040	0.028±0.050	0.150±0.067
neg. leptons	647	-0.076±0.039	-0.085±0.047	-0.053±0.072
$\chi^2 \leq 3$	338	0.140±0.054	0.170±0.064	0.061±0.100
relax b-tag con.	1260	0.090±0.028	0.069±0.034	0.140±0.051
P0-19 (3.4 fb^{-1})	777	0.100±0.036	0.081±0.043	0.150±0.063
P20-27 (3.1 fb^{-1})	341	0.009±0.054	0.009±0.066	0.009±0.096
CEM	735	0.053±0.037	0.086±0.045	-0.012±0.064
CMUP	332	0.130±0.054	0.064±0.065	0.290±0.096
CMX	172	0.035±0.076	-0.042±0.092	0.210±0.130
pre-tag	4279	0.011±0.015	-0.009±0.018	0.059±0.029
pre-tag no tag-con	4279	0.016±0.015	-0.005±0.018	0.070±0.029
single tag	979	0.095±0.032	0.079±0.038	0.130±0.057
double tag	281	-0.004±0.060	-0.023±0.076	0.028±0.097
4 jets	939	0.076±0.033	0.039±0.039	0.160±0.058
5 jets	321	0.065±0.056	0.120±0.069	-0.034±0.093

Table 8.7. The asymmetry $A^{p\bar{p}}$ in all data, $M_{t\bar{t}} < 450$ GeV/c^2, and $M_{t\bar{t}} \geq 450$ GeV/$c^2$for various selections.

in Fig. 8.26, the background model is in good agreement with the anti-tag sample. The overall asymmetry observed in the anti-tag sample is a weighted combination of the signal asymmetry and the background asymmetry as expressed in Equation 8.1:

$$A_{\text{measured}} = \alpha_{\text{signal}} A_{\text{signal}} + \alpha_{\text{background}} A_{\text{background}} \tag{8.1}$$

where α_{signal} and $\alpha_{\text{background}}$ represent the relative weights of the signal and background samples as fractions of the whole. Equation 8.1 can be re-arranged to express the background asymmetry in terms of the measured and signal asymmetries along with the respective fractions:

$$A_{\text{background}} = \frac{A_{\text{measured}}}{\alpha_{\text{background}}} - \frac{\alpha_{\text{signal}}}{\alpha_{\text{background}}} A_{\text{signal}} \tag{8.2}$$

The measured asymmetry in the anti-tag sample can be used to estimate an upper bound on the background asymmetry. First we note that the signal asymmetry

is bounded below by the PYTHIA asymmetry, $A_{\text{signal}}^{\text{PYTHIA}} = -0.017$, and above by the parton-level MCFM asymmetry, $A_{\text{signal}}^{\text{MCFM}} = 0.090$. The PYTHIA and MCFM signal values give good estimates for the low and high values of the signal asymmetry, because PYTHIA is a leading-order estimate and MCFM is a next-to-leading-order estimate calculated at the parton-level (roughly a factor of two higher than the detector-level value). As the slope of the signal asymmetry in Equation 8.2 is negative, the lower bound of the signal asymmetry will produce the upper bound on the background asymmetry. To obtain a conservative upper bound, the value of the anti-tag asymmetry is two standard deviations about the measured value of $A_{\text{measured}}^{\text{anti}} = 0.044 \pm 0.035$. Thus, $A_{\text{background}} \leq 0.157$. At the estimated background fraction, $\alpha_{\text{background}} = 0.157$, the upper bound of the background asymmetry is not large enough to account for the measured asymmetry in the tagged sample.

8.11 Background Normalization Errors

If the background normalization is incorrect, then it will change the measured asymmetry by changing the relative weight of the background asymmetry. This can be seen directly in Equation 8.1. Taking advantage of the fact that the relative weights sum to one, Equation 8.1 can be re-arranged to express the background fraction in terms of the asymmetries:

$$\alpha_{\text{background}} = \frac{A_{\text{measured}} - A_{\text{signal}}}{A_{\text{background}} - A_{\text{signal}}} \tag{8.3}$$

Using $A_{\text{measured}} = 0.210 \pm 0.049$ and the signal and background asymmetries from various sources, Equation 8.3 can be used to give the background fractions required for consistency which are summarized in Table 8.8.

To be physical, sample fractions must be between 0 and 1. The background fractions given in Table 8.8 do not meet this condition. It is unlikely that the background normalization alone – while keeping the background asymmetry fixed – is the source

	$A_{\text{background}} = -0.024$		$A_{\text{background}} = 0.157$	
	A_{signal}	$\alpha_{\text{background}}$	A_{signal}	$\alpha_{\text{background}}$
PYTHIA	-0.017	-34.39	-0.017	1.30
MCFM	0.090	-1.06	0.090	1.79

Table 8.8. The required background fractions for each signal source and background asymmetry estimate. The left uses the background asymmetry from the Method II estimates, $A_{\text{background}} = -0.020$, while the right uses the background asymmetry, $A_{\text{background}} = 0.114$, estimated from the anti-tags.

of the observed asymmetry in the tagged sample.

8.12 Background Asymmetry Errors with Variable Normalization

Both fluctuations and errors in the background asymmetry can be considered at the same time, as they result in different asymmetry values from the expected. Again taking advantage of the fact that the relative weights sum to one, Equation 8.1 can be re-arranged to express the background asymmetry in terms of the measured and signal asymmetries along with the background fraction:

$$A_{\text{background}} = \frac{A_{\text{measured}}}{\alpha_{\text{background}}} + \frac{\alpha_{\text{background}} - 1}{\alpha_{\text{background}}} A_{\text{signal}} \tag{8.4}$$

Equation 8.4 is used to plot the required background asymmetry as a function of the required background fraction as shown on the left of Figure 8.31. As expected, the curves for PYTHIA and MCFM both converge when the background fraction goes to unity and the sample is entirely background – thus requiring that the background asymmetry equal the measured asymmetry, $A_{\text{background}} = 0.210$. The vertical black line in Figure 8.31 shows the expected background fraction, $\alpha_{\text{background}} = 0.114$. The intersections of the this line with the two curves show that at this background fraction the background asymmetry is required to be between 80 and 100 percent, which is over 6σ from the expected background asymmetry and over 5σ from the estimated upper bound for the background asymmetry.

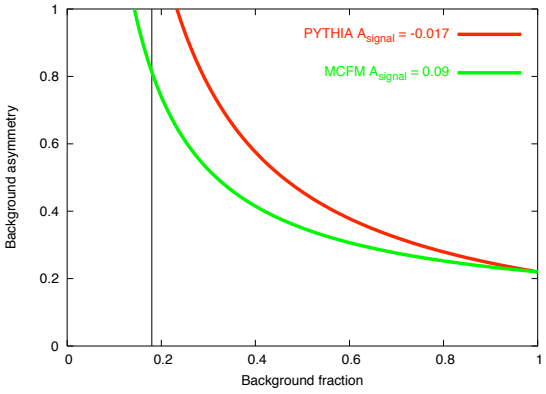

Figure 8.31. The background asymmetry versus background fraction for Δy at high mass. The estimation using the PYTHIA Monte Carlo as the signal asymmetry estimate is in red, and the estimation using the MCFM Monte Carlo is in green. The vertical black line shows the expected background fraction of 0.191.

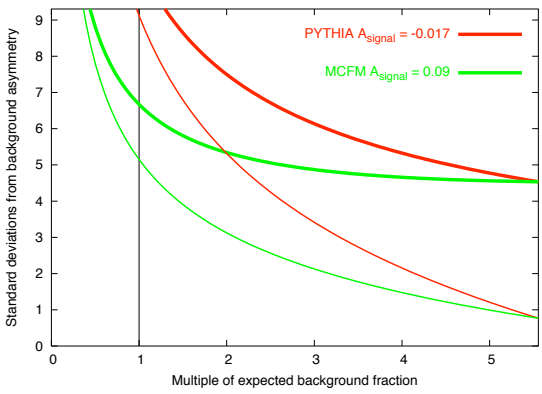

Figure 8.32. The required deviation from the expected background asymmetry versus required background fraction in multiples of the expected background fraction for Δy at high mass. The estimation using the PYTHIA Monte Carlo as the signal asymmetry estimate is in red, and the estimation using the MCFM Monte Carlo is in green. The vertical black line shows the expected background fraction multiple at 1. The thinner lines mark the required curves using the upper bound on the background asymmetry derived from the anti-tags, while the thicker lines mark the required curves using the background asymmetry estimated from Method II.

The number of standard deviations between the required and expected background asymmetries is given by:

$$n_\sigma = \frac{A^{\text{required}}_{\text{background}} - A^{\text{expected}}_{\text{background}}}{\sigma^{\text{expected}}_{\text{background}}} \tag{8.5}$$

where $A^{\text{required}}_{\text{background}}$ is from Equation 8.4. At first glance, it seems that if the required background asymmetry at 80% is over 6σ from the expected value then when the required background asymmetry is reduced by a factor of four to 22% the distance to the expected background asymmetry will drop by a similar factor. But, it is important to note that the denominator in Equation 8.5 is a function of the background fraction, as with a fixed asymmetry the error decreases as the number of events grows larger. To make visual interpretation easier, the curves in the left of Figure 8.31 are re-expressed on the right of the Figure in terms of the number of standard deviations the required background asymmetry is from the expected background asymmetry as a function of multiples of the expected background fraction. The vertical black line at the expected background fraction from the left-hand figure is retained but scaled to unity in the right-hand figure. The thick curves are the distances given the expected background asymmetry, while the thin curves are the distances given the upper bound of the background asymmetry. We see that even in the extreme case of the upper bound on the background asymmetry, the required background asymmetry is still 3σ away when the background fraction is twice its expected value and 2σ away when the background fraction is three times its expected value.

It is unlikely that the background is the source of the asymmetry, even if our estimates for both the normalization and the asymmetry are off. The anti-tag sample confirms that our background is modeled reasonably well.

CHAPTER 9

Validation of the Unfold Procedure

9.1 Prior Validation in CDF9813

A complete study of linearity, bias, and pulls in the unfold was performed in Ref. [28]. Input samples with linear A *vs.* $M_{t\bar{t}}$ behavior in the manner of Fig. 9.1 were created by reweighting Pythia $t\bar{t}$. The distribtution of the top production angle in the $t\bar{t}$ frame was reweighted to add a term of the form $A\cos\theta$, where A depends linearly on $M_{t\bar{t}}$ through two adjustable parameters: $A = \alpha(M_{t\bar{t}}) - 350 + \beta$

By varying slope α and offset β it was possible to create samples over a wide range of A vs. $M_{t\bar{t}}$ functions, and study the performance of the unfold on each. For example to test the output linearity in α, the asymmetry in the two mass bins was used calculate the "reconstructed $A(\alpha)$" which was then compared to the "truth $A(\alpha)$". Fig. 9.1 shows the truth-unfold comparison as a function of α for the case of no constant term ($\beta = 0$). The unfold procedure is extremely linear and the largest bias over the full range of α is $\delta A = 0.028$, much smaller than the statistical uncertainty. The errors returned by the unfold were studied with standard PE techniques, and it was shown that the pulls in the unfold have width 1.0. For further details, see Ref. [28].

9.2 Validation Samples

We are using exactly the same algorithm (in some cases, exactly the same code) as in Ref. [28]. We have rerun our code on the same data samples used there and

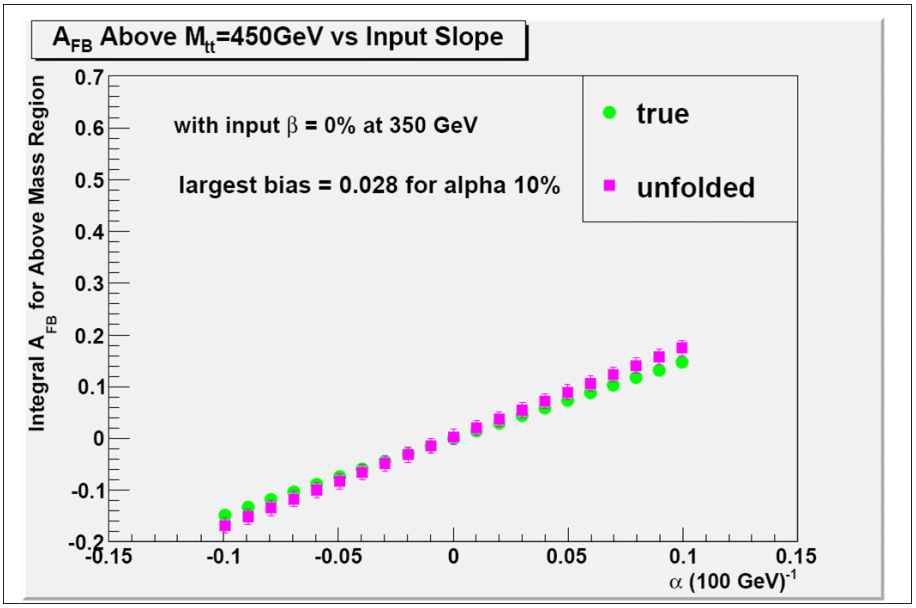

Figure 9.1. The unfold for $A^{t\bar{t}}$ in the axigluon sample using ttop25 at the $M_{t\bar{t}} = 450$ GeV/c^2mass threshold in each of the four bins: low mass forward, low mass backward, high mass forward, high mass backward. True values of the asymmetry are $A_{lh}^{\text{low}} = 0.150$ and $A_{lh}^{\text{high}} = 0.466$.

verified that we exactly reproduce the results there. We do not re-invent any of those performance studies here, but, instead, study two simple samples that reinforce our confidence and allow us to gauge unexpected possible biases in a simple instructive way. Of concern are the creation of asymmetries where there are none (Type 1 errors) and the failure to find asymmetries where they exist (Type II errors). To validate the technique, two samples are needed: one with no asymmetry and one with an asymmetry (preferably a mass-dependent one). For the former, we will use ttop25, which as a leading-order QCD Monte Carlo, has no asymmetry across the whole mass range. For the latter, we will use MADGRAPH with an axigluon model which has a large, mass-dependent asymmetry. As seen in Figs. 9.3 and 9.5, the two samples have similar mass distributions, differing mainly in their rapidity distributions, which allows for better validation of the technique as it compares to the data sample on hand [32].

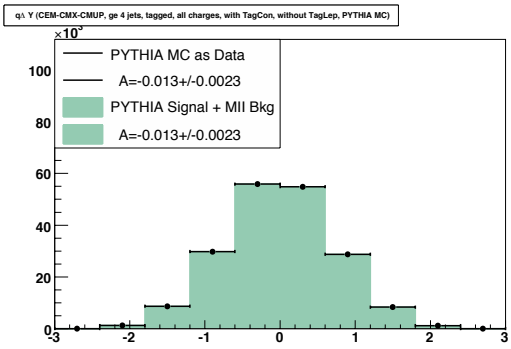

Figure 9.2. The distribution of $q\Delta y_{lh}$ for ttop25.

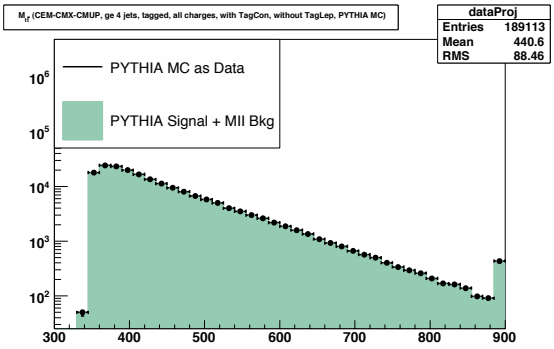

Figure 9.3. The distributions of $M_{t\bar{t}}$ for ttop25.

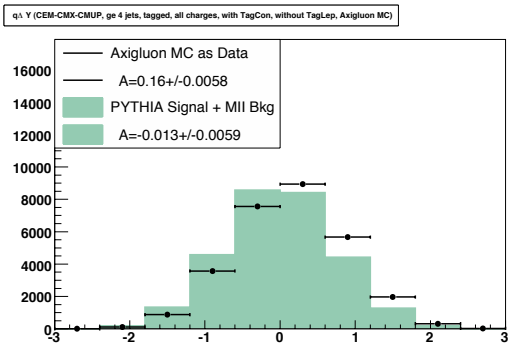

Figure 9.4. The distributions of $q\Delta y_{lh}$ for axigluon.

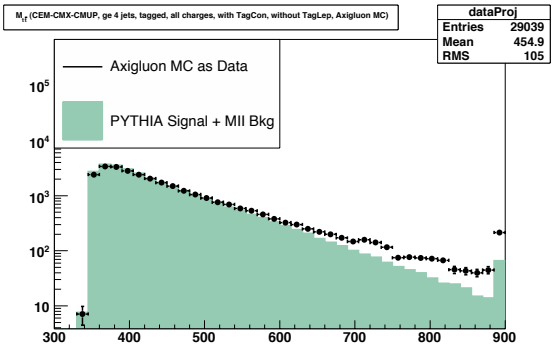

Figure 9.5. The distributions of $M_{t\bar{t}}$ for axigluon.

9.3 Type I Errors

At the leading-order, QCD has no asymmetry at any invariant mass threshold, so ttop25 is a good sample to test if the unfold technique introduces any asymmetries where they don't exist. In Figs. 9.6 and 9.7, the raw values (in black) of the asymmetries show discrepancies from the truth values (in turquoise). In the asymmetries below the mass threshold, the asymmetry is relatively constant of roughly -1% – likely due in part to an acceptance bias in favor of backward events. Above the mass threshold, the raw asymmetry values seem to exhibit a combination of the acceptance biases for backward and high mass events – with roughly constant values of around -1% until around 500 GeV/c^2 when the the asymmetry increases to about 5% at 800 GeV/c^2. After the unfold, however, the corrected asymmetries (red values) are constant at the expected value of zero. Tables 9.1 confirms that the corrected values are consistent with the truth values. This gives us confidence that the unfold does not create an artificial asymmetry – indeed, in this case it removes an asymmetry that was an artifact of the acceptance and smearing.

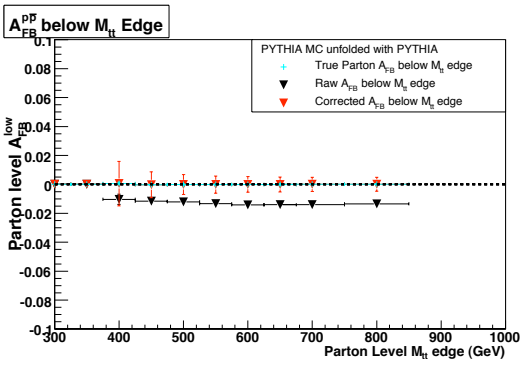

Figure 9.6. Mass-dependence of $A^{t\bar{t}}$ in ttop25 below the mass threshold with values before and after ttop25 unfold.

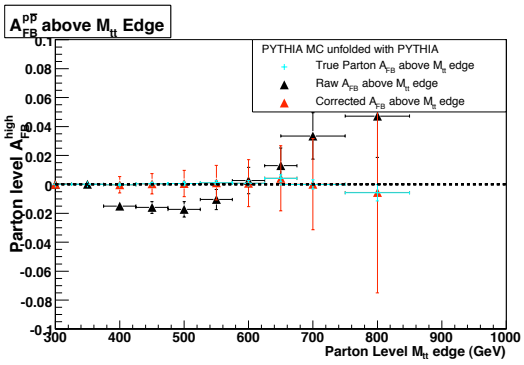

Figure 9.7. Mass-dependence of $A^{t\bar{t}}$ in ttop25 above the mass threshold with values before and after ttop25 unfold.

	low mass		
edge	$A^{p\bar{p}}$	$A^{t\bar{t}}$	Truth $A^{t\bar{t}}$
400	-0.010 ± 0.004	0.001 ± 0.015	-0.002
450	-0.012 ± 0.003	0.000 ± 0.009	0.000
500	-0.012 ± 0.003	-0.001 ± 0.007	0.000
550	-0.013 ± 0.002	-0.001 ± 0.006	0.001
600	-0.014 ± 0.002	0.000 ± 0.005	0.000
650	-0.014 ± 0.002	-0.000 ± 0.005	0.000
700	-0.014 ± 0.002	0.000 ± 0.005	0.000
800	-0.014 ± 0.002	0.000 ± 0.005	0.000
	high mass		
edge	$A^{p\bar{p}}$	$A^{t\bar{t}}$	Truth $A^{t\bar{t}}$
400	-0.015 ± 0.003	0.000 ± 0.006	0.000
450	-0.016 ± 0.004	0.000 ± 0.007	0.000
500	-0.017 ± 0.005	0.001 ± 0.009	0.001
550	-0.010 ± 0.007	0.001 ± 0.012	0.001
600	0.003 ± 0.009	0.001 ± 0.016	0.001
650	0.013 ± 0.012	0.004 ± 0.023	0.004
700	0.034 ± 0.000	0.000 ± 0.032	0.000
800	0.047 ± 0.029	-0.006 ± 0.069	0.000

Table 9.1. The $p\bar{p}$- and $t\bar{t}$-frame asymmetry values of $A^{t\bar{t}}$ in ttop25 compared at low and high $M_{t\bar{t}}$ as the invariant mass threshold is scanned.

9.4 Type II Errors

To create a sample with a large, known asymmetry, we used MADGRAPH with an axigluon model containing a pole at 1.8 TeV. This served as an improvement over past asymmetric models which were either a post-reconstruction ad hoc modification of PYTHIA or a Z' model with a mass spectrum that didn't match the observed $M_{t\bar{t}}$ spectrum. Our axigluon model, while explicitly not a prediction for the data, allows us to use a model that closely matches our invariant mass distribution and can be fully reconstructed from the parton-level giving useful comparisons of the corrected values to truth values. While it can be useful in the abstract to check how the unfold technique functions with matrix entries derived from axigluon truth values, there is more utility in using ttop25 truth values in the matrices since PYTHIA is expected to be a first-order model of the data while there is no such expectation

for an arbitrary and unphysically motivated model such as the axigluon model in MADGRAPH. In Figs. 9.8 and 9.9, the raw values (in black) of the asymmetries show discrepancies from the truth values (in turquoise). Below the mass threshold, the corrected asymmetry values are consistently higher than the truth values by about 25% of the truth asymmetries. Above the mass threshold, the corrected values are much closer to the truth asymmetries (usually differing by 2-6%). In both above and below cases, the corrections are an improvement over the uncorrected values. Table 9.2 confirms that the corrected values are consistent with the truth values. This gives us confidence that the unfold correctly recovers an asymmetry that is dampened by detector-level effects.

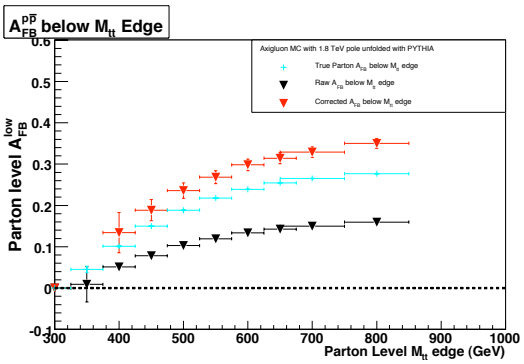

Figure 9.8. Mass-dependence of $A^{t\bar{t}}$ in the axigluon sample below the mass threshold with values before and after ttop25 unfold.

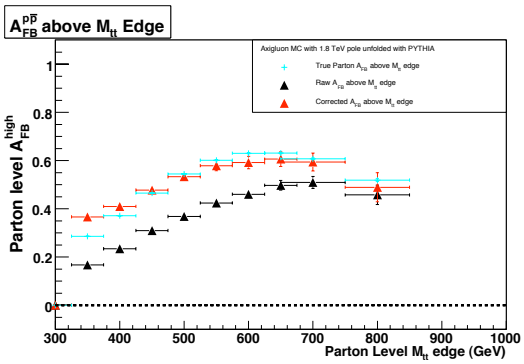

Figure 9.9. Mass-dependence of $A^{t\bar{t}}$ in the axigluon sample above the mass threshold with values before and after ttop25 unfold.

9.5 Validation Summary

In both the axigluon and ttop25 samples, the unfold technique provided corrected values that were an improvement over the raw asymmetries. The technique also showed robustness in the face of the creation of both Type I and Type II errors. The comparison of the corrected values to the truth values will also aid in estimating systematic errors.

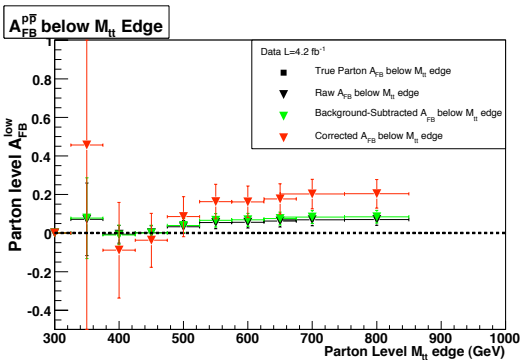

Figure 9.10. Mass-dependence of $A^{t\bar{t}}$ in $t\bar{t}$ events in $\mathrm{L} = 5.3\ \mathrm{fb}^{-1}$ below the mass threshold with values before and after ttop25 unfold.

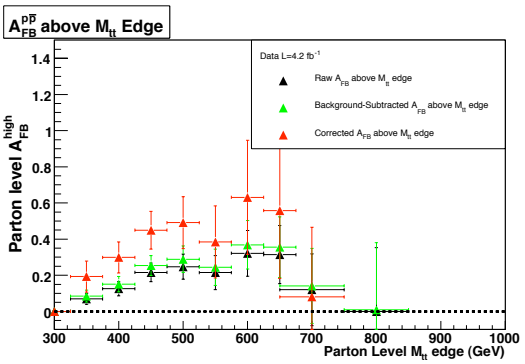

Figure 9.11. Mass-dependence of $A^{t\bar{t}}$ in $t\bar{t}$ events above the mass threshold with values before and after ttop25 unfold.

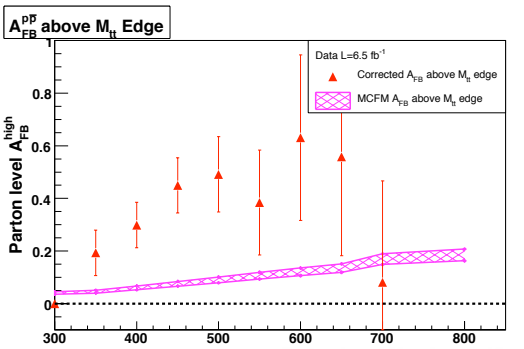

Figure 9.12. The corrected parton-level value of $A^{t\bar{t}}$ in the high mass sample, as a function of the high mass $M_{t\bar{t}}$ threshold, compared to the MCMF prediction (12% scale error assumed).

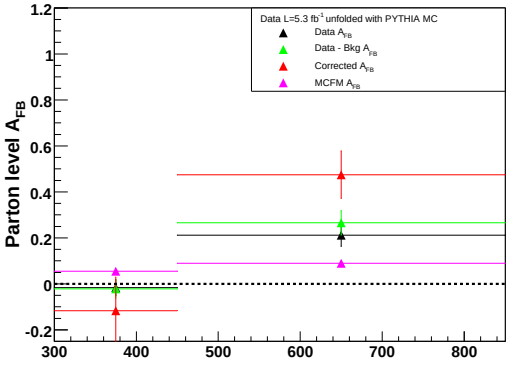

Figure 9.13. Asymmetries below and above $M_{t\bar{t}} = 450\ \mathrm{GeV}/c^2$.

	low mass		
edge	$A^{p\bar{p}}$	$A^{t\bar{t}}$	Truth $A^{t\bar{t}}$
400	0.052 ± 0.010	0.134 ± 0.049	0.101
450	0.078 ± 0.007	0.189 ± 0.025	0.150
500	0.103 ± 0.007	0.236 ± 0.019	0.188
550	0.119 ± 0.006	0.269 ± 0.016	0.218
600	0.134 ± 0.006	0.298 ± 0.014	0.239
650	0.143 ± 0.006	0.314 ± 0.013	0.255
700	0.150 ± 0.006	0.329 ± 0.013	0.265
800	0.160 ± 0.006	0.350 ± 0.012	0.277
	high mass		
edge	$A^{p\bar{p}}$	$A^{t\bar{t}}$	Truth $A^{t\bar{t}}$
400	0.235 ± 0.007	0.410 ± 0.013	0.372
450	0.310 ± 0.009	0.478 ± 0.015	0.466
500	0.369 ± 0.011	0.533 ± 0.018	0.545
550	0.425 ± 0.014	0.579 ± 0.021	0.602
600	0.460 ± 0.017	0.592 ± 0.025	0.631
650	0.498 ± 0.020	0.606 ± 0.031	0.631
700	0.510 ± 0.025	0.594 ± 0.037	0.608
800	0.458 ± 0.040	0.490 ± 0.060	0.519

Table 9.2. The $p\bar{p}$- and $t\bar{t}$-frame asymmetry values of $A^{t\bar{t}}$ in ctopo3 compared at low and high $M_{t\bar{t}}$ as the invariant mass threshold is scanned.

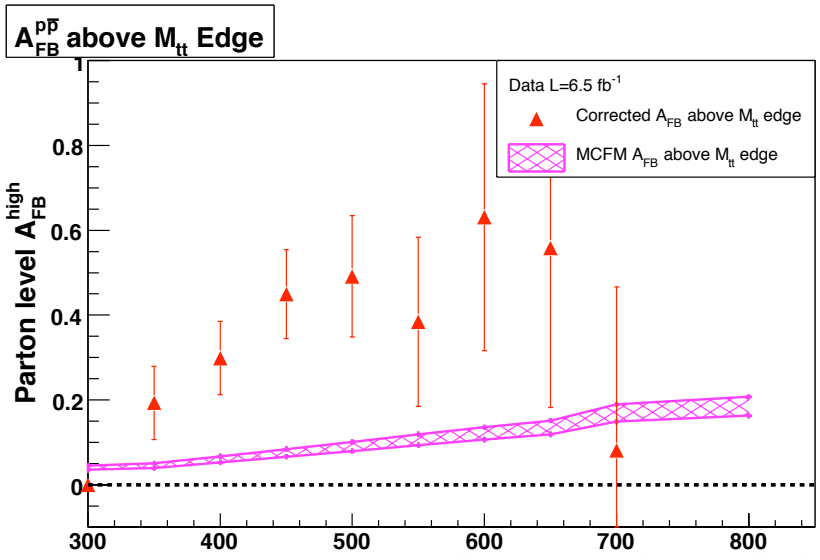

Figure 9.14. The corrected parton-level value of $A^{t\bar{t}}$ in the high mass sample, as a function of the high mass $M_{t\bar{t}}$ threshold, compared to the MCFM prediction (12% scale error assumed).

CHAPTER 10

Systematics

10.1 Overview

All systematic uncertainties represent different uncertainties in our understanding of the models used to correct the reconstructed data. These uncertainties propagate along different paths to our measurements. We consider three different sources of systematic uncertainties for our asymmetry measurements: background, signal, and correction. In all but one case, to compute the systematic uncertainty from the background and signal sources variations are made to the model – which we take to be ttop25 (the leading-order MC sample). The $t\bar{t}$ data sample is then corrected using the model and the variations on it. The differing corrected values are then compared using the standard method of taking the average of the largest pair-wise difference between all the values [33]. The correction systematics are more straightforward: various MC samples are corrected using ttop25 and the resulting values are compared to the known parton-level values.

10.2 Background Systematics

As in Section 8.9, we consider two different background systematics: background normalization and background shape. The former is computed by keeping the overall background shape constant and scaling the number of background events by $\pm\sigma$. The latter is computed keeping the number of background events constant and changing the shape of the background by shifting the background asymmetry by $\pm\sigma$.

The background normalization affects the asymmetry in the final measurement because the background must be subtracted from the reconstructed sample to measure the asymmetry of the $t\bar{t}$ sample. The background asymmetry is expected to be negative, so the $t\bar{t}$ asymmetry must be larger than the asymmetry in the reconstructed data, but the size of the normalization determines the magnitude of the shift. The background normalization is computed from the Method II background tables which estimate the background contribution from nine different sources: QCD, W plus heavy flavor, W plus light flavor, single top (in both s- and t-channels), WW, WZ, ZZ, and Z plus light flavor. QCD is estimated from the data while the other sources are estimated from Monte Carlo. The errors from the estimates are summed in quadrature to give the full estimate of the error in the background normalization. For the $t\bar{t}$ sample used in this analysis, the background normalization is 283.3 ± 93 events. To calculate the systematic error from the background normalization, the background normalization is shifted by $\pm\sigma = \pm 93$ events.

The background shape affects the asymmetry by determining the background asymmetry. The background shape only matters in terms of which events are forward and which events are backward – forward (or backward) events can be shifted around and the overall asymmetry will not change as long as the events remain forward (or backward). So the systematic error on the shape of the background is equal to the systematic error on asymmetry of the background. For a distribution with a given standard deviation, σ, and number of events, n, the error on the standard deviation is given by $\sigma/\sqrt{2n}$. The standard deviation for a distribution is given by Equation 10.1.

$$\sigma = \sqrt{\frac{1 - A^2}{2n}} \tag{10.1}$$

So the error in the standard deviation, σ_σ, is given by Equation 10.2.

$$\sigma_\sigma = \frac{\sqrt{\frac{1-A^2}{n}}}{\sqrt{2n}} = \sqrt{\frac{1-A^2}{2n^2}} = \frac{\sqrt{(1-A^2)/2}}{n} \tag{10.2}$$

So the shifted asymmetries are given by Equation 10.3.

$$A \pm \sigma_\sigma = \frac{n_F - n_B}{n} \pm \frac{\sqrt{(1-A^2)/2}}{n} = \frac{n_F - n_B \pm \sqrt{\frac{1-A^2}{2}}}{n} \tag{10.3}$$

Equation 10.3 can be re-written as Equation 10.4 using $\delta = \sqrt{\frac{1-A^2}{8}}$.

$$A \pm \sigma_\sigma = \frac{(n_F \pm \delta) - (n_B - \pm\delta)}{n} \tag{10.4}$$

For a given background distribution, the number of forward and backward events can be shifted to change the asymmetry of the distribution by σ_σ. The resulting distributions are then subtracted from the reconstructed data and used to compute the systematic uncertainty of the asymmetry with respect to the background shape.

Both of these systematics influence the input to the correction technique, as the correction requires background-subtracted data. Thus these systematics are relevant not only to the corrected measurements but to the background-subtracted measurements. The results for both systematic background contributions are shown in Table 10.1.

10.3 Signal Systematics

We calculate four different sources of the systematics due to the modeling of the $t\bar{t}$ production and decay. These correspond to changes of $\pm\sigma$ in the MC-generated events for the following effects: initial- and final-state radiation (ISR/FSR), jet energy scale (JES), color connection, and parton distribution functions (PDF). The last source is the only one to use a different method to compute the systematic from the method mentioned in Section 10.1; instead, the standard prescription for PDF systematics is used. The results of these systematic checks are shown in Table 10.1.

10.4 Correction Systematics

As in Section 9, we want to evaluate the accuracy of our correction technique in terms of the bias between the truth and unfolded values. To evaluate this, we use three different MC samples: ytop25+ltopo3 which is a leading-order sample generated with PYTHIA with no asymmetry that serves as an alternative to ttop25; ctopo3 which is an axigluon MC sample generated with MADGRAPH with a high, mass-dependent asymmetry; and ctopoa which is identical to ctopo3 in all aspects except the asymmetry which is half that of ctopo3. The first sample gives an intrinsic bias of the technique, as it is a correction of the same type of sample. The last two samples give the bias of the technique when correcting a sample with an asymmetry with a model (ttop25 in this case) with no asymmetry. Of the three samples, ctopoa is the closest in terms of the measured asymmetry to our data sample, though we make no claims about the connection between the data and the model beyond noting that they have similar asymmetries. For each MC sample, the corrected asymmetries are compared with the truth values. At a given invariant mass threshold, the largest discrepancy between the truth value and the correction value is taken as the systematic. The results of these systematic checks are shown in Table 10.1.

10.5 Summary

Overall, apart from extremes at the edges where there are low statistics, the systematic uncertainties for a given invariant mass edge are less than 8% for asymmetries below above. In general, the largest source of systematic uncertainty comes from the correction bias, which is unsurprising given that the sample used for the correction and the sample being corrected have much more potential for variance. After correction bias, the largest source of uncertainty tends to be variation in the jet energy scale. In the central mass region (400-550 GeV/c^2), the systematic uncertainty less than 5% for asymmetries below above.

AFB Systematics Below									
Source	350	400	450	500	550	600	650	700	800
bkg norm	0.067	0.032	0.017	0.002	0.012	0.012	0.013	0.016	0.016
bkg shape	0.245	0.007	0.003	0.002	0.001	0.001	0.001	0.001	0.000
JES	0.218	0.017	0.005	0.003	0.007	0.006	0.007	0.008	0.007
ISR/FSR	0.259	0.012	0.012	0.005	0.001	0.002	0.002	0.003	0.003
color	0.166	0.009	0.004	0.004	0.005	0.004	0.005	0.004	0.004
PDF	0.038	0.018	0.019	0.047	0.005	0.004	0.006	0.006	0.007
Correction	-0.409	0.032	0.037	0.046	0.049	0.057	0.057	0.062	0.071
Total	0.613	0.054	0.047	0.066	0.051	0.059	0.06	0.065	0.073
AFB Systematics Above									
Source	350	400	450	500	550	600	650	700	800
bkg norm	0.014	0.022	0.032	0.034	0.02	0.034	0.019	0.011	0.013
bkg shape	0.004	0.002	0.003	0.006	0.012	0.027	0.041	0.045	0.175
JES	0.003	0.004	0.012	0.021	0.021	0.039	0.035	0.012	0.020
ISR/FSR	0.007	0.007	0.008	0.013	0.017	0.008	0.012	0.058	0.073
color	0.007	0.002	0.004	0.010	0.016	0.021	0.028	0.018	0.038
PDF	0.011	0.003	0.004	0.006	0.012	0.013	0.016	0.167	0.528
Correction	0.079	0.036	0.034	0.012	0.032	0.040	0.053	-0.015	0.022
Total	0.082	0.043	0.049	0.046	0.052	0.075	0.086	0.185	0.563

Table 10.1. Summary of systematic uncertainties for the unfolded asymmetries above and below the invariant mass thresholds.

CHAPTER 11

Conclusions

We have studied the forward-backward asymmetry of top quark pairs produced in 1.96 TeV $p\bar{p}$ collisions at the Fermilab Tevatron. In a data sample with $L = 5.3$ fb^{-1} and 1260 events in the lepton+jet decay topology, we measure both the inclusive asymmetry and the $M_{t\bar{t}}$-dependent asymmetry in the $p\bar{p}$ and $t\bar{t}$ rest frames. We compare to NLO predictions for the charge asymmetry in QCD assuming CP conservation.

	below threshold		above threshold	
threshold	$A^{p\bar{p}}$	$A^{t\bar{t}}$	$A^{p\bar{p}}$	$A^{t\bar{t}}$
400	-0.006 ± 0.046	-0.171 ± 0.271	0.126 ± 0.039	0.293 ± 0.096
450	0.001 ± 0.036	-0.116 ± 0.153	0.216 ± 0.052	0.475 ± 0.114
500	0.053 ± 0.033	0.032 ± 0.165	0.247 ± 0.070	0.562 ± 0.152
550	0.054 ± 0.031	0.130 ± 0.105	0.215 ± 0.094	0.433 ± 0.201
600	0.057 ± 0.031	0.141 ± 0.102	0.321 ± 0.127	0.633 ± 0.323
650	0.062 ± 0.030	0.159 ± 0.099	0.314 ± 0.160	0.527 ± 0.384
700	0.069 ± 0.030	0.184 ± 0.101	0.120 ± 0.199	0.072 ± 0.401
800	0.070 ± 0.030	0.181 ± 0.105	0.000 ± 0.354	0.038 ± 0.946

Table 11.1. The lab and rest frame asymmetries in $t\bar{t}$ events in $L = 5.3$ fb^{-1} below and above $M_{t\bar{t}}$ as the invariant mass threshold is scanned. Errors in corrected asymmetries reflect both statistical and systematic uncertainties.

The $p\bar{p}$ frame measurement uses the rapidity of the hadronically decaying top system. This distribution shows a parton-level forward-backward asymmetry in the $p\bar{p}$ frame of $A^{p\bar{p}} = 0.150 \pm 0.055$ (stat+sys). This has less than 1% probability of representing a fluctuation from zero and is two standard deviations above the predicted asymmetry from NLO QCD. We also study the frame-invariant difference of the rapidities, $\Delta y = y_t - y_{\bar{t}}$; asymmetries in Δy are identical to those in the

top production angle in the $t\bar{t}$ rest frame. We find a parton-level asymmetry of $A^{t\bar{t}} = 0.158 \pm 0.075$ (stat+sys), which is somewhat higher than, but not inconsistent with, the NLO QCD expectation of 0.058 ± 0.009. The asymmetry is a roughly monotonic function of the $t\bar{t}$ invariant mass, $M_{t\bar{t}}$, with $p\bar{p}$ and $t\bar{t}$ asymmetries as shown in Table 11.1.

At the optimal sensitivity threshold of $M_{t\bar{t}} = 450$ GeV/c^2, the asymmetries in the $t\bar{t}$ rest-frame are seen in Table 11.2. The asymmetry at high mass is 3.4 standard deviations above the current NLO prediction for the charge asymmetry of QCD.

	A^{tt}	
	$M_{t\bar{t}} < 450$ GeV/c^2	$M_{t\bar{t}} \geq 450$ GeV/c^2
$L = 5.3$ fb^{-1} events	-0.116 ± 0.153	0.475 ± 0.114
MCFM	0.040 ± 0.006	0.088 ± 0.013

Table 11.2. The rest frame asymmetries in $t\bar{t}$ events in $L = 5.3$fb^{-1} compared to predicted asymmetries from MCFM. Errors in measured asymmetries reflect both statistical and systematic uncertainties.

The asymmetries reverse sign under interchange of lepton charge. The $t\bar{t}$ frame asymmetry for $M_{t\bar{t}} \geq 450$ GeV/c^2 is found to be robust against variations in $t\bar{t}$ reconstruction quality and secondary vertex b-tagging, as well as background normalization and asymmetry strength. When the high-mass data is divided by the lepton avor, the asymmetries are larger in muonic events, but statistically compatible across species. Simple studies of the jet multiplicity and frame dependence of the asymmetry at high mass may offer the possibility of discriminating between the NLO QCD effect and other models for the asymmetry, but the statistical power of these comparisons is currently insufficient for any conclusion.

CDF is predicted to have L 10 fb^{-1} of data recorded by the end of 2011, almost doubling the sample used in this analysis. Repeating this analysis with a larger sample would reduce the statistical uncertainty, likely improving the the discriminatory power of the measurement. Additionally, this analysis focused on the lepton+jets channel of $t\bar{t}$ production. Further analysis in other channels, like the dilepton channel, would add

clarification to this measurement. Collaboration with DØ would also aid in probing the results of this measurement. While it is possible to measure effects related to this analysis at the LHC, it is not possible to make a direct measurement of the same type at the LHC. The LHC is a pp collider, opposed to a $p\bar{p}$ collider like the Tevatron, which means that the direction of the top quark cannot be measured in relation to the proton direction. Without a defined direction for the proton, the forward-backward asymmetry is undefined, so it cannot be measured.

The measurements presented here suggest that the modest inclusive $t\bar{t}$ production asymmetry originates from a signicant effect at large total invariant mass $M_{t\bar{t}}$.

BIBLIOGRAPHY

[1] F. Abe *et al.* "Observation of Top Quark Production in $p\bar{p}$ Collisions with the Collider Detector at Fermilab", Phys. Rev. Lett. **74**, 14 (1995).

[2] S. Abachi *et al.* "Search for High Mass Top Quark Production in $p\bar{p}$ Collisions at $\sqrt{s} = 1.8TeV$", Phys. Rev. Lett. **74**, 13 (1995).

[3] The Tevatron Electroweak Working Group for the CDF and D0 Collaborations, "Combination of CDF and DØ results on the mass of the top quark using up to 5.6fb^{-1}of data", arXiv:hep-ex/1007.3178v1 (2010).

[4] J.H. Kuhn and G. Rodrigo, Phys. Rev. D **59**, 054017 (1999).

[5] S. Frixione and B.R. Webber, JHEP **0206**, 029 (2002), hep-ph/0305252. https://www.hep.phy.cam.ac.uk/theory/webber/MCatNLO/

[6] J. M. Campbell, R. K. Ellis, Phys. Rev. D **62**, 114012 (2000), hep-ph/000304. http://mcfm.fnal.gov/

[7] T. Aaltonen *et al.* (CDF Collaboration), "Measurement of the Forward-Backward Asymmetry in $t\bar{t}$ Production in 3.2fb^{-1} of Tevatron Data", CDF 9724, Mar. 2009. http://www- cdf.fnal.gov/physics/new/top/2009/tprop/Afb/

[8] D. Hirschbuehl *et al.*, "Measurement of the Charge Asymmetry in Top Pair Production Using 1.9 fb^{-1}", CDF9122, Dec. 2008.

[9] T. Schwarz *et al.*, "Measurement of the Front-Back Asymmetry in Top-Antitop Quark Pairs in 1.9 fb^{-1} of Tevatron Data", CDF9169, Jan. 2008.

[10] G. Strycker *et al.*, "Measurement of the Forward-Backward Asymmetry in $t\bar{t}$ Production in 3.2 fb^{-1} of Tevatron Data", CDF9705, March 2009.

[11] G. Strycker *et al.*, "Measurement of the Inclusive Forward-Backward Asymmetry and its Rapidity Dependence in $t\bar{t}$ Production in 5.3 fb^{-1} of Tevatron Data", CDF10185, June 2010.

[12] V. M. Abazov *et al.*, DØ Collaborations, "Measurement of the forward-backward production asymmetry of t and $\bar{t}$ quarks in $p\bar{p} \rightarrow t\bar{t}$ events", DØ Note 6062 CONF, July 2010.

[13] D.W. Jung, P. Ko, J.S. Lee, and S. H. Nam, Phys. Lett. B **691**, 238 (2010); E. Alvarez, L. DaRold, and A. Szynknam, arXiv:1011.6557; D.W. Jung, P. Ko, and J.S. Lee, arXiv:1011.5976; C.H. Chen, G. Cvetic, and C.S. Kim, arXiv:1009.5976; Y.K. Wong, B. Xiao, and S.H. Zhu, arXiv:1008.2685; M. Bauer, F. Goertz, U. Haisch, T. Pfoh, and S. Westhoff, J. High Energy Phys. **11** 039 (2010); R.S. Chivukula, E.H. Simmons, and C.P. Yuan, Phys. Rev. D **82**, 094009 (2010); B. Xiao, Y.K. Wang, and S. H. Zhu, Phys. Rev. D **82**, 034026 (2010); Q.-H. Cao, D. McKreen, J. Rosner, G. Shaughnessy, and C. Wagner, Phys. Rev. D **81**, 114004 (2010); I. Dorsner, S. Fajfer, J.F. Kamenik, and N. Kosnik, Phys. Rev. D **81**, 055009 (2010); S.H. Jung, H. Muryama, A. Pierce, and J.D. Wells, Phys. Rev. D **81**, 015004 (2010); K. Cheung, W.-Y. Keung, and T.-C. Yuan, Phys. Lett. B **682**, 287 (2009); P.H. Frampton, J. Shu, and K. Wang, Phys. Lett. B **683**, 294 (2010); A. Arhrib, R. Benbrik, and C.-H. Chen, Phys. Rev. D **82**, 034034 (2010); D.-W. Jung, P. Ko, J.S. Lee, and S.-H. Nam, arXiv:0912.1105; J. Cao, Z. Heng, L. Wu, and J.M. Yang, Phys. Rev. D **81**, 014016 (2010); V. Barger, W.-Y. Keung, and C.-T. Yu, Phys. Rev. D **81**, 113009 (2010); P. Ferrario, and G. Rodrigo, Phys. Rev. D **78**, 094018 (2008); .

[14] D. McGinnis *et al.*, "The Run II Handbook", Fermilab National Accelerator Laboratory (2000). http://www-ad.fnal.gov/runII

[15] D. Amidei *et al.*, "The CDF II Detector Technical Design Report", FERMILAB-PUB-96-390-E, Fermilab National Accelerator Laboratory (1996).

[16] The CDF Collaboration, CDF Detector Pictures (2005). http://www-cdf.fnal.gov/events/detector_pictures.html

[17] T. Schwarz, "Measurement of the Front Back Asymmetry in Top-Antitop Quark Pairs Produced in $p\bar{p}$ Collisions at $\sqrt{s} = 1.96\ TeV$", Doctoral Dissertation, 2006.

[18] T. Sjostrand, L. Lonnblad, and S. Mrenna, "PYTHIA 6.2 Physics and Manual", Comput. Phys. Commun. **101**, 232 (1997).

[19] G. Corcella *et al.*, "HERWIG 6: An Event Generator for Hadron Emission Reactions with Interfering Gluons", J. High Energy Phys. **01**, 010 (2001).

[20] M. Mangano *et al.*, "ALPGEN, A Generator for Hard Multi-parton Processes in Hadronic Collisions", J. High Energy Phys. **07**, 001 (2003).

[21] F. Maltoni and T. Stelzer, "MadEvent: Automatic Event Generation with MadGraph", J. High Energy Phys. **02**, 027 (2003).

[22] T.Aaltonen *et al.* (CDF Collaboration), CDF Conference Note 9913 (2009).

[23] T. Aaltonen *et al.* (CDF Collaboration), "Observation of Single Top Quark Production and Measurement of $|V_{tb}|$ with CDF", arXiv:hep-ex/1004.1181 (2010).

[24] S. Edielman *et al.* "Review of Particle Physics", Phys. Lett. B **592**, 1 (2004).

[25] A. Abulencia *et al.* (CDF Collaboration), Phys. Rev. D **73**, 032003 (2006).

[26] F. James, "MINUIT: Function Minimization and Error Analysis Reference Manual", Computing and Networks Division, CERN (1998). `http://wwwasdoc.web.cern.ch/wwwasdoc/minuit/minmain.html`

[27] L. Demortier, "Assessing the significance of a deviation in the tail of a distribution", CDF3419, Nov. 1995.

[28] M. Tecchio, T. Schwarz *et al.*, "Dependence of the Forward-Backward Asymmetry in $t\bar{t}$ Production on the $M_{t\bar{t}}$ Invariant Mass", CDF9813, June 2009.

[29] J. Naganoma, K. Kondo, T. Kubo, "Update of Massive Gluon Search USing DLM to 1.9 fb^{-1} $t\bar{t}$, CDF9126, Dec. 2007.

[30] A. Bridgeman, T. Liss "Measurement of the $t\bar{t}$ Differential Cross Section, $d\sigma/dM_{t\bar{t}}$, CDF9157, Jan. 2008.

[31] D0 Collaboration, "Search for $t\bar{t}$ Resonances in the Lepton plus Jets Final State in $p\bar{p}$ Collisions at $\sqrt{s} = 1.96$ TeV, arXiv:0804.3364 (hep-ex), Phys.Lett. B668:98-104, 2008.

[32] We are indebted to T. Tait for the MADGRAPH implementation of the color-octet models.

[33] Top Group Systematic Uncertainties web page,
`http://www-cdf.fnal.gov/internal/physics/top/run2mass/systematics_links.html`,
`http://www-cdf.fnal.gov/internal/physics/top/run2mass/systematics_08_add.html`